KERNFORSCHUNGSZENTRUM

KARLSRUHE

August 1971

KFK 1465

Institut für Neutronenphysik und Reaktortechnik
Projekt Schneller Brüter

Investigation of Integral Parameters of the Fast-Thermal Reactor STARK, Assembly 5

compiled by
G. Kussmaul and H. Meister

GESELLSCHAFT FÜR KERNFORSCHUNG M. B. H.
KARLSRUHE

GESELLSCHAFT FÜR KERNFORSCHUNG M. B. H.
KARLSRUHE

KERNFORSCHUNGSZENTRUM KARLSRUHE

August 1971 KFK 1465

Institut für Neutronenphysik und Reaktortechnik
Projekt Schneller Brüter

Investigation of Integral Parameters of the Fast-Thermal Reactor STARK, Assembly 5

by

Chr. Brückner, K. Burkart, D. Kuhn, G. Kussmaul
H. Meister, and H. Werle

compiled by

G. Kussmaul and H. Meister

Gesellschaft für Kernforschung mbH., Karlsruhe

Abstract

This report gives a compilation of zero-power integral experiments carried out in the fast-thermal reactor STARK, assembly 5. In these experiments the neutron spectrum, reaction rates and material worths in the center of the fast zone as well as physics properties of the entire system were studied. Special emphasis was laid on the further development of the square-wave pile oscillator method to measure reactivity worths of samples.

The experimental results are discussed on the basis of standard multigroup calculations, and some conclusions are drawn as to the suitability of different 26-group cross section sets. With the particular fast core compoisition of this assembly, a central neutron spectrum almost identical with the equilibrium spectrum was obtained, such that reaction rates and the majority of reactivity worth ratios at core center closely represent the values for an all-fast system of the same core composition.

Zusammenfassung

Dieser Bericht gibt eine Zusammenfassung der integralen Nulleistungsexperimente, die in dem schnell-thermischen Reaktor STARK, Anordnung 5, durchgeführt wurden. In diesen Experimenten wurden das Neutronenspektrum, Reaktionsraten und Materialwerte im Zentrum der schnellen Zone sowie die physikalischen Eigenschaften des gesamten Systems untersucht. Besonderer Wert wurde auf die Weiterentwicklung der Pile-Oszillator-Methode gelegt, um Reaktivitätswerte von Materialproben zu messen.

Die experimentellen Ergebnisse werden an Hand von Standard-Multigruppenrechnungen diskutiert und einige Folgerungen bezüglich der Eignung von verschiedenen 26-Gruppen Querschnittssätzen gezogen. Mit der speziellen Zusammensetzung des schnellen Cores dieser Anordnung erhielt man ein zentrales Neutronenspektrum, welches nahezu dem Gleichgewichtsspektrum entspricht, so daß Reaktionsraten und die Mehrzahl der Reaktivitätswerte im Corezentrum nahe bei den Werten liegen, die für ein schnelles Einzonensystem der gleichen Corezusammensetzung gelten.

Introduction

In the coupled fast-thermal assembly STARK 5 a fast core composition was chosen that leads to a relatively soft neutron spectrum. The central zone of STARK 5 contained uranium metal, 12.35 percent enriched, with Al_2O_3, aluminum and 2.1 volume percent polypropylene as additional moderating materials. Compared to the earlier assembly STARK 2, a higher fuel concentration (1.25 kg U^{235} per liter) was adopted such that the spectrum at core center closely represents the equilibrium spectrum in the entire energy range down to 10 eV.

The zero-power experiments carried out in this assembly had three major objectives:

1. - Measurement of the differential neutron spectrum, reaction rate ratios and material worth ratios at core center for a comparison with multigroup calculations. Due to the good spectrum match, most of these quantities are identical with the values that would be found in the center of a large all-fast system of the same core composition.

2. - Investigation of the reactor physics properties of the entire system. In particular, the question of the space dependence of the spectrum was to be studied by measuring the radial variation of reaction rates.

3. - Further development of kinetic methods to measure reactivity changes, especially the improvement of the square-wave pile oscillator technique.

This report gives a general description of the experimental methods and a compilation of the data obtained. In a final section the experimental results are discussed and compared with various multigroup calculations obtained with different cross section sets.

1. Description of the Reactor

The general design of STARK is shown in Fig. 1. Essentially, the reactor consists of 5 distinct zones: the fast zone, a natural uranium buffer zone, a graphite zone, the thermal Argonaut core and an outer graphite reflector.

The central fast core is formed by an array of 37 vertical stainless steel tubes which are fixed by a bottom grid plate. The tubes are filled with platelets (5.07 x 5.07 cm^2) of 19.86 percent enriched uranium metal (a), natural uranium metal (b), Al_2O_3, aluminum (d) with a polypropylene disk (3 cm diameter, 0.1 cm thick) and 25.4 cm thick natural uranium blocks (B) arranged in the following pattern:

Upper reflector (8.25 cm)	Core region (60.6 cm)	Lower reflector (8.25 cm)
B B B b b b	b; 24 x(adbacdab)	b b B B B

A fundamental cell (Fig. 2) consists of 8 platelets (adbacdab) with a mean enrichment of 12.35 percent U^{235}. The total fuel mass in the fast core is 80.658 kg U^{235}.

The fast core is enclosed in a natural uranium metal zone (5.6 cm mean thickness) with a step-shaped inner and an octagonal outer boundary. The purpose of this zone is to absorb low energy neutrons so as to prevent a strong peak in the U^{235} fission rate at the boundary of the fast core.

The surrounding graphite region mainly acts as an internal reflector for thermal neutrons.

The thermal core consists of 24 Argonaut-type fuel elements with graphite wedges between them to form an annular arrangement within an annular aluminum tank (60.95 cm inner diameter, 15.27 cm width). Each fuel element is composed of 11 or 12 fuel plates, respectively, arranged in parallel with a spacing of 6.2 mm for the light-water moderator. The volume between the fuel zone and the outer tank wall is completely filled with graphite pieces. Each fuel plate contains 20.83 g U^{235} in form of 20 percent enriched U_3O_8. Normally, the thermal core is operated at a temperature of 80°C in order to achieve a high degree of inherent shutdown capability.

The control and shut-down system consists of 12 cadmium plates evenly distributed around the thermal core and a fuel-poison safety rod (S_4) installed at an eccentric position in the fast core. Three of the cadmium plates (R_1,R_2,R_3) can be used as fine-control units.

A more detailed description of STARK and its safety features has been given in previous papers [1,2].

2. Multigroup Calculations

Standard one-dimensional multigroup calculations have been performed with the Karlsruhe nuclear code system NUSYS. The calculations were made in cylindrical geometry, assuming a system of concentric zones equal in area and material composition to the corresponding actual zones of the reactor. The atom densities and the geometry of the zones are given in Table 1.

A constant axial buckling $B_z^2 = 13.98 \cdot 10^{-4}$ cm^{-2} independent of energy group and zone was assumed. This value corresponds to an effective core height $H_{eff} = 84$ cm, found as a mean value from a number of fission chamber traverse measurements performed in the fast and thermal zones of STARK, assembly 1 to 5 [3-6] .

The following cross section sets were used in these computations:

1. The Russian cross section set of ABAGJAN et al.[7], referred to as ABN set, which is based on a 1/E-weighting spectrum.
2. The KFK-SNEAK set prepared in Karlsruhe [8,9] and referred to as SNEAK set. This set is based on a reevaluation of cross sections for a number of materials weighted with a collision density spectrum typical for a steam-cooled fast reactor. Other materials are taken unchanged from the ABN set.
3. The H2Ø-PBM set [9] which differs from the SNEAK set in two respects: First, U^{238} capture data in the energy region from 10 keV to 800 keV (groups 6-11) have been slightly decreased, according to measurements of PONITZ et al.[10] and, secondly, U^{235} capture and fission data in the region from 21.5 keV to 400 keV (groups 7-10) have been slightly decreased leaving $\alpha = \sigma_c/\sigma_f$ unchanged.
4. The MØXTØT set [11] where the U^{238} capture data of MOXON et al. [12] are used in the energy region from 0.5 keV to 100 keV.

5. The KFKINR set [13], a modified version of the MØXTØT set in which, besides other changes, the inelastic scattering cross section of U^{238} has been reduced.

The energy group structure of all sets is identical and is given in [7] and shown, for example, in Fig. 3 and 4. For the thermal core and the reflector always the ABN cross sections were used in the 26th group.

The reactor was made critical by increasing the number of fuel plates in the thermal zone (cf.Sec.3.1). In a similar way, the computation procedes by varying the outer radius of the thermal driver (zone 4) until $k_{eff} = 1.00000 \pm 1.0 \cdot 10^{-5}$ is reached. Because the fuel concentration of the thermal zone depends on its thickness, due to the geometry of the graphite wedges, the estimated radius, from which the iteration starts, should not be too far from the final value.

In a succeding perturbation calculation the power contribution γ_m and the relative importance α_m of zone m has been evaluated, using the equation

$$\alpha_m = F_m/F \qquad (2.1)$$

where $F_m = \int_{\text{Zone } m} \Sigma_{i,j} \; \phi_i^+ \chi_i \nu \Sigma_{fj} \phi_j \, dV$

and $F = \Sigma_{\text{all zones}} F_m$.

The α_m are identical with the coefficients of reactivity partition in AVERY's theory of coupled reactors [14] and describe the effect on the overall reactivity

$$\Delta\rho = \sum_m \alpha_m \frac{\delta \nu_m}{\nu_m} \qquad (2.2)$$

of a fictious change $\delta \nu_m$ of the number of fission neutrons in zone m. Some results of the calculations (critical mass, reactivity and power contributions in the reactor midplane of each fuel zone) are given in Tab. 2.

Furthermore, the overall neutron generation time

$$\Lambda = \frac{\int \sum_{i=1}^{26} \phi_i^+ \frac{1}{v_i} \phi_i \, dV}{F} \qquad (2.3)$$

and the effective delayed neutron fractions of the fissionable isotopes U^{235} and U^{238}

$$\beta^M_{eff_i} = \beta^M_i \left(\frac{\sum_{k,j=1}^{26} \phi^+_k \chi_{ki} \nu \Sigma^M_{fj} \phi_j \, dV}{F} \right) \tag{2.4}$$

were computed. The symbols used in Eqs.(2.3) and (2.4) have the following meaning

$$F = \left(\sum_{i,j=1} \phi^+_i \chi_i \nu \Sigma_{fj} \phi_j \, dV \right)_{Reactor} \tag{2.5}$$

$\beta^M_{eff_i}$ = effective delayed neutron fraction of material M, delayed neutron group i,

β^M_i = actual delayed neutron fraction of material M, delayed neutron group i, as measured by KEEPIN /15/

Σ^M_{fj} = macroscopic fission cross section of material M, energy group j,

χ_{ki} = energy distribution of delayed neutrons, delayed neutron group i, energy group k, derived from the measured distributions of BATCHELOR and HYDER /16/ and adapted to the group division of the cross sections sets /17/.

All other symbols have the usual meaning of multigroup formalism. The calculated kinetic parameters are given in Tab. 3.

The reactivity worths of small material samples were determined by first-order perturbation theory. A small amount of sample material (10^{19} to 10^{20} atoms /cm^3) was added to the core mixture within the perturbed zone, usually at core center. In this way, the worth of an infinitely small and dilute sample should be obtained and self-shielding effects should be excluded. To account for the finite size of real samples and to calculate the sample size dependence, a special code has been used /18/, which is based on a collision probability formalism. It allows to calculate the reactivity worth of a finite sample in a surrounding homogeneous core considering resonance self-shielding within the sample. In the limit of an infinitely small sample the reactivity worth converges to the value of first-order perturbation theory.

In order to study the influence of heterogeneity on the equilibrium spectrum of the fast zone, additional 26-group calculations were made with the cell code ZERA /19/ which uses the collision probability method to solve the multigroup transport problem for a periodic slab lattice.

For a more detailed comparison with measured differential neutron spectra a zero-dimensional calculation has been made using the Karlsruhe 208-group cross section set /20/. A buckling value $B^2 = 35.0 \cdot 10^{-4}$ cm^{-2} was assumed, which was obtained from a preceding 26-group calculation with the SNEAK set.

3. Experiments

3.1 Approach to Critical

The approach to critical started from a configuration where all fuel elements of the fast core, except the fuel-poison safety rod S_4, were completely loaded with natural uranium. The thermal zone was filled with moderator and 225 fuel plates, which corresponds to about 80 percent of the critical value predicted by multigroup calculations. In this way, the control system was kept fully effective during the following loading process, where the natural uranium elements were successively replaced by fast core elements filled according to Fig.2. Then the number of fuel plates in the thermal zone was increased until criticality was reached.

After each loading step the multiplication was measured with two BF_3-counters on top of the thermal core and a U^{235}-fission chamber located in the natural uranium zone. A Sb-Be neutron source with a strength of about 10^7 n/sec was used as a start-up source in an eccentric position below the thermal driver zone.

Criticality was reached with 270 fuel plates at 80°C which corresponds to a critical mass of the thermal zone $m_{crit} = 5.614 \pm 0.01$ kg U^{235}.

3.2 Flux and Power Distribution

3.2.1 Flux Distribution in the Thermal Zone

The distribution of the thermal and epithermal flux in the thermal zone has been determined by the two-foil method /21/. In this method pairs

of foils of different materials (Cu and Au) are simultaneously irradiated along a traverse; from the saturation activities of the foils, Z_{Cu} and Z_{Au}, the thermal flux ϕ_{th} and the epithermal flux ϕ_{ep} per unit lethargy are evaluated:

$$\phi_{th} = \frac{1}{\alpha_{Au}} \frac{Z_{Cu} - b\, Z_{Au}}{a - b}\,; \qquad \alpha_{Au} = \frac{N_L}{A}\, \sigma_{act}\, g_{act} \tag{3.2.1}$$

$$\phi_{ep} = \frac{1}{\beta_{Au}} \frac{a\, Z_{Au} - Z_{Cu}}{a - b}\,; \qquad \beta_{Au} = \frac{N_L}{A}\, I_{eff} \tag{3.2.2}$$

where N_L = Avogadro's number,
A = atomic weight,
σ_{act} = thermal activation cross section for Au = 98.80 barn,
g_{act} = Westcott factor for Au at 80°C = 1.0086,
I_{eff} = effective resonance activation integral for Au
(= 1002 barn for Au foils of 8 mg/cm^2).

The quantities $a = (Z_{Cu}/Z_{Au})_{th} = 0.042$ and $b = (Z_{Cu}/Z_{Au})_{Cd} = 0.0045$, i.e. the ratios of the saturation activities, were experimentally determined in a pure thermal neutron field inside the thermal column and in the thermal core under Cd-cover, respectively.

The radial distribution of the thermal and epithermal flux in the reactor midplane is shown in Fig. 5. The calculated curves are normalized with a common factor such that the thermal flux agrees with the experimental value at r = 34.8 cm.

To measure the axial distribution of the thermal flux a miniature U^{235}-fission chamber was used to obtain a good spatial resolution; the chamber was inserted between the fuel plates at r = 34.8 cm. An approximate cosine shape was found in the core region (Fig. 6), except for perturbations close to the axial water reflector and a bump 4 cm below the reactor midplane which is caused by an annular water channel in the graphite wedges. By fitting a cosine function to the unperturbed parts of the curve an effective core height H_{eff} = 84.5±2 cm was found.

3.2.2 Fission Rate Distribution in the Fast Zone

The U^{235} and U^{238} fission rates per atom, n_f^{25} and n_f^{28}, were measured in the fast zone using cylindrical fission chambers (cf.Sec.3.3.1) that have been calibrated against parallel plate absolute chambers

(Tab. 5). For axial and radial traverse measurements these chambers were inserted into a channel inside a special fuel element which was placed into the following core positions:

Pos. 19, 26, 31, 32, 36 (cf. Fig. 1).

Measurements were also made in the channel V of the natural uranium zone.

Fig. 7 shows the experimental data compared with fitted cosine distributions from which the following effective core heights have been derived:

U^{235}-traverse: $H_{eff} = 84.5 \pm 2$ cm,
U^{238}-traverse: $H_{eff} = 81 \pm 2$ cm.

This shows that within experimental error the same axial buckling as in the thermal zone is established, such that one-dimensional radial calculations are expected to give an appropriate description of the system.

The radial distribution of U^{235} and U^{238} fission rates in the reactor midplane are shown in Fig. 8. In addition to the fission chamber data, the U^{235} fission rate in the thermal zone has been derived from the thermal and epithermal fluxes, ϕ_{th} and ϕ_{ep}, found by the Au+Cu foil activation:

$$n_f^{25}(r) = \sigma_{th}^{25}\, g^{25}\, \phi_{th} + \sigma_{ep}^{25}\, \phi_{ep} \qquad (3.2.3)$$

where σ_{th}^{25} = thermal fission cross section of U^{235} = 582 barn,
g^{25} = Westcott factor for U^{235} at 80°C = 0.962.

The effective epithermal fission cross section

$$\sigma_{ep}^{25} = \frac{\sum_{i=1}^{26} \phi_i\, \sigma_{fi}^{25}}{\phi_{21}/\Delta u} \qquad (3.2.4)$$

has been evaluated from the calculated 26-group fluxes ϕ_i in the thermal zone ($\phi_{21}/\Delta u$ = flux per unit lethargy at the Au-resonance, E = 4.9 eV).

3.2.3 Power Distribution in the Entire System

To determine the power distribution in the reactor and the contributions of the various reactor zones, the fission rate per unit volume of the homogenized core, $S(r,z)$, has been derived from the measured fission rates per atom, n_f^{25} and n_f^{28}, and the known atom densities N^{25} and N^{28} of Tab. 1:

$$S(r,z) = S^{25}(r,z) + S^{28}(r,z)$$
$$= N^{25}\, n_f^{25}(r,z) + N^{28}\, n_f^{28}(r,z) \qquad (3.2.5)$$

Spatial integration of $S(r,z)$ over the individual reactor zones yields the corresponding power fractions given in Tab. 4. The results show that about 20 percent of the fissions occur in the fast zone. Integration over the whole reactor then leads to a power calibration of the reactor instrumentation.

For a comparison with one-dimensional radial calculations it is appropriate to consider the power distribution in the reactor midplane, $S(r) = S(r,o)$, which is plotted in Fig. 9. Radial integration of this distribution gives the power fractions γ_m^x of isotope x in zone m

$$\gamma_m^x = \frac{\int_{\text{zone m}} S^x(r)\, rdr}{\int_{\text{all zones}} S(r)\, rdr} \qquad (3.2.6)$$

which are also listed in Tab. 4 together with values derived from a one-dimensional diffusion calculation.

Finally, the power densities in the fuel material of zone m

$$s_m = (N_f^{25}\, n_f^{25} + N_f^{28}\, n_f^{28})_{\text{Zone m}} \qquad (3.2.7)$$

are calculated, using the known atom densities N_f^x for the fuel materials. The ratio of the power densities in the fuel of the fast and the thermal zone was found to be

$$s_1/s_4 = 0.33,$$

which is much lower than the maximum permissible value 1.16 for the moderator temperature of 70°C stated in the safety report of STARK [1].

3.3. Neutron Spectrum and Spectral Indices

The neutron spectrum in the fast zone of STARK 5 has been investigated by measuring differential spectra as well as reaction rate ratios as spectral indices.

3.3.1 Fission Rates and Fission Rate Ratios

To study the spatial variation of the neutron spectrum inside the fast zone, fission rates and their ratios have been measured for the isotopes Th^{232}, U^{233}, U^{235}, U^{238}, Np^{237} and Pu^{239}, using cylindrical fission chambers of 6 mm diameter ($2o^{th}$ Century Electronics, FC-4), which were coated with about 500 $\mu g/cm^2$ of fissionable material. These chambers have been calibrated in a thermal neutron field or, for the threshold substances, with 14 MeV neutrons. To allow a comparison with earlier measurements, the same calibration factors are used as for the previous STARK assemblies [4,5], despite of some deviations from the new absolute fission standards (cf.Tab.5).

Four of these chambers were combined to one unit which was fed through a 1.7 cm wide channel spared out in a special fast core element. Axial fission rate traverses have been obtained by moving the chambers with an automatic driving mechanism, radial traverses by changing the position of the special element containing the fission chambers.

Fig. 10 shows the radial dependence of measured fission rates n_f^x (per sec and atom of isotope x) compared with a 26-group diffusion calculation. The calculated curves have been multiplied by a common normalization factor in such a way that agreement is obtained for U^{235} in the center of the fast zone. Axial and radial traverses for U^{235} and U^{238} are also given in Fig. 7 and 8.

From the measured fission rates n_f^x the fission ratios

$$\sigma^x/\sigma^y = n_f^x / n_f^y \qquad (3.3.1)$$

relative to U^{235} and U^{238} have been derived and plotted in Fig. 11 and 12 as a function of the radial position r.

As may be seen from these figures, all fission ratios are constant within experimental error inside the innermost part ($r \lesssim 10$ cm) of the fast zone.

This indicates that an equilibrium spectrum is reached there at least for those energy groups that give measurable contributions to the corresponding reaction rates. The variation in the outer region is due to low energy neutrons entering from the thermal driver. A detailed discussion of these variations is given in Sec.4.2.

Additional absolute fission rate measurements have been made in the central position of the fast core using Kirn-type parallel-plate fission chambers. The chambers (2.5 cm diameter, 4 mm plate distance) had 0.3 mm thick aluminum walls and were operated as flow counters with an argon-methane mixture. The layer of fissionable material, about 200 ug/cm^2, was prepared by electrodeposition [22] on a 0.2 mm thick stainless steel backing foil. The amount of fissionable material was known within $\pm$ 1 to 2 percent from the stock solution and has been checked by low-geometry α-counting and by intercalibration of counters in the thermal column of STARK.

For the fission ratio measurement two parallel-plate chambers containing different isotopes were arranged back-to-back inside a 10 x 5 x 5 cm^3 void volume spared out in the central fuel element. In this way, the sensitive areas of both counters were exposed to the same neutron spectrum which is supposed to be close to the spatially averaged spectrum of the heterogeneous core structure. Results of these measurements are given in Tab. 5 together with calculated values obtained from various 26-group cross section sets (cf.Sec.4.2).

3.3.2 Indium Sandwich Measurements

Indium sandwiches consisting of three foils of the same thickness ($\approx$ 80 mg/cm^2) have been irradiated in the reactor midplane at various radial positions of the fast zone. The objective of these measurements was to get some information on the neutron intensity at the very low energy end of the spectrum, i.e. near the main resonance at 1.46 eV of the $In^{115}(n,\gamma)In^{116m}$-reaction.

The individual foils of the sandwiches were counted in 2π-β-counters and analyzed for the In^{116m}-activity on the basis of the observed decay curves. Due to the strong self-shielding in the foil, the activity difference C_o-C_i (outer minus inner foil) is predominantly caused by neutrons near the main resonance, while C_i corresponds

to (n,γ)-reactions in the entire energy range. Thus, C_o/C_i-1 may be considered as a spectral index proportional to the relative neutron intensity around 1.46 eV.

Tab. 6 shows the measured activity ratios C_o/C_i together with the ratios obtained from homogeneous and heterogeneous 26-group calculations. A discussion of the results is given in Sec.4.2.

3.3.3 Differential Neutron Spectrum Measurements with Spherical Hydrogen Counters.

The differential neutron spectrum in the center of the fast core was measured by the proton recoil technique using hydrogen-filled proportional counters [23]. To cover the energy range from 30 keV to 1 MeV, four spherical counters (3.94 cm diameter) filled with hydrogen and methane, respectively, under different pressures were used. The counters were inserted into an empty channel obtained by removing the central element from the fast zone.

By operating the reactor at low power ($\approx$10 mWatts) the counting rate was kept below 2000 cps such that deadtime losses could easily be corrected for.

From the measured pulse height distribution of recoil protons per unit energy, P(E), the neutron flux per unit lethargy, $\phi(u)$, can be derived using the relationship

$$\phi(u) = - \frac{E^2}{\sigma(E) N T} \frac{dP(E)}{dE} \qquad (3.3.2)$$

where $\sigma(E)$ = (n,p)-scattering cross section of hydrogen,
N = number of hydrogen atoms within the sensitive region of the counter,
T = live counting time.

The evaluation of experimental data was carried out on the basis of Eq.(3.3.2) using a computer code which calculates the average logarithmic derivative of P(E) within a set of energy intervals $\Delta E/E = 0.20$. Furthermore, wall effect corrections were applied, following the procedure of Benjamin [23], by first subtracting from the measured proton recoil distribution, P(E), the contribution of the spectrum above the upper energy limit of the counter and then multiplying the derivative dP/dE with correction factors obtained from a Monte Carlo calculation.

The energy calibration was achieved by irradiating the counters with monoenergetic neutrons from a Van-de-Graaff generator.

The results of the measurement are compared in Fig. 13 with a zero-dimensional calculation using the Karlsruhe 208-group cross section set. A discussion of the results is given in Sec.4.1.

3.4 Reactivity Measurements

The following methods were employed to measure reactivity changes:

1. - Asymptotic period, rod drop (RD) and inverse kinetics (IK) techniques for reactivities $|\rho| \gtrsim 2\ ¢$,
2. - the square-wave pile oscillator method to measure reactivity worths of small material samples ($|\rho| \lesssim 2\ ¢$) in the center of the fast core.

Whereas the asymptotic period method poses no problems, the other methods exhibit some features not commonly met that will be described in the following.

3.4.1 Reactivity Measurements in the Thermal Zone

3.4.1.1 Theoretical Model

In all cases the time behavior of the neutron population, n(t), was observed and subsequently analyzed. The well-known kinetics equations of a point reactor were consistently used as the theoretical model for all methods of reactivity evaluation. These equations write as follows:

$$\frac{dn}{dt} = \frac{\rho(t)-\beta}{\Lambda}\, n(t) + \sum_{i=1}^{N} \lambda_i\, C_i(t) + S(t) \qquad (3.4.1)$$

$$\frac{dC_i}{dt} = \frac{\beta_i}{\Lambda}\, n(t) - \lambda_i\, C_i\,(t) \qquad (i=1, \ldots\ldots N) \qquad (3.4.2)$$

where all symbols have the usual meaning.

Because of the differences in the λ_i-values for U^{235} and U^{238} [15], 12 delayed neutron groups were used (N=12), 6 for each fissionable isotope contained in the fuel. The effective fraction of the i^{th} group of delayed neutrons, $\beta_i = \beta_{eff_i}$, and the generation time Λ of the prompt neutrons were derived from a 26-group perturbation calculation as described in Sec.2.

3.4.1.2 Experimental Setup

The neutrons are detected by He^3-ionization chambers or by a B^{10}-lined compensated ionization chamber located near the thermal core in the outer graphite reflector. The chamber signal is amplified by an electrometer amplifier and then fed to a voltage-to-frequency converter whose output pulses are counted by a 256-channel multiscaler time analyzer. The channel width was normally set to 0.5 sec.

3.4.1.3 The Inverse Kinetics Method (IK)

The Eqs.(3.4.1) and (3.4.2) can be cast into the following integro-differential equation

$$\frac{\rho(t)}{\beta} + \frac{\Lambda S(t)}{\beta n(t)} = 1 + \frac{1}{n(t)} \left[\frac{\Lambda}{\beta} \frac{dn}{dt} - \sum_{i=1}^{N} a_i \, e^{-\lambda_i t} \left(n_o + \lambda_i \int_o^t n(\tau) e^{\lambda_i \tau} \, d\tau \right) \right] \quad (3.4.3)$$

where $a_i = \beta_i/\beta$. In a source-free system ($S(t) \equiv 0$) or at a power level where the source term is negligible, the measured signal $n(t)$ can be converted by means of Eq.(3.4.3) into the reactivity of the system, starting from the stationary and critical value n_o. A FORTRAN program is used to calculate the right-hand side of Eq.(3.4.3).

This method was widely used in our investigations. If a control or safety rod is inserted with constant velocity, the reactivity-vs.-position characteristics can be determined in a single run. The applicability ranges from minute reactivity values (cf.Sec.3.4.2) to large values of some $. Our investigations showed [24] that the IK method is also very useful in the evaluation of rod drop measurements, if a proper detector position is chosen or if a correction procedure is applied [25].

3.4.1.4 The Rod Drop Method (RD)

For a source-free point reactor, the neutron signal after a step change of reactivity ρ applied at $t = 0$ to a stationary and critical system ($n(t) = n_o$ for $t < o$) is given by

$$\frac{n(t)}{n_o} = \sum_{j=o}^{N} A_j \, e^{\omega_j t} \quad (3.4.4)$$

where ω_j are the N+1 real roots of the inhour equation

$$\omega\left(\Lambda + \sum_{i=1}^{N} \frac{\beta_i}{\omega + \lambda_i}\right) - \rho = 0 \qquad (3.4.5)$$

and

$$A_j = \frac{\Lambda + \sum_{i=1}^{N} \frac{\beta_i}{\omega_j + \lambda_i}}{\Lambda + \sum_{i=1}^{N} \frac{\beta_i \lambda_i}{(\omega_j + \lambda_i)^2}} \qquad (j = 0,1,.....N). \qquad (3.4.6)$$

A detailed analysis of the $n(t)/n_o$-curves measured after a drop of control plates showed a strong variation in the amplitude of the prompt jump with detector position, whereas a few seconds after completion of the reactivity change a common space-independent time behavior was observed [24]. To eliminate spatial effects from the experimental data, n(t) was normalized not to the initial value n_o but rather to a value n(T) at a time T after the reactivity step (e.g. T = 10 sec) which is not influenced by higher spatial modes of the prompt neutron distribution. The reactivity values were obtained by comparing the experimental ratios $n(t)/n(T)$ with those calculated by Eq.(3.4.4), $\sum_{j=s}^{N} A_j e^{\omega_j t} / \sum_{j=s}^{N} A_j e^{\omega_j T}$, for a series of reactivity steps. The reactivity values were found to be independent of detector position within $\pm$ 2 percent.

Compared to the space-independent model, the prompt transient is larger for detector positions close to the control plate and smaller for positions far away. On the boundary of both regions, appropriate detector positions exist at an azimuthal angle of $\approx 60^{\circ}$ from the plate, where n(t) was found to agree well with the space-independent model in its entire shape. In these positions control plate characteristics were determined by the IK method and no systematic deviations from the other methods were observed.

The application of the IK method to RD measurements has been investigated in a recent paper [25]. If the disturbing effect is caused mainly by prompt spatial modes a correction procedure is applicable which eliminates the space dependence of the reactivity values.

3.4.1.5 Reactivity Calibration of Control and Safety Plates

The reactivity worths of the control plates R_1, R_2 and R_3, the safety plate S_3[3] and the fuel-poison safety rod S_4 were measured by the RD method (cf.Sec.3.4.1.4). Two series of measurements were made which differ in the critical position of the control units. In the first series the reactor was made critical by control plate R_3 on position 26.6 cm, all other plates and the safety rod S_4 were fully withdrawn. In the second series the reactor was made critical by S_4 on position 39.2 cm and all Cd-plates were fully withdrawn. The results of both series are given in Tab. 7 as obtained with detector 1 and 2 (cf.Fig.1).

The total reactivity caused by simultaneous insertion of all 12 Cd-plates was found to be 4.7 $. This corresponds to a worth per plate of 39.1 ¢, which is 10 percent smaller than the average worth of a single control plate (43.0 ¢) as given in Tab. 7; the difference is explained by the mutual shadowing of the plates.

Fig. 14 shows the reactivity-vs.-position characterictcs of control plate R_2 as measured by continuous insertion (IK method). The resulting integral worths of this plate and others are also given in Tab. 7. As can be seen, they agree satisfactorily with those determined from RD measurements, except for plate R_1 measured by detector 1.

3.4.1.6 Void Coefficient

In order to measure the reactivity effect of voids in the light-water moderator, a flat aluminum tube (cross section 0.4 cm by 1.0 cm, 61 cm length, volume $\Delta V = 24\ cm^3$) was placed between two fuel plates. By means of a pneumatic device the water within the tube was displaced by air and the reactor was run at constant power. By a sudden pressure release the water was allowed to reenter the tube and the neutron time behavior was observed. The resulting reactivity $\Delta\rho$ was determined by the asymptotic period method as an average value over the core height. The void coefficient was found to be negative throughout the thermal core. Fig. 15 shows the radial distribution of the void coefficient $\frac{\Delta\rho}{\Delta V}$ from which the mean value

$$\frac{\Delta\rho}{\Delta V} = -\ 2.07 \cdot 10^{-4}\ \$ / cm^3$$

was derived. Related to the overall moderator volume of 67.7 l the following relative value was found:

$$V \frac{\Delta\rho}{\Delta V} = - 0.140 \text{ \$ / \% void}$$

The error is estimated to be about 10 percent.

3.4.1.7 Temperature Coefficient

The temperature coefficient of the thermal zone has been determined by continuously raising the moderator temperature at a rate of 4°C per hour, starting from 71°C up to 84°C. During the temperature increase the reactor was kept critical by counterbalancing with a control plate that was calibrated in the same experiment by stepwise withdrawal and determination of the asymptotic period.

The result of this measurement is shown in Fig. 16. There is an approximately linear decrease of reactivity with increasing temperature corresponding to a mean slope

$$\frac{\Delta\rho}{\Delta\vartheta} = - 1.8 \text{ ¢ / °C.}$$

In order to determine the reactivity gain caused by a decrease of the moderator temperature from the operating point (80°C) to room temperature the following relation was assumed

$$\rho(\vartheta) = \text{const.} \quad \rho_2(\vartheta) \qquad (3.4.7)$$

where $\rho_2(\vartheta)$ is the temperature dependence of reactivity measured for STARK2 [4] between 86°C and 32°C. The constant in Eq.(3.4.7) was found by a fit to the common region between 71°C and 84°C. Hence, a reactivity gain

$$\Delta\rho \ (80^\circ C \rightarrow 20^\circ C) = + 0.79 \text{ \$}$$

is obtained.

3.4.2 Pile Oscillator Measurements in the Fast Zone

The reactivity worths of a variety of material samples were measured in the center of the fast zone by a square-wave pile oscillator technique.

Material worth measurements in the empty central channel of earlier STARK assemblies showed remarkable differences between experimental and calculated values [4,5], especially for scattering materials like Al and C. These discrepancies were partly attributed to the perturbing effect of the empty channel that leads to an angular dependence of the neutron flux $\phi(\vec{\Omega})$ and the adjoint $\phi^{+}(\vec{\Omega})$ at core center, from which a non-zero transport contribution to the sample worth is expected to arise. A detailed comparison in STARK 4 [5] between data obtained with an empty and a solid oscillator rod confirmed this conjecture. For the STARK 5 measurements it was therefore decided to use an oscillator element filled with the normal core mixture over its entire length.

The oscillation of the fuel-filled rod results in a periodical replacement of one part of the core fuel by another. During the in-core phase of one part a build-up of delayed neutron precursors occurs which then partially decay within the following out-of-core phase. Because of the resulting periodical net loss of precursors, the kinetic behavior of the reactor differs from that of a usual square-wave oscillated system [26] in so far as a delayed neutron transient is superimposed upon the signal caused by the sample motion.

One of the objectives of the pile oscillator experiments in STARK 5 was to study the applicability of a newly developed analytical model to treat the time behavior of such a fuel-oscillated reactor. Further aims were 1.- the comparison of measured reactivity worths with perturbation calculations performed with different cross section sets; 2.- the comparison of experimental sample size effects with calculations based on a collision probability method [18]; 3.- an investigation of the reactivity effect caused by interaction between different sample materials.

3.4.2.1 Kinetic Model of a Reactor with Oscillated Fuel

In this section a short description of the theoretical model is given which serves as a basis for interpretation of the pile oscillator measurements. For further details we refer to [27]. The kinetic equations of a zero-power point reactor, Eqs.(3.4.1) and (3.4.2), are modified to account for the net loss of delayed neutron precursors at each stroke of the pile oscillator:

$$\frac{dn}{dt} = \frac{\rho(t)-\beta}{\Lambda}\, n(t) + \sum_{i=1}^{N} \lambda_i \left(C_i(t) + f'(t)\, C'(t) + f''(t)\, C''(t)\right) \qquad (3.4.8)$$

$$\frac{dC_i}{dt} = (1-\gamma)\,\frac{\beta_i}{\Lambda}\, n(t) - \lambda_i\, C_i(t) \qquad (3.4.9)$$

$$\frac{dC_i'}{dt} = \gamma\,\frac{\beta_i}{\Lambda}\, n(t)\, f'(t) - \lambda_i\, C_i'(t) \qquad (3.4.10)$$

$$\frac{dC_i''}{dt} = \gamma\,\frac{\beta_i}{\Lambda}\, n(t)\, f''(t) - \lambda_i\, C_i''(t) \qquad (3.4.11)$$

$(i = 1,2,\ldots.N)$

The quantities $n(t)$, $\rho(t)$, Λ, β, β_i, λ_i and N have their conventional meaning (cf.Sec.3.4.1.1); $f'(t)$ and $f''(t)$ are discountinuous functions defined by

$$f'(t) = 1 - H(t) + H(t-T) - H(t-2T) + \ldots + H(t-(2m-1)T) - H(t-2mT) + \ldots$$

and

$$f''(t) = 1 - f'(t)$$

where

$$H(t) = \begin{cases} 1 & \text{for } t > 0 \\ 0 & \text{for } t \leq 0 \end{cases}$$

is the Heaviside or unit-step function and T the time between two consecutive strokes (T = half-period).

The modification of the kinetic equations consists of a division of the precursor population into two parts. The first part, $C_i(t)$, comprises the precursor population that remains fixed within the core during the oscillations. The second part, $C_i'(t)$ and $C_i''(t)$, respectively, is periodically removed from the reactor and decays partially outside the core during the corresponding half-period T. The term $(1-\gamma)\,\frac{\beta_i}{\Lambda} n(t)$ in Eq.(3.4.9) takes into account that only the fraction $(1-\gamma)$ of precursors formed within the core will remain there, the term $\gamma\,\frac{\beta_i}{\Lambda} n(t)$ in Eqs.(3.4.10) and (3.4.11), respectively, describes the production rate of precursors periodically removed. γ is assumed to be time-independent and $\gamma \ll 1$.

The external reactivity is assumed to oscillate in a square-wave manner

$$\rho(t) = \rho_M\,(f''(t) - f'(t)) + \rho_C \qquad (3.4.12)$$

where ρ_M is the reactivity amplitude of the sample and ρ_c a compensating reactivity necessary to achieve a steady-state behavior. Substituting $t = 2\nu T + \vartheta$ with $o \leq \vartheta \leq 2T$ ($\nu = 0,1,2,\ldots$) and integrating Eqs.(3.4.8) to (3.4.11) over one full period one finds the steady-state condition

$$\frac{2T}{\Lambda}\,\rho_c = \frac{1}{\Lambda}\int_o^{2T} \rho(\vartheta)\,d\vartheta = \sum_{i=1}^{N}\lambda_i \left(\int_o^{T} C_i'(\vartheta)\,d\vartheta + \int_T^{2T} C_i''(\vartheta)\,d\vartheta\right) \qquad (3.4.13)$$

and by combining Eqs.(3.4.8) to (3.4.11) the integro-differential equation /27/

$$\left[\frac{\rho_M}{\beta} + \gamma \sum_{i=1}^{N} \frac{a_i}{1+e^{-\lambda_i T}}\left(\frac{1-e^{-\lambda_i T}}{\lambda_i T} - e^{-\lambda_i \vartheta}\right)\right] f''(\vartheta)$$

$$+\left[-\frac{\rho_M}{\beta} + \gamma \sum_{i=1}^{N} \frac{a_i}{1+e^{-\lambda_i T}}\left(\frac{1-e^{-\lambda_i T}}{\lambda_i T} - e^{-\lambda_i(\vartheta - T)}\right)\right] f'(\vartheta) \qquad (3.4.14)$$

$$= 1 + \frac{1}{n(t)}\left[\frac{\Lambda}{\beta}\frac{dn}{dt} - \sum_{i=1}^{N} a_i\, e^{-\lambda_i T}\left(n_o + \lambda_i \int_o^{t} n(\tau)\, e^{\lambda_i \tau}\, d\tau\right)\right] \equiv \rho'(t)$$

$$(\vartheta = t - 2\nu T \text{ with } o \leq \vartheta \leq 2T)$$

where $a_i = \beta_i/\beta$ and n_o is an average value of $n(t)$. By comparison of Eq.(3.4.14) with Eq.(3.4.3) underlying the inverse kinetics method, one finds the r.h. side expressions to be identical. The terms of the l.h. side containing the factor γ can be interpreted as a pseudo-reactivity, $\rho_p(\vartheta)/\beta$, for which the following relation must be fulfilled to obtain stationary state solutions:

$$\int_o^{2T} \rho_p(\vartheta)\, d\vartheta = 0\,. \qquad (3.4.15)$$

$\rho_p(\vartheta)/\beta$ is composed of a time-dependent part caused by the removal of delayed neutron precursors, which is periodical with period T, and the time-independent term ρ_c to compensate, on the average, the precursor loss. Because ρ_M/β changes sign every half-period, in contrast to the pseudo-reactivity $\rho_p(\vartheta)/\beta$, we are able to separate these two parts:

$$\rho'(\vartheta)/\beta - \rho'(\vartheta+T)/\beta = 2\,\rho_M/\beta \qquad (3.4.16)$$

$$\rho'(\vartheta)/\beta + \rho'(\vartheta+T)/\beta = 2\gamma \sum_{i=1}^{N} \frac{a_i}{1+e^{-\lambda_i T}}\left(\frac{1-e^{-\lambda_i T}}{i^T} - e^{-\lambda_i \vartheta}\right) \qquad (3.4.17)$$

$$= 2\gamma\, F(a_i, \lambda_i, T, \vartheta)$$

3.4.2.2 Experimental Equipment

Fig. 17 shows schematically a cross section of the reactor with the pile oscillator and the data recording system. The central fuel element of the fast core has been replaced by a stainless steel tube serving as an experimental channel. Another square stainless steel tube filled with 4.66 x 4.66 cm^2 platelets of fast core materials to an overall height of 145 cm represents the oscillator rod. For material worth measurements two aluminum containers, one for sample and the other empty, were embedded into the oscillator element at two positions, each half a stroke width (21.25 cm) from the rod center. The oscillator rod was connected to the piston of a driving mechanism actuated by compressed air. Thus, the sample was oscillated between the center of the core and a position outside the blanket with a transient time of $\approx$ 1.5 sec such that the reactivity approximately changed in a square-wave manner with a period 2T = 64 sec. The reactor was normally run at a power of 10 Watts.

The neutron signal was measured by a B^{10}-ionization chamber located near the thermal core in the graphite reflector. A large part of the chamber current was suppressed while the oscillating part was amplified by an electrometer amplifier and then fed to a voltage-to-frequency converter. The pulse train of the converter was recorded by a 256-channel multiscaler time analyzer. Oscillator and analyzer were synchronized in such a way that groups of two consecutive periods were stored in each analyzer sweep. Normally ten double-periods were sampled to improve the signal/noise ratio. Small reactivity drifts during the measurement were manually compensated by a slowly moving fine-control rod.

3.4.2.3 Processing of Experimental Data

The experimental data were evaluated by a computer code that employs two methods.
The first method made use of the inverse kinetics code (cf.Sec.3.4.1.3) which calculates the r.h. side of Eq.(3.4.14) from the sampled data n(t) to which the constant suppressed signal had to be added. To attain the steady-state reactivity values, Eq.(3.4.14) is applied to data obtained from a periodical continuation of the original two-period train. The resulting reactivity $\rho'(t)/\beta$ then converges against an asymptotic function after 4 to 5 continuations (t = 8 to 10 min.).

In order to extract the material worth ρ_M and the transient part due to delayed neutrons, differences and sums of corresponding values, as described by Eqs.(3.4.16) and (3.4.17), were formed.

As a second evaluation method a Fourier analysis was applied to the experimental data. For a linear system with a square-wave reactivity input the following relation holds

$$\frac{c_k}{i_o} = \begin{cases} \frac{4}{k\pi} \frac{|\rho_M|}{\beta} |W(j\omega_k)| & \text{for } k = 1,3,5,..... \\ 0 & \text{for } k = 2,4,6,..... \end{cases} \qquad (3.4.18)$$

where c_k = Fourier amplitude of the k^{th} harmonic with frequency $\omega_k = k\pi/T$

i_o = mean signal

$$W(j\omega_k) = \left[j\omega_k \frac{\Lambda}{\beta} + \sum_{i=1}^{I} \frac{a_i}{j\omega_k + \lambda_i} \right]^{-1} = \text{calculated zero power reactor transfer function.} \qquad (3.4.19)$$

By shifting the integration interval of length 2T by steps of T/2 through the two-period signal, we obtain integrals which can be combined in such a way that first and second order drift terms are exactly eliminated [27].

The time analyzer data from a typical 20-period pile oscillator measurement with a 20 percent enriched uranium sample ($\approx$ 250 g) are shown in Fig. 18 which also includes the reactivity values $\rho'(t)$ resulting from the inverse kinetics evaluation, Eq.(3.4.14). The figure shows the square wave oscillation caused by the sample motion and the superimposed delayed neutron transients.

A comparison between the inverse kinetics and the Fourier analysis evaluation is made in Tab.8. As can be seen, the drift-corrected value of the fundamental mode agrees within $\pm$0.4% with the values obtained by the inverse kinetics method. Also the values derived from the odd harmonics up to the seventh agree within 1%.The experimental errors are in accordance with the theoretical sensitivity of the pile oscillator measurement, $1.2 \cdot 10^{-7}$ $\Delta k/k$, as calculated from the formula derived by Frisch and Littler [28], and the experimental value obtained from data accumulated without sample oscillation.

If the reactivity values of Fig. 18 are combined according to Eq. (3.4.17), one obtains the transient due to the build-up of delayed neutron precursors within the in-core part of the pile oscillator rod. Fig.19 shows the values $\rho'(t) + \rho'(t+T)$ derived from Fig.18 in comparison with the theoretical function given in Eq.(3.4.17). Except for a transient phase during the first few seconds, a good agreement between experimental and theoretical values is observed. From a fit to the experimental data the parameter $\gamma = 3.75 \cdot 10^{-3}$ was found which turned out to be the same for all measurements in STARK 5.

3.4.2.4 Investigation of Reactivity Worth vs. Sample Size

Reactivity worth measurements at core center have been made for a variety of sample materials given in Tab.9 and 10. Except for Pu and B^{10}, the sampleswere platelets or foils of 4.66 x 4.66 cm^2 outer dimension which were placed vertically inside the sample container as shown in Fig.20. Thus, the samples were exposed to the average neutron spectrum inside the void volume of the container, which is supposed to be close to the spatially averaged cell spectrum, except for the slight inelastic moderation in the surrounding stainless steel walls.

The resulting sample worths per gram are listed in Tab.9 and 10. The data of Pu and B^{10} are corrected for the effect of the aluminum cladding, the U-data for the nickel coating of the platelets or foils.

For a comparison with first-order perturbation calculations it is necessary to correct the experimental data for the effect of finite sample size, i.e. the effects of self-shielding and self-multiplication For the samplesof Tab. 9 and 10 this was done by measuring the reactivity worth per gram as a function of sample thickness and extrapolating to zero as shown in Fig.21 to 24.

The measured sample size dependence is compared with calculated curves obtained by a collision probability code /18/ (cf.Sec.2), into which the sample size enters by the average cord length, 4V/S. For all sample size calculations the H2ØPMB set was used; the influence of the cross section set on the sample size dependence was found to be rather small.

The calculated reactivity worths are based on an adjusted value of the normalization integral F (cf.Sec.2) that yields agreement with experiment for the U(93.14%)-foils. With this normalization, the calculated reactivity worths of the other materials deviate from experiment by about 10 percent, while a still larger deviation is found for the Nb sample.

Despite of the deviations in absolute value, which are partly due to the residual sample worth in the out-position (Sec.3.4.2.7), the shape of most calculated curves is in good agreement with experiment, as may be seen from the theoretical curves fitted to the measured data in Fig.21 to 23. This indicates that the self-shielding effects are correctly predicted by the integral transport code. An important deviation still remains for CH_2 where the calculated sample size effect is definitely stronger than the measured one.

To correct the experimental data for finite sample size an extrapolation has been made in Fig.21 to 24, using two different concepts:

1.- extrapolation with the theoretical sample size dependence fitted to the experimental data,

2.- linear extrapolation or extrapolation by hand where experimental data are obviously non-linear (B^{10},Ni).

Both extrapolated values are given in Tab.9 and 10; while method 1. appears to be more appropriate for most materials, the comparison gives some idea about the magnitude of possible systematic errors due to the extrapolation procedure.

3.4.2.5 Investigation of Sample Interaction Effects

Some oscillator experiments have been carried out to obtain information on sample interaction effects, i.e. on how strongly the sample worth may be influenced by spectrum and adjoint perturbations due to the presence of other materials in its vicinity.

These measurements were made with enriched uranium (93.14%) foils as a sample which was covered on both sides by platelets of the perturbing material. Two measurements were performed:

1.- shielded case:

ρ_s = reactivity worth of the uranium sample with cover plates minus worth of cover plates alone,

2.- unshielded case:

ρ_o = reactivity worth of the uranium sample alone.

Tab.11 gives the experimental results for a number of cover plate materials. A definite increase in U^{235}-worth was found under C (due to elastic moderation) and depleted uranium (due to additional fast fissions released in the U^{238}). A small opposite effect was observed under Ni where inelastic scattering gives the predominant contribution.

The data found for Fe and stainless steel show that the perturbing effect of the surrounding matrix tubes (2 x 1 mm stainless steel) on the U^{235} sample worth is negligibly small.

3.4.2.6 Derivation of Isotopic Reactivity Worths

For comparison with calculations reactivity worths per atom are considered which have to be derived, in some cases, from measurements with composite samples. We will discuss here the case of U^{235} and U^{238}, whose isotopic reactivity worths ρ^{25}, ρ^{28}, can be obtained from the data of two uranium samples of different enrichment:

$$\begin{aligned} \rho_1 &= N_1^{25}\ \rho^{25} + N_1^{28}\ \rho^{28} \\ \rho_2 &= N_2^{25}\ \rho^{25} + N_2^{28}\ \rho^{28} \end{aligned} \qquad (3.4.20)$$

where ρ_i = reactivity worth per g of sample i,

N_i^x = number of atoms x per g of sample i.

In Eq.(3.4.20) additivity of reactivity worths in the mixture, i.e. absence of interaction effects, has been assumed. This assumption is fulfilled if ρ_1 and ρ_2 are the values correctly extrapolated to zero sample size.

Tab.12 shows the evaluation of ρ^{25} and ρ^{28} from four combinations of four different sample enrichments, using the two extrapolation procedures of Sec.3.4.2.4. Within experimental error, all sample combinations yield the same result. However, there is a rather large influence of the extrapolation procedure on ρ^{28}, showing that linear extrapolation may not be sufficient for determining the U^{238} sample worth.

3.4.2.7 Correction for the Residual Worth in the Out-Position

Due to the experimental technique described in Sec.3.4.2.2, the measured reactivity worth ρ per atom represents the difference of the sample worth at core center, $\rho(o)$, minus the sample worth in the out-position, $\rho^* = \rho(z = 42.5\ cm)$, i.e. in a position 4 cm outside the axial U_{nat} reflector. Hence, the central worth is given by the sum

$$\rho(o) = \rho + \rho^* \qquad (3.4.21)$$

While the residual worth ρ^* can be neglected against ρ for fissile and strongly absorbing materials, this is not the case for typical scattering materials having a central worth ρ close to zero.

The residual worth has been studied recently with the same equipment in a similar assembly [29] by oscillating various samples between the usual out-position (z = 42.5 cm) and a position far away (z = 85 cm). The value ρ^* was found to be predominantly due to neutron backscattering and it was possible to represent the experimental data by the simple expression

$$\rho^* = a\ \rho_d \qquad (3.4.22)$$

where $a = 0.20 \pm 0.02$ and ρ_d is twice the diffusion contribution to the worth per atom as calculated by first-order perturbation theory, Eq.(4.9), for a central column extending over full core height:

$$\rho_d = -\frac{1}{F}\frac{\mu^2}{3}\sum_{j=1}^{26}\frac{\sigma^s_{trj}}{(\Sigma_{trj})^2}\,\phi_j^+(o)\,\phi_j(o), \qquad \mu = \pi/H_{eff} \qquad (3.4.23)$$

This semi-empirical concept based on Eq.(3.4.22) and (3.4.23) was employed to determine the additive correction term ρ^*. The correction is carried out in Tab.13, using the calculated ratio $\rho_d/\rho^{25}(o)$ given in Tab.14. The resulting central worth ratios $\rho(o)/\rho^{25}(o)$ are listed in Tab.15 together with various multigroup calculations. A general discussion follows in Sec.4.3.

3.4.3. Reactivity Worth of Large Samples in the Fast Zone

Reactivity worth measurements have been made for some axially extended samples (CH_2, B_4C, void) in certain positions of the fast zone. For these experiments a stainless steel matrix tube was filled with the sample material and inserted into the fast core, replacing the element filled with normal core material. Usually, the corresponding sample worth was obtained from the change of the critical position of a calibrated control plate; the B_4C-worth was measured directly by dropping the fuel-poison safety rod S_4 (cf. Sec.3.4.13).

In the case of the CH_2-sample an extrapolation procedure was employed which has been described in [5]. The sample was formed by 3 mm thick polythene platelets that were placed into the empty central element in various steps, such that the sample worth was obtained as a function of the axial sample height h. The resulting reactivity per unit mass, ρ/M, was normalized to the corresponding average importance

$$\frac{\rho^*}{M} = \frac{\rho}{M} \Big/ \frac{1}{h} \int_0^h \cos^2\left(\frac{\pi z}{H_{eff}}\right) dz \qquad (3.4.24)$$

and plotted in Fig.25 as a function of sample size. For large samples the ρ^*/M values approach an asymptotic value $(\rho^*/M)_\infty$ from which the worth of a fully extended sample can be derived:

$$\frac{\rho}{M} = \frac{1}{2} \left(\frac{\rho^*}{M}\right)_\infty \qquad (3.4.25)$$

Tab.16 gives a comparison of experimental results with both one-dimensional reactor calculations and with first-order perturbation calculations. As in STARK 3 and 4, the CH_2 worth is underestimated by the reactor calculation [5]. Calculations with first-order perturbation theory give unreliable results, except for the case of the voided central position where agreement within a few percent is observed.

3.5. Pulsed Neutron Source Measurements

Pulsed neutron source measurements were performed to determine the prompt neutron decay constant α and the prompt neutron generation time Λ. The decay of neutron pulses periodically injected into the system was measured with a BF_3-counter in the air gap near the safety plate S_3^3 (Fig.1) and recorded by a 256-channel time analyzer. The experimental set-up and the data evaluation procedure were the same as described in an earlier paper [30].

A compact 100 keV deuteron accelerator with a duoplasmatron ion source [31] was used as pulsed neutron source. The unit was fed through the top shield of the reactor such that the tritium target was located above the fast zone. The pulse repetition rate f = 1/T was 10 sec^{-1}. From the data corrected for dead-time losses and the approximately constant delayed neutron background the fundamental-mode decay constant α was determined.

As derived by Simmons and King [32], the decay constant α is related to the reactivity ρ/β and the generation time Λ by

$$\alpha = \frac{\beta}{\Lambda}\,(1 - \rho/\beta) \qquad (3.5.1)$$

The α-values measured for three reactor configurations near critical ($-30\ ¢ \lesssim \rho/\beta \lesssim -10\ ¢$) are shown in Fig.26 as a function of the reactivity ρ/β determined by the rod drop method (cf.Sec.3.4.1.4). By extrapolation to delayed critical the value $\alpha_c = \beta/\Lambda$ can be found. Because of the curvature of the α vs. ρ/β-curve, i.e. the variation of the generation time Λ with ρ/β, this procedure may be erroneous. From measurements at STARK, assembly 1 to 4 [6] we found that the γ-values obtained by the method of Garelis and Russel [33] were only weakly dependent on reactivity. The quantity γ is the solution of the integral equation

$$\int_0^\infty n_p(t)\ (e^{\gamma t} - 1)\,dt = \int_0^\infty n_d(t)\,dt \qquad (3.5.2)$$

where $n_p(t)$ and $n_d(t)$ are the prompt and delayed neutron populations, respectively.

A Fortran program was used to solve Eq.(3.5.2). The γ-values, which are also shown in Fig.26, can be extrapolated to delayed critical with high precision. Thus, the rather time-consuming measurement at delayed critical could be avoided.

For the critical reactor a value of

$$\alpha_c = 82.1 \pm 0.5 \text{ sec}^{-1}$$

was found. Compared with the values of β/Λ from the 26-group diffusion calculations (Tab.2) a good agreement is observed.

4. Discussion of Results

4.1. Neutron Spectrum in the Fast Zone

The general behavior of the neutron spectrum in STARK 5 is demonstrated in Fig.3, where 26-group fluxes ϕ_i obtained in a one-dimensional diffusion calculation are given for various radial positions. The spectrum in the thermal driver zone follows roughly a 1/E-shape, while, entering into the fast core, a strong attenuation of low-energy neutrons ($E \lesssim 1$ keV) occurs, especially for the thermal group and near the main U^{238} resonance. In the central part of the fast core the spectrum ϕ_i closely approaches the equilibrium spectrum ϕ_i^{as} as calculated for a one-zone all-fast system of the same composition. The deviation of the calculated STARK spectrum at r = o from the equilibrium spectrum is of the order of $\pm$ 1%, except for the very low energy region ($\lesssim$ 10 eV) whose contribution to the reaction rates in the individual reactor materials is negligibly small. In comparison to the earlier STARK assemblies [4,5] a much better spectrum match is obtained because of the hydrogen admixture and the sufficiently high U^{235} concentration in the fast zone.

The analogous diagram for the adjoint flux ϕ_i^+ in Fig.4 shows deviations from the asymptotic adjoint ϕ_i^{+as} of the order of $\pm$ 2%. The increase of ϕ_i^+ relative to ϕ_i^{+as} at high energies (E > 0.5 MeV) is explained by the presence of excess U^{238} in the natural uranium buffer zone.

The influence of heterogeneity on the neutron spectrum is illustrated in Fig.27, which shows the relative deviation of the heterogeneous spectrum, ϕ_i^{het}, from that of a homogeneous one-zone diffusion calculation. ϕ_i^{het} has been calculated by the cell program ZERA [19] for the infinite slab lattice of Fig.2. Fig.27 shows that for energies $E \gtrsim 500$ eV the spatially averaged cell spectrum

$$\left\langle \phi_i^{het} \right\rangle_{cell} = \frac{1}{l} \int_0^l \phi_i(z)\,dz \qquad (4.1)$$

agrees within $\pm$ 2.5 percent with the homogeneous calculation, while at lower energies heterogeneity leads to a pronounced fine structure and to a cell-averaged spectrum considerably softer than that of the homogeneous model.

For the following discussion of the measured differential neutron spectrum at core center, which covers the energy range from 0.03 to 1 MeV, both the deviation from equilibrium and the influence of heterogeneity can be neglected. Fig.13 shows the experimental spectrum compared with a zero-dimensional P_1-calculation with the Karlsruhe 208-group set [20]. In the calculation, pairs of two neighboring group fluxes have been added together to obtain a group width comparable to the energy resolution of the experiment. The comparison shows that the dips due to the Al- and O-resonances agree for both spectra reasonably well in energy.

To discuss the overall shape, both the experimental data and the 208-group fluxes have been collapsed to the 26-group structure of the ABN set. These values are plotted in Fig.28 together with results of one-dimensional radial calculations performed with various 26-group cross section sets.

An intercomparison among the calculated spectra for energies $E \gtrsim 10$ keV shows that the calculations with the improved 26-group sets (SNEAK, MØXTØT, KFKINR) yield quite similar spectra which deviate appreciably from the ABN spectrum and, to a lesser extent, also from the 208-group calculation. The experimental spectrum follows closely the ABN calculation and appears to be definitely harder than the 208-group spectrum and those from the improved 26-group calculations. This is in contrast to observations in STARK 6 [34] where the experimental spectrum agrees very well with the 208-group calculation.

The relatively large differences between the ABN spectrum and those of the improved 26-group sets are mainly due to the different weighting spectra employed, namely a 1/E-spectrum in the ABN set and that of a typical steam-cooled fast reactor (SNEAK 3A-2) in the other sets.

The weighting spectrum is known to have a strong influence on the elastic removal cross section $\Sigma^{el}_{i\to i+1}$; for elastic scattering in the reactor materials except hydrogen, the average logarithmic energy loss ξ is small compared with the lethargy width Δu_i of the groups and one finds for $\Sigma^{el}_s(u) \approx \text{const}$

$$\Sigma^{el}_{i\to i+1} \approx \frac{\xi \Sigma^{el}_s}{\Delta u_i} \frac{\varphi(u_i)}{\langle \varphi(u) \rangle_i} \qquad (4.2)$$

where $\varphi(u_i)$ = weighting spectrum at the low energy end of group i,
$\langle\varphi(u)\rangle_i$ = average of $\varphi(u)$ over group i.

In the ABN set we have $\varphi(u_i)/\langle\varphi(u)\rangle_i = 1$ since $E\varphi(E) = \varphi(u) = \text{const}$; for a typical fast reactor weighting spectrum one has instead

$$\varphi(u_i)/\langle\varphi(u)\rangle_i > 1 \quad \text{for } E \gtrsim 300 \text{ keV},$$
$$\varphi(u_i)/\langle\varphi(u)\rangle_i < 1 \quad \text{for } E \lesssim 300 \text{ keV},$$

i.e. above $\approx$ 300 keV the elastic removal cross section is greater, for $E \lesssim 300$ keV smaller than that of the ABN set.

This is illustrated in Fig.29 where the group transfer cross sections $\Sigma_{i \to i+1}$ of the ABN and the SNEAK set are shown. They are compared with values obtained by condensation of the 208-group calculation, where the uncertainties in the weighting are negligibly small. The 208-group data are seen to agree rather well with the SNEAK data for energies below 200 keV, while for the high energy groups they follow, in general, more closely the ABN values as found recently in calculations for STARK 6 [34].

To eliminate the uncertainty of the weighting spectrum it was attempted to improve the original 26-group SNEAK set by introducing transfer cross sections $\Sigma_{i \to i+1}$ obtained by condensation of a zero-dimensional 208-group calculation. The resulting 208-group spectrum shown in Fig.30 agrees well with the condensed 208-group spectrum in the energy range $E < 800$ keV where the differences in the fission spectrum and the inelastic scattering data of the two sets have only litte influence.

4.2. Reaction Rates and Spectral Indices

Additional information on the neutron spectrum and its spatial variation inside the fast zone may be deduced from individual reaction rates and reaction rate ratios.

Fig.10 shows the radial variation of measured fission rates per atom, $n_f^x(r)$, compared with calculated values derived from the group fluxes $\phi_i(r)$ of the 26-group diffusion calculation:

$$n_f^x(r) = \sum_{i=1}^{26} f_i^x \, \sigma_{fi}^x \, \phi_i(r) \qquad (4.3)$$

where σ_{fi}^{x} = infinite dilute fission cross section } material x,
f_i^x = self-shielding correction factor } group i.

Fission rates of most materials were taken directly from the output of the NUSYS evaluation, while those of U^{234} and Np^{237} not present in all sets were calculated separately from Eq.(4.3), assuming $f_i=1$. The calculated data of Fig.10 have been multiplied by a common normalization factor to obtain agreement with the U^{235}-measurement at core center.

The experimental data of Fig.10 have been obtained with calibrated cylindrical fission chambers (cf.Sec.3.3.1). Despite of some discrepancies with the absolute measurements at core center (Tab.5) the same calibration factors were used as in the measurements on the earlier STARK assemblies [4,5], so that changes from one assembly to another can be observed with an accuracy of about ± 3 percent.

The U^{235} fission rate n_f^{25} in Fig.10 shows, as a result of the strong absorption of low energy neutrons, in the buffer and near the edge of the fast zone a steep gradient which goes over into a relatively flat curve in the interior of the fast core. The experimental data are seen to agree with the theoretical curve for $r \lesssim 12$ cm, while in the outer region they are higher than calculated, indicating that slow neutrons penetrate deeper into the fast core than predicted by the calculation. This discrepancy is thought to be mainly due to the use of the effective group cross section concept in the thermal and epithermal region, which is not suited to describe a typical transmission problem. As discussed in [6], also transport effects play an important role.

For the threshold substances Th^{232}, U^{238} and Np^{237}, relatively flat fission rate traverses were found which extend well into the buffer zone. The shape of the experimental curves is in good agreement with the calculation, but there are rather large deviations in absolute value for Th^{232} and Np^{237} which are similar in magnitude to those in the previous STARK assemblies [4,5]. These discrepancies are probably due to errors in the fission chamber calibration, since a much better agreement is found for the absolute measurements at core center (Tab.5)

Fig.11 and 12 show the radial variation of fission ratios

$$\sigma_f^x / \sigma_f^y = n_f^x / n_f^y \qquad (4.4.)$$

relative to U^{235} and U^{238}.

As spectral indices sensitive to the eV region, the fission ratios Pu^{239}/U^{235} and U^{233}/U^{235} are plotted in Fig.11. The maxima in the calculated curves are due to the fact that thermal neutrons are more strongly absorbed in the natural uranium zone than eV neutrons that cause fission in the lower Pu^{239}- and U^{233}-resonances. Towards the interior of the fast core the eV neutrons die out and the fission ratios go over into the values characteristic of the fast spectrum. The experimental data of Fig.11 show spatially constant fission ratios in the central region, $r \lesssim 10$ cm, which indicates that an equilibrium spectrum has been reached there. In the outer region, however, $\sigma_f^{49}/\sigma_f^{25}$ is higher than calculated which gives another indication that the penetration of low energy neutrons is stronger than expected from theory.

The fission ratios of threshold substances (Th^{232}, U^{238} and Np^{237}) relative to U^{235}, as plotted in Fig.12, also show space-independent values in the central region and characteristic deviations from the calculation in the outer part which are a consequence of the stronger penetration of slow neutrons. The fission ratio σ^{37}/σ^{28} between the threshold substances Np^{237} and U^{238} follows an almost space-independent shape throughout the entire fast zone, showing that important changes in the high energy part of the spectrum do not occur.

The fission ratios measured with absolute parallel-plate chambers at core center are compared in Tab.5 with various 26-group calculations. Measurements have been made with two sets of fission samples, namely the old set used in the earlier STARK and SNEAK assemblies, and a new set of standards whose effective masses have been checked by various independent methods [22]. For the following discussion only the data obtained with the new samples are considered.

The U^{233}/U^{235} ratio is found to agree reasonably well with calculations with the SNEAK, MØXTØT and KFKINR sets, whereas the ABN set underestimates this quantity considerably. The ratios of threshold

substances (U^{234}, U^{236} and U^{238}) relative to U^{235} in general are overestimated by the ABN set and strongly underestimated by the MØXTØT set, while a better overall agreement is obtained with the KFKINR and SNEAK calculations. This observation agrees with the general results found recently in the assembly STARK 6 [34].

The experimental fission ratios between two threshold substances, which are sensitive to the slope of the spectrum at the high energy end ($E \gtrsim 0.5$ MeV), agree better with the ABN calculation than with any of the improved 26-group calculations. Neither the introduction of the transfer cross sections $\Sigma_{i \to i+1}$ from the 208-group calculation into the SNEAK or KFKINR set nor the direct evaluation with the 208-group spectrum leads to a better agreement.

In contrast to STARK 6 [34], where the ratios U^{234}/U^{238} and U^{236}/U^{238} agree with the 208-group calculation within $\pm$ 2 percent, here these quantities were found to be 4 to 6 percent above the corresponding calculation. Considering the group contributions to the fission rates shown in Fig.31, we have to conclude that the slope at the high-energy end of the spectrum (ABN-groups 3 to 6) is steeper than that given by the 208-group calculation.

Tab.5 also contains a comparison between central fission ratios in STARK 5 with those for a one-zone fast system of the same composition, as obtained from 26-group calculations with the SNEAK set. For all isotope combinations, the deviations stay within $\pm$ 0.5 percent, i.e. they are much smaller than the experimental error. The STARK 5 fission ratios can therefore be considered as identical to those in the center of an all-fast system of the same core composition.

The results of the In sandwich measurements in Tab.6 show that the neutron flux at 1.46 eV is largely underestimated by the homogeneous calculation. This discrepancy is greatly reduced when the spectrum of the heterogeneous ZERA calculation is used.

4.3. Reactivity Worth of Material Samples in the Fast Zone

The reactivity worths of samples measured by the pile oscillator technique and extrapolated to zero sample size (Sec.3.4.2) are compared in Tab.13 with the results of homogeneous first-order perturbation calculations performed with different cross section sets. The calculated reactivity worth per atom is given by

$$\rho = \rho_a + \rho_f + \rho_m + \rho_d \qquad (4.5)$$

where

$$\rho_a = \frac{1}{F} \sum_{i=1}^{26} \phi_i^+ \sigma_{ai}^s \phi_i \qquad (4.6)$$

$$\rho_f = \frac{1}{F} \sum_{i,j=1}^{26} \phi_j^+ \chi_j \nu \sigma_{fi}^s \phi_i \qquad (4.7)$$

$$\rho_m = \frac{1}{F} \sum_{i,j=1}^{26} (\phi_j^+ - \phi_i^+) \sigma_{i\to j}^s \phi_i \qquad (4.8)$$

are the contributions of neutron absorption, fission and moderation and σ_{ai}^s, σ_{fi}^s, $\sigma_{i\to j}^s$ are the effective microscopic cross sections of the sample material for absorption, fission and transfer from group i to group j. F is the so-called normalization integral defined in Sec.2.

The diffusion term

$$\rho_d = -\frac{1}{3F} \sum_{j=1}^{26} \frac{\sigma_{trj}^s}{(\Sigma_{trj})^2} (\nabla\phi_j^+, \nabla\phi_j) \qquad (4.9)$$

vanishes in the isotropic neutron field at core center (σ_{trj}^s = transport cross section of the sample).

The dilute sample cross sections (σ_{ai}^s etc) are calculated by the perturbation code from differences between the effective macroscopic cross sections of the homogeneous core mixture, to which the sample material has been added in low concentration, and those of the unperturbed core mixture. These differences therefore include the effect of the sample on the self-shielding in the other core materials. The individual contributions ρ_f, ρ_a and ρ_m are given in Tab.14 as obtained in a calculation with the H2ØPMB set.

In addition, the dependence of the calculated worths on the sample concentration N_s has been investigated. For strong resonance absorbers like Ta it was found necessary to use sample concentrations not higher than 10^{19} atoms/cm^3 in order to exclude self-shielding in the sample material. For the scattering substances of low reactivity worth (Al, C etc.), however, concentrations of 10^{20} atoms/cm^3 have been chosen to keep rounding errors sufficiently small. Except for U^{238}, the resulting reactivity worths are found to agree within $\pm$ 2 percent with the integral transport calculation extrapolated to zero sample size.

A discussion of the calculated group contributions to reactivity (cf.Fig.32 and 33) shows that the homogeneous model ist fully adequate for most sample materials; only in case of B^{10} and Ta the energy region below 1 keV gives measurable contributions such that heterogeneity effects cannot be neglected (cf.Fig.32).

In general, a comparison between measured and calculated sample worths provides an additional check of the quality of the calculation and allows in simple cases, on the basis of Eq.(4.6) to (4.8), to draw conclusions about the energy dependence of the real or adjoint spectrum, ϕ_i or ϕ_i^+, or about the cross sections of the sample material.

The reactivity worth of U^{235}, the principal fissile material in the reactor, is almost exclusively given by the contributions ρ_f and ρ_a (Tab.14). As seen in Tab.15, the calculated values ρ^{25} show a marked variation with the cross section set, mainly due to the dependence of F on the fuel mass in the thermal driver needed to render k_{eff}=1.

To be independent of the F-value of the particular calculation, we compare in the following the reactivity worth ratios relative to U^{235}, ρ^x/ρ^{25}, which may be considered as indices characterictic of the energy dependence of the real and adjoint spectra. The use of U^{235} as a reference substance is suggested by the fact that it is the main fissile material in the reactor and that the influence of the sample environment on its worth is rather small as demonstrated in Tab.11.

Tab.15 shows that also the calculated reactivity worth ratios depend appreciably on the cross section set used. In general, the best overall agreement with experiment is obtained for the calculations with the SNEAK and KFKINR sets, while the original ABN set gives the largest deviations. In the following, some of the individual results shall be discussed briefly, distinguishing four groups of materials.

1.- Fissile materials (U^{235}, Pu):

For the fissile materials the quantities ρ_f and ρ_a in Eq.(4.5) are the leading terms; sample size effects are relatively small. The group contributions to ρ_f and ρ_a for U^{235} are shown in Fig.32. With the given real and adjoint spectra, Fig.3 and 4, the reactivity ratio ρ^{Pu}/ρ^{25} depends mainly on the shape of ϕ_i, while that of the adjoint has only a minor influence. One finds from Tab.15 that ρ^{Pu}/ρ^{25} depends only slightly on the cross section set and that the calculations with the SNEAK, MØXTØT and KFKINR sets agree sufficiently well with the experiment.

2.- Strongly absorbing materials (B^{10},Ta):

Here the reactivity worth is almost completely due to the absorption term ρ_a (Tab.14) and one finds again that the influence of the adjoint is not very pronounced; self-shielding in the low energy region leads to a strong sample size dependence. Tab.15 shows for Ta a satisfactory agreement with the improved 26-group calculations, while for B^{10} all calculated values are definitely lower than the experiment. From Fig.32 one finds that the low energy region, where heterogeneity cannot be neglected, gives a measurable contribution to ρ_a, even the region below 10 eV. A reevaluation with the cell-averaged spectrum of the ZERA calculation, Fig.27, leads to 5 percent higher B^{10} worths and reduces the discrepancy considerably.

3.- Moderating materials

For these substances the moderation effect ρ_m is at least comparable to ρ_a. As one finds from Eq.(4.8), the slope of the adjoint, $\phi_i^+ - \phi_j^+$, enters as a factor such that positive as well as negative group contributions may arise (cf.Fig.33). Hence, one expects the resulting net effect ρ_m to depend strongly on the shape of the adjoint spectrum. Considering further the marked variation of ρ_{mi} from one

group to the next (Fig.33), one can hardly expect that the 26-group division used in our calculations is fine enough to allow a precise description of the moderation effect. These considerations are confirmed by the data of Tab.15 where the calculated worths of typical scatterers like Al,C, H and O are seen to depend strongly on the cross section set used.

The best general agreement with experiment is obtained for the KFKINR set. Here, substantial deviations (>5 percent) exist for the group of light nuclei (Al, C, O), where positive and negative values of ρ_{mi} compensate to a large extent, and for H whose worth is underestimated by all calculations in accordance with observations in other assemblies [34].

In the group of the heavier nuclei one finds a satisfactory agreement ($\pm$ 5 percent) for Cr, Fe, Mo and Ni. In contrast to this, large deviations from experiment are found for Nb (+ 25 percent) and Zr (- 25 percent), which cannot be explained by sample size effects. Hence, one has to consider the possibility that the cross section data of these two materials are in error.

4.- U-238

For this material the three effects ρ_f, ρ_a and ρ_m are comparable in magnitude (Tab.14), such that definite conclusions can hardly be drawn from the worth measurement. Due to the high U^{238}-concentration in the core mixture, a strong resonance self-shielding occurs, even in case of thin samples, which may be the reason for the 10 percent discrepancy between the integral transport calculation and first-order perturbation theory. As seen in Tab.15, the experimental worth agrees best with the SNEAK and H2ØPM calculations if the calculated sample size dependence is adopted, whereas a linear sample size extrapolation leads to a better agreement with the KFKINR calculation.

5. Conclusions

The analysis of the STARK 5 experiments shows that both the integral parameters of the entire assembly and the data measured in the interior of the fast zone are reasonably well described by standard 26-group diffusion calculations, while characteristic deviations remain in the transition region between the thermal driver and the fast core. In particular, the following principal results are summarized:

1.- The influence of the cross section set on the calculated spectral indices and material worths at core center were found to be rather large. The best overall agreement with experiment is consistently obtained with the KFKINR set, while the ABN and the MØXTØT set give larger deviations.

2.- The differential neutron spectrum measured at core center in the energy range from 30 keV to 1 MeV appears to be somewhat harder than the calculation with the Karlsruhe 208-group set. This observation is, at least qualitatively, supported by the fission ratio measurements. It should be pointed out that both quantities show a much better agreement in STARK 6 [34], a similar assembly having a higher uranium enrichment and a considerably lower U^{238} concentration.

3.- An investigation of the spatial variation of spectral indices shows that the spectrum in the central region of STARK 5 does not measurably deviate from the equilibrium spectrum, in accordance with multigroup calculations which give deviations of $\pm$ 1 percent for the entire energy range down to 10 eV.

4.- Special emphasis was put on the further development of the square-wave pile oscillator technique to measure reactivity worths of samples. In order to avoid systematic errors, the following steps had to be taken:

a.- use of an oscillator rod filled with core material to prevent streaming effects and spectral distortion,

b.- consideration of the effect of finite sample size,

c.- correction for the residual sample worth in the out-position, which was necessary because of the limited stroke of the present oscillator system.

5.- Except for H and B^{10}, the measured sample size dependence is well represented by a 26-group collision probability calculation such that an extrapolation to zero sample mass can be made with sufficient accuracy. For the majority of substances the extrapolated worths deviate by less than 5 percent from first-order perturbation calculations with the KFKINR set. Larger discrepancies are found for typical scatterers (Al, C, H), and especially for Nb and Zr where the deviation is thought to be due to cross section errors.

References

/1/ MEISTER, H., et al.: Sicherheitsbericht für den gekoppelten schnell-thermischen Argonaut-Reaktor Karlsruhe (STARK), March 1964, unpublished

/2/ MEISTER, H., K.H. BECKURTS, W. HÄFELE, W.H. KÖHLER, and K. OTT: The Karlsruhe Fast-Thermal Argonaut-Reactor Concept, KFK-217, Kernforschungszentrum Karlsruhe (1964)

/3/ BRÜCKNER, Chr., G. KUSSMAUL, H. MEISTER and D. STEGEMANN: Die Ladung 1 (Natururanladung) des Schnell-Thermischen Argonaut-Reaktors Karlsruhe, STARK, unpublished

/4/ BARLEON, L., et al. (compiled by H. MEISTER): Untersuchungen an der Ladung 2 des Schnell-Thermischen Argonaut-Reaktors STARK, KFK-592, Kernforschungszentrum Karlsruhe (1967)

/5/ BARLEON, L., et al (compiled by G. KUSSMAUL, and H. MEISTER): Untersuchungen an den Ladungen 3 und 4 des Schnell-Thermischen Argonaut-Reaktors STARK, KFK-668, Kernforschungszentrum Karlsruhe (1967) and EUR-3701d.

/6/ BARLEON, L., et al.: Evaluation of Reactor Physics Experiments on the Coupled Fast-Thermal Argonaut Reactor STARK, KFK-482, Kernforschungszentrum Karlsruhe (1966) and ANL-7320

/7/ ABAGJAN, L.P., et al.: Gruppenkonstanten schneller und intermediärer Neutronen für die Berechnung von Kernreaktoren, KFK-tr-144, Kernforschungszentrum Karlsruhe (1964)

/8/ BACHMANN, H., et al.: The Cross Section Set KFK-SNEAK Preparation and Results, KFK-628, Kernforschungszentrum Karlsruhe (1967)

/9/ HUSCHKE, H.: Gruppenkonstanten für dampf- und natriumgekühlte schnelle Reaktoren in einer 26-Gruppendarstellung; KFK-770, Kernforschungszentrum Karlsruhe (1968)

/10/ PÖNITZ, W.P.: Some New Measurements and Renormalizations of Neutron Capture Cross Section Data in the keV Energy Range, KFK-635, Kernforschungszentrum Karlsruhe (1967)

/11/ KIEFHABER, E. et al.: Evaluation of Fast Critical Experiments by Use of Recent Methods and Data, BNES Conf. on The Physics of Fast Reactor Operation and Design, London (1969)

/12/ MOXON, M.C.: UKAEA-Report AERE-R 6074 (1969)

/13/ KIEFHABER, E.: to be published as KFK Quarterly Report

/14/ AVERY, R.: Theory of Coupled Reactors, Proc.Second U.N. International Conference on the Peaceful Uses of Atomic Energy 12, 182 (1958)

/15/ KEEPIN, G.R.: Physics of Nuclear Kinetics, Addison-Wesley Publishing Company, Inc., Reading, Ma.(1965)

/16/ BATCHELOR, R., and H.R. McHYDER, J.Nucl.Energy 3,7 (1956)

/17/ KUSSMAUL, G.: Ermittlung der Spektren χ_{ij} der verzögerten Neutronen für den 26-Gruppen-ABN-Satz, unpublished

/18/ FISCHER, E.A.: A Method to Calculate Reactivity Worth by Integral Transport Theory, KFK-995, Kernforschungszentrum Karlsruhe (1969)

/19/ WINTZER, D.: Heterogeneity Calculations Including Space Dependent Resonance Self-Shielding, KFK-633 (1967), and Fast Reactor Physics II, Vienna, p.237-255 (1968)

/20/ HUSCHKE, H.: Die Beschreibung der Datei GRUBA für 208 Energiegruppen, unpublished

/21/ BECKURTS, K.H., and K. WIRTZ: Neutron Physics, Springer Verlag (1964)

/22/ KUHN, D.: unpublished

/23/ BENJAMIN, P.W., et al.: The Use of a Gas-Filled Spherical Proportional Counter for Neutron Spectrum Measurements in a Zero Energy Fast Reactor, AWRE Report No.NR 2/64 (1964)

/24/ KUSSMAUL, G.: Reaktivitätsmessungen am STARK, unpublished

/25/ KUSSMAUL, G.: Prompt Jump Correction of Inverse Kinetics Rod Drop Measurements, Nucl.Sci.Eng.40, 494 (1970)

/26/ JOHN, M.N.: The Response of the Reactor Kinetic Equations to Square Wave Oscillations of Reactivity, AEEW-M 193 (1962)

/27/ KUSSMAUL, G., and H. MEISTER: Material Worth Measurements with a Fuel-Filled Pile Oscillator Rod, to be published in Journal of Nucl.Energy (1971)

/28/ FRISCH, O.R., and LITTLER, D.J.:Phil.Mag.7, p.45 (1954)

/29/ MEISTER, H., et al.: to be published

/30/ EDELMANN, M., G. KUSSMAUL, H. MEISTER, D. STEGEMANN,and W. VÄTH: Pulsed Source and Noise Measurements on the STARK-Reactor at Karlsruhe, KFK-473, Kernforschungszentrum Karlsruhe (1965) and IAEA-Proceedings on Pulsed Neutron Research, Vol.II, 799 (1965)

/31/ EYRICH, W., and A. SCHMIDT: Two Compact High-Intensity Pulsed Neutron Sources, KFK-304, Kernforschungszentrum Karlsruhe (1965) and IAEA-Proceedings on Pulsed Neutron Research, Vol.II, 589 (1965)

/32/ SIMMONS, B.E., and S.J. KING: Nucl.Sci.Eng.3, 595 (1958)

/33/ GARELIS E., and J.L. RUSSEL jr.: Nucl.Sci.Eng.16, 263 (1963)

/34/ MEISTER, H., et al.: Investigation of Reactor Physics Properties of the SNEAK 3A-2 Core in the Fast Thermal Reactor STARK, Assembly 6, to be published as KFK-Report.

Tab. 1 Atom densities($10^{20}/cm^3$) of STARK 5 used for homogeneous calculations

Zone No.	1	2	3	4	5	6	7
Zone	Fast core	Natural uranium	Graphite+ tank walls	Thermal core	Graphite	Graphite + tank walls	Graphite reflector
Outer radius	18.6 cm	24.2 cm	30.5 cm	R +)	46.06 cm	50.06 cm	86.06 cm
Material							
Al	164.13		92.643	129.95		72.60	
C	8.38		492,25	169.96	852.55	428.91	852.55
Cr	12.71						
Fe	41.80						
H	16.35		3.680	360.44		5.267	
Ni	10.54						
O	72.76			193.74			
U-235	31.665	3.437		1.0151			
U-238	224.70	473.94		4.0556			

+) Values obtained from radius variation ($k_{eff} = 1$):

ABN : R = 40.243 cm

SNEAK: R = 39.905 cm

H2ØPMB: R = 39.857 cm

MØXTØT: R = 39.561 cm

KFKINR: R = 39.480 cm

Tab. 2 Experimental reactor parameters compared with 26-group diffusion calculations

	Measurement	ABN-set	SNEAK-set	H2Ø-PMB-set	MØXTØT-set	
Criticality data:						
Fuel mass, fast core	80.658					kg U^{235}
Fuel enrichment, fast core	12.35	12.35	12.35	12.35	12.35	weight %
Fuel mass, therm.core(20°C)	5.031±0.04	5.234	5.028	4.999	4.820	kg U^{235}
Fuel mass, therm.core(80°C)	5.614±0.04	-	-	-	-	kg U^{235}
Deviation of calc.k_{eff} from exp.	-	- 0.87	+ 0.01	+ 0.12	+0.79	% k
Power contributions:						
Fast core, γ_1	21.4 ±1.0	22.22	19.63	19.23	21.93	%
Uranium zone, γ_2	11.1 ±1.0	11.04	10.58	10.63	10.66	%
Reactivity contributions:						
Fast core, α_1	-	28.66	23.55	23.07	27.47	%
Uranium zone, α_2	-	12.27	11.52	11.63	11.66	%
Reactivity worths, fast zone:						
Central elements vs. void	+0.27 ±0.01	+ 0.280[1)]				% k
Worth of safety rod S_4	-0.737±0.010	- 0.782				% k
Reactivity worths, therm.zone:						
Worth of outer fuel plate	+0.081±0.010	+ 0.067				% k
Void coefficient	-0.103±0.010	- 0.144[1)]				%k/%void
Worth of temp.change 80→20°C	+0.583±0.005	-				% k
Worth of 1 control plate	-0.318±0.005	-				% k
Worth of all 12 control plates	-3.47 ±0.2	-				% k
Kinetic parameters:						
Generation time Λ	9.00 ±0.10	9.052	9.631	9.719	9.243	$\times 10^{-5}$ sec
$\beta^{25}_{eff} / \beta_{eff}$	-	0.801	0.836	0.837	0.828	
$\beta^{28}_{eff} / \beta_{eff}$	-	0.199	0.164	0.163	0.172	
β_{eff}	-	7.389	7.323	7.326	7.327	$\times 10^{-3}$

1) Perturbation calculation

Tab. 3 Kinetic parameters of STARK 5 used for the reactivity evaluations (diffusion calculation with ABN-set)

Isotope	k	λ_k [sec^{-1}]	$\beta_{eff\ k}$
U^{235}	1	0.0124	$2.028 \cdot 10^{-4}$
	2	0.0305	$1.334 \cdot 10^{-3}$
	3	0.111	$1.177 \cdot 10^{-3}$
	4	0.301	$2.399 \cdot 10^{-3}$
	5	1.13	$6.917 \cdot 10^{-4}$
	6	3.00	$2.526 \cdot 10^{-4}$
U^{238}	1	0.0132	$1.678 \cdot 10^{-5}$
	2	0.0321	$1.830 \cdot 10^{-4}$
	3	0.139	$2.107 \cdot 10^{-4}$
	4	0.358	$5.265 \cdot 10^{-4}$
	5	1.41	$3.013 \cdot 10^{-4}$
	6	4.02	$1.004 \cdot 10^{-4}$
	Delayed neutron fractions:		
U^{235}	$\beta^{25}_{eff} = \sum_{k=1}^{6} \beta^{25}_{eff\ k} = 6.057 \cdot 10^{-3}$		
U^{238}	$\beta^{28}_{eff} = \sum_{k=1}^{6} \beta^{28}_{eff\ k} = 1.339 \cdot 10^{-3}$		
Total	$\beta_{eff} = \beta^{25}_{eff} + \beta^{28}_{eff} = 7.396 \cdot 10^{-3}$		
	Prompt neutron generation time:		
	$\Lambda = 8.958 \cdot 10^{-5}$ sec		

Tab. 4 Power contributions of the individual reactor zones of STARK 5

	Power fraction, ax. integrated	Power fraction in reactor midplane	
	fission chamber measurement	fission chamber measurement	Diffusion calcul. with ABN-set
Fast core:			
core, U^{235}	0.165	0.179	0.1825
core, U^{238}	0.033	0.035	0.0399
blanket, U^{235}	0.002	-	
blanket, U^{238}	0.004	-	
total:	0.204	0.214	0.2224
Buffer zone:			
U^{235}	0.082	0.067	0.0638
U^{238}	0.048	0.044	0.0465
total:	0.130	0.111	0.1103
Thermal zone:			
U^{235}, thermal	0.615	0.622	0.6068
U^{235}, epitherm.	0.051	0.053	0.0605
total:	0.666	0.675	0.6673

Tab. 5 Fission ratios σ_f^x / σ_f^y in the center of STARK 5

Isotope ratio	Absolute fission chamber		26-group diffusion calculation (...) = calc./exp.						0-dim. 208-group calculat.	Ratio STARK 6 / 1-Zone-syst.
	old fission standards	new fission standards	ABN	SNEAK	H2ØPMB	MØXTØT	KFKINR	SNEAK 2)		
Th^{232}/U^{235}	(0.00767)	-	0.00659	0.00625	0.00627	0.00586	0.00651	0.00648	-	0.997
U^{233}/U^{235}	(1.522)	1.566±0.025	1.460 (0.932)	1.595 (1.018)	1.669 (1.066)	1.598 (1.020)	1.617 (1.032)	1.598 (1.020)	-	1.001
U^{234}/U^{235}	-	0.245±0.004	0.2489 (1.016)	0.2257 (0.921)	0.2276 (0.929)	0.2057 (0.839)	0.2231 (0.911)	0.2319 (0.948)	-	0.997
U^{236}/U^{235}	-	0.0740±0.0015	0.0775 (1.047)	0.0707 (0.955)	0.0709 (0.958)	0.0636 (0.859)	0.0706 (0.954)	0.0716 (0.968)	-	0.996
U^{238}/U^{235}	(0.0354)	0.0318±0.0005	0.03351 (1.054)	0.03121 (0.981)	0.03128 (0.984)	0.02860 (0.899)	0.03106 (0.977)	0.03220 (1.012)	-	0.996
Pu^{239}/U^{235}	1.013±0.020 1)	-	1.0336 (1.020)	0.9965 (0.984)	1.0360 (1.022)	0.9784 (0.966)	1.0209 (1.008)	1.0041 (0.991)	-	1.000
Pu^{240}/U^{235}	-	-	0.2602	0.2359	0.2378	0.2225	0.2423	0.2406	-	0.997
U^{234}/U^{238}	-	7.69±0.15	7.427 (0.966)	7.232 (0.940)	7.276 (0.946)	7.193 (0.935)	7.183 (0.934)	7.203 (0.936)	7.380 (0.960)	1.001
U^{236}/U^{238}	-	2.33±0.05	2.312 (0.992)	2.266 (0.972)	2.268 (0.973)	2.224 (0.954)	2.275 (0.976)	2.224 (0.962)	2.212 (0.949)	1.000

1) Cylindrical fission chamber

2) Modified by introducing $\Sigma_{i \to i+1}$ from 208-group calculation

Tab. 6 Activity ratio C_o/C_i (outer to inner foil) for indium sandwiches compared with various 26-group calculations

Foil thickness /mg/cm²/	Pos.	r /cm/	Experimental C_o/C_i	Cross section set	Calculated C_o/C_i	calc.flux at 1.46 eV / exp. flux at 1.46 eV
3 x 83.8	36	16.2	1.409±0.005	ABN[1]	1.186	0.18
3 x 83.5	32	10.8	1.148±0.005	ABN[1]	1.027	0.14
3 x 82.6	26	5.4	1.076±0.005	ABN[1]	1.009	0.12
3 x 82.5	19	0	1.061±0.005	ABN[1]	1.0069	0.11
				SNEAK[1]	1.0124	0.20
				MØXTØT[1]	1.0133	0.22
				KFKINR[1]	1.0134	0.2
				SNEAK[2]	1.022	0.36
				SNEAK[3]	1.030	0.49

1) Homogeneous diffusion calculation

2) ZERA calculation (spatially averaged spectrum)

3) ZERA calculation (spectrum at CH_2-foil)

Tab. 7 Reactivity of control and safety units

Plate Rod	Series No.	Detector Pos. No.	RD Measurement ρ/ß [¢]	Contin.insertion Final value ρ/ß [¢]
R_1	1	1	- 0.428	-
R_2	1	1	- 0.400	- 0.395
S_3^3	1	1	- 0.393	-
S_4	1	1	- 0.996	- 0.989
R_1	2	1	- 0.418	- 0.442
R_2	2	1	- 0.394	- 0.387
R_2	2	2	- 0.397	-
R_3	2	1	- 0.472	- 0.468
R_3	2	2	- 0.467	- 0.453
3R+9S	2	2	- 4.7	-

Tab. 8 Reactivity worth of a 19.8% enriched Uranium sample obtained by Fourier analysis and inverse kinetics evaluation of pile oscillator measurements.

Harmonics index k	Uranium sample (250.09 g U; 19.8 w/o U^{235})		
	C_k/i_o [10^{-3}]	$\frac{\Delta_M}{ß} = 2\frac{\rho_M}{ß}$ [¢]	$\Delta_M = 2\rho_M$ [10^{-5} Δk/k]
1	15.659	1.0659	7.8833
2	1.059	-	-
3	3.374	1.0693	7.9089
4	0.614	-	-
5	1.769	1.0730	7.9358
6	0.422	-	-
7	1.164	1.0544	7.7987
1 (drift corrected)	15.550	1.0646	7.8736
Inverse kinetics values	1^{st} period (1.0647 ± 0.0013) ¢		
	2^{nd} period (1.0643 ± 0.0018) ¢		

Tab. 9 Reactivity worth of samples in the center of STARK 5 measured by the pile oscillator method.

Material	Sample weight [g]	Experimental sample worth[1] [10^{-7} k/g]	Extrapolated sample worth		
			Experimental data		Integr.transp. calculation
			[10^{-7} k/g]	[$\Delta k/10^{30}$ atoms]	[$\Delta k/10^{30}$ at.]
B[2]	0.333	-461.8±7.0			
	0.972	-417.8±4.0	- 510 [3]	- 854 [3]	- 725
	1.729	-400.6±2.0	- 478 [4]	- 800 [4]	
	2.807	-390.8±2.0			
$(CH_2)_n$	3.11	+114.6±0.8	+ 103 [3]	+ 240 [3]	
	6.245	+126.2±0.4	+ 94 [4]	+ 218 [4]	+ 220.0
Fe	51.11	-1.212±0.03	- 1.32 [3]	- 12.2 [3]	
	102.19	-1.106±0.015	- 1.342 [4]	- 12.45 [4]	- 11.59
Ni	38.84	- 1.749±0.04			
	77.78	- 1.687±0.02	- 1.84 [3]	- 17.9 [3]	
	123.4	- 1.607±0.01	- 2.02 [4]	- 19.7 [4]	- 17.44
	246.7	- 1.485±0.01			
	493.7	- 1.378±0.005			
Ta	53.74	- 7.292±0.04	- 8.08 [3]	- 242.7 [3]	
	107.10	- 6.535±0.03	-11.48 [4]	- 344.8 [4]	- 335.8
U(0.4%)	124.13	- 1.300±0.03	- 1.31 [3]	- 51.8 [3]	
	247.95	- 1.290±0.02	- 1.39 [4]	- 54.9 [4]	- 57.73
	372.08	- 1.272±0.01			
U_{nat}	125.30	- 1.239±0.03	- 1.25 [3]	- 49.4 [3]	
	250.61	- 1.240±0.02	- 1.33 [4]	- 52.6 [4]	- 55.02
	375.91	- 1.224±0.01			
U(19.84%)	125.04	+ 2.915±0.03	+ 2.88 [3]	+ 113.8 [3]	
	250.09	+ 2.952±0.02	+ 2.833 [4]	+ 112.0 [4]	+ 108.5
U(35%)	124.95	+ 6.106±0.06	-	-	-
U(93.14%)	3.586	+ 18.45±0.30	+ 18.45 [3]	+ 721.4 [3]	
	7.247	+ 18.44±0.15	+ 18.53 [4]	+ 724.5 [4]	+ 724.5
	14.335	+ 18.45±0.12			
	21.634	+ 18.67±0.10			
	29.483	+ 18.60±0.08			
	36.656	+ 18.73±0.08			

(continuation on next page)

Tab. 9 (Continuation)

Material	Sample weight [g]	Experimental sample worth[1] [$10^{-7}\Delta k/g$]	Extrapolated sample worth		
			Experimental data		
			[$10^{-7}\Delta k/g$]	[$k/10^{30}$ atoms]	
Pu [5]	1.510	+ 26.5±1.2	+ 25.7 [3]	+ 1020 [3]	
	2.470	+ 25.8±0.8			
	4.891	+ 27.0±0.5			

1) Values are reactivity differences between core center and out-position (z=42.5 cm)

2) Composition of B-sample: 92.15 at.% B^{10}, 7.85 at.% B^{11}

3) Extrapolation by hand for B and Ni, all others are linearly extrapolated

4) Extrapolation by normalization of calculated sample size dependence on the experimental data

5) Composition of Pu-sample: 91.48% Pu^{239}, 7.69% Pu^{240}, 0.80% Pu^{241}, 0.03% Pu^{242}.

Tab. 10 Reactivity worth of samples in the center of STARK 5 measured by the pile oscillator method

Material	Sample weight /g/	Experimental sample worth[1] /10^{-7} k/g/	Extrapolated sample worth		
			Experimental data		Integr.transp. calculation
			/10^{-7} k/g/	/Δk/10^{30}at./	/Δk/10^{30}atoms/
Al	34.86	- 1.33±0.02	- 1.40 [4]	- 6.27 [4]	- 5.618
C	43.86	- 0.554±0.01	-	- 1.105 [2]	- 1.843
Cr	36.89	- 1.138±0.03	- 1.242 [4]	- 10.73 [4]	- 9.708
Mo	102.27	- 2.949±0.01	- 3.61 [4]	- 57.5 [4]	- 56.34
Mn	21.99	- 1.540±0.03	-	- 14.05 [2]	-
Nb	56.43	- 4.036±0.02	- 4.88 [4]	- 75.28 [4]	- 92.51
W	62.55	- 2.891±0.03	-	- 88.29 [2]	-
Zr	42.10	- 1.312±0.02	- 1.455 [4]	- 22.04 [4]	- 16.38
Al_2O_3	78.39	- 1.191±0.01	-	-	-
Fe O	85.03	- 1.211±0.01	-	-	-
SS	53.90	- 1.251±0.02	-	-	-
B10			- 558 [3]	- 928 [3]	
H			+ 722.4 [3] + 656.0 [4]	+ 120.5 [3] + 109.5 [4]	
U^{235}			+20.0±0.1 [3]	+ 780.5 [3]	
			+20.1±0.1 [4]	+ 784.4 [4]	
U^{238}			-1.403± 0.020 [3]	- 55.46 [3]	
			-1.484± 0.020 [4]	- 58.66 [4]	
Pu^{239}			+ 27.5 [3]	+ 1090 [3]	

1) Values are reactivity differences between core center and out-position (42.5 cm)
2) Not extrapolated
3) Using experimental sample size dependence
4) Using calculated sample size dependence

Tab. 11 Reactivity worth of enriched uranium foils (U 93.14%) covered on both sides with platelets of different materials

Cover material	Thickness	U-sample weight	Reactivity worth		Ratio
			shielded	unshielded	
		[g]	[10^{-7} k/g]	[10^{-7} k/g]	
C	2 x 6 mm	14.18	18.90±0.08	18.48±0.08	1.023±0.007
Fe	2 x 6 mm	14.18	18.75±0.08	18.48±0.08	1.014±0.007
SS	2 x 6 mm	14.18	18.63±0.08	18.48±0.08	1.008±0.007
Ni	2 x 6 mm	14.18	18.20±0.06	18.48±0.08	0.985±0.007
Ni	2 x12 mm	14.34	17.74±0.08	18.48±0.08	0.960±0.007
Ni	2 x12 mm	21.63	17.73±0.08	18.67±0.08	0.950±0.007
$U_{depl.}$	2 x 3 mm	6.91	18.72±0.10	18.44±0.10	1.016±0.01
$U_{depl.}$	2 x 3 mm	14.18	18.83±0.06	18.48±0.08	1.019±0.07
$U_{depl.}$	2 x 9 mm	14.34	18.74±0.06	18.48±0.08	1.014±0.07

Tab. 12 Evaluation of isotopic reactivity worths ρ^{25} and ρ^{28} from uranium sample measurements

Pair of samples	Linear extrapolation		Extrapolation with calculated curve	
	ρ^{25}	ρ^{28}	ρ^{25}	ρ^{28}
	[10^{-7}k/g]	[10^{-7}k/g]	[10^{-7}k/g]	[10^{-7}k/g]
U 19.84%/U_{nat}:	+20.19±0.20	-1.404±0.035	+20.28±0.20	-1.485±0.035
U 35% /U_{nat}:	+20.06±0.20	-1.403±0.035	-	-
U 93.14%/U_{nat}:	+19.91±0.10	-1.402±0.035	+20.00±0.10	-1.483±0.035
U 93.14%/U19.84%:	+19.91±0.10	-1.33 ±0.30	+19.99±0.10	-1.42 ±0.30
Average [10^{-7}/g]	+20.0 ±0.1	-1.403±0.020	+20.1 ±0.1	-1.484±0.020
Isotopic reactivity worth [Δk/10^{30} atoms]:	+ 780.5	- 55.46	+ 784.4	- 58.66

Tab. 13 Correction of central reactivity worths for residual worth at z = 42.5 cm

	Measured worth ratio	Correction term, Eq. (3.4.22)	Corrected worth ratio
	ρ/ρ^{25}	$\rho^*/\rho^{25}(o)$	$\rho(o)/\rho^{25}(o)$
Al	- 0.0080	0.0012	- 0.0068
B^{10}	- 1.183	0.0016	- 1.178
C	- 0.0014	0.0013	- 0.0001
CH_2	+ 0.306	0.0035	+ 0.309
Cr	- 0.0137	0.0014	- 0.0123
Fe	- 0.0159	0.0013	- 0.0146
H	+ 0.153	0.0011	+ 0.154
Mo	- 0.0733	0.0025	- 0.0706
Ni	- 0.0251	0.0020	- 0.0231
Nb	- 0.0960	0.0026	- 0.0931
O	- 0.0028	0.0014	- 0.0014
Ta	- 0.440	0.0029	- 0.435
Zr	- 0.0281	0.0025	- 0.0256
U^{235}	1.000	0.0033	1.000
U^{238}	- 0.0748	0.0031	- 0.0715
Pu	+ 1.300	0.0033	+ 1.299

Tab. 14 Individual contributions to sample worth according to Eq.(4.5)
(perturbation calculation with H2ØPMB set)

	Worth at core center $\langle \Delta k/10^{30} \text{atoms} \rangle$				Central column	$(\rho/\rho^{25})_{\text{STARK}}$
Material	$\rho_f(o)$	$\rho_a(o)$	$\rho_m(o)$	$\rho(o)$	$\rho_d/\rho^{25}(o)$	$(\rho/\rho^{25})_{1\text{-Zone}}$
Al	0.1284	- 1.5896	- 3.8100	- 5.2711	0.00592	1.077
B^{10}	4.4682	- 749.78	- 0.3439	- 745.66	0.00824	0.998
C	0.3894	- 1.6046	- 0.7081	- 1.9233	0.00662	1.683
Cr	0.4795	- 4.4375	- 5.3713	- 9.3292	0.00728	1.089
Fe	0.7833	- 6.3782	- 5.4073	- 11.002	0.00644	1.021
H	1.6185	- 6.4414	+ 100.10	+ 95.282	0.00561	1.050
Mo	1.6310	- 41.050	- 12.957	- 52.976	0.01237	1.003
Nb	0.7460	- 74.743	- 12.542	- 86.540	0.01307	0.995
Ni	1.4179	- 15.120	- 3.4985	- 17.201	0.01011	1.001
O	0.3108	- 1.6881	- 0.6044	- 1.9817	0.00723	1.522
Pu	1664.5	- 667.29	- 8.8123	+ 988.37	0.01650	0.995
Ta	4.2095	- 299.84	- 20.781	- 316.41	0.01434	0.999
U^{235}	1406.6	- 670.50	- 12.030	+ 724.08	0.01641	1.000
U^{238}	51.731	- 84.423	- 19.375	- 52.066	0.01544	1.009
Zr	0.6379	- 8.4135	- 7.7784	- 15.554	0.01270	1.016

Tab. 15 Central reactivity worth ratios of samples extrapolated to zero sample size (calculations for critical systems obtained by radius variation)

	Experiment			26-group perturbation calculation									
				ABN set		SNEAK set		H2ØPMB set		MØXTØT set		KFKINR set	
	$\rho(o)/\rho^{25}(o)$	1)	rel. error /%/	ρ/ρ^{25}	calc./exp.	ρ/ρ^{25}	calc./exp.	ρ/ρ^{25}	calc./exp.	ρ/ρ^{25}	calc./exp.	ρ/ρ^{25}	calc./exp.
Al	- 0.0068	c	5	- 0.00603	0.887	- 0.00723	1.063	- 0.00736	1.082	- 0.00555	0.816	- 0.00636	0.935
B^{10}	- 1.100	c	2	- 0.8206	0.746	- 0.9599	0.873	- 1.0355	0.941	- 1.0708	0.973	- 1.0580	0.962
	- 1.178	e			0.697		0.815		0.879		0.909		0.898
	- 1.178	e						- 1.083[3]	0.919[3]			- 1.107[3]	0.940[3]
C	- 0.0001	n	-	+ 0.00028	-	-0.00364	-	- 0.00284	-	- 0.00059	-	- 0.00085	-
CH_2	+ 0.308	e	1	+ 0.2079	0.675	+ 0.2130	0.692	+ 0.2604	0.845	+ 0.2534	0.823	+ 0.2804	0.910
Cr	- 0.0123	c	5	- 0.01350	1.098	- 0.01275	1.037	- 0.01302	1.059	- 0.01154	0.938	- 0.01266	1.029
Fe	- 0.0146	c	3	- 0.01208	0.827	- 0.01460	1.000	- 0.01520	1.041	- 0.01341	0.918	- 0.01429	0.979
H	- 0.154	e	1	+ 0.1038	0.674	+ 0.1083	0.703	+ 0.1316	0.855	+ 0.1270	0.825	+ 0.1406	0.913
Mo	- 0.0706	c	2	- 0.06245	0.885	- 0.06883	0.975	- 0.07316	1.036	- 0.07087	1.004	- 0.07459	1.056
Ni	- 0.0231	c	3	- 0.02157	0.934	- 0.02336	1.011	- 0.02376	1.029	- 0.02235	0.968	- 0.02319	1.004
Nb	- 0.0934	c	2	- 0.09907	1.061	- 0.11140	1.193	- 0.11952	1.280	- 0.11960	1.281	- 0.12016	1.287
O	- 0.0014	n	–	- 0.00049	0.350	- 0.00296	2.114	- 0.00301	2.150	- 0.00219	1.564	- 0.00072	0.514
Ta	- 0.435	c	2	- 0.3469	0.797	- 0.4056	0.932	- 0.4370	1.005	- 0.4449	1.023	- 0.4515	1.038
								- 0.457[3]	1.050[3]			- 0.472[3]	1.085[3]
Zr	- 0.0256	c	4	-0.01943	0.759	- 0.02082	0.813	- 0.02148	0.839	- 0.01931	0.754	- 0.02046	0.799
U^{238}	- 0.0715	c	2	-0.06036	0.844	- 0.07105	0.994	- 0.07191	1.006	- 0.06513	0.911	- 0.06541	0.915
	- 0.0676	e	2		0.893		1.051		1.064		0.963		0.968
Pu[2]	+ 1.299	e	1	+1.3882	1.069	+ 1.3067	1.006	+ 1.3650	1.051	+ 1.2951	0.997	+ 1.3255	1.020
U^{235}	U^{235}-worth /$\Delta k/10^{30}$ atoms/:												
	786	c	1	936.6	1.192	754.8	0.960	724.6	0.922	897.1	1.141	871.8	1.109

1) Mode of extrapolation: c: using calculated curve, e: using experimental curve, n: not extrapolated
2) Composition cf.Tab.9 and 10
3) Heterogeneous calculation

Tab. 16 Reactivity worth of large samples in the fast core of STARK 5

	Pos.	$\vec{r}$ / cm /	Reactivity worth $\Delta k/\bar{k}$		
			Measurement	Diffusion calculation (ABN set)	Perturbation calculation
Central element filled with CH_2, replacing normal element:	19	0	+1.71±0.15	+ 1.104	+ 0.595
Central element without CH_2-platelets, replacing normal element:	19	0	-0.024±0.002	-	- 0.0210
Normal central element, replacing void:	19	0	+0.27±0.01	-	+ 0.280
Safety rod S_4 (filled with B_4C), replacing normal core mixture:	19 6	0 10.8	- -0.737±0.010	- 0.848 - 0.782	- 1.212 - 1.117

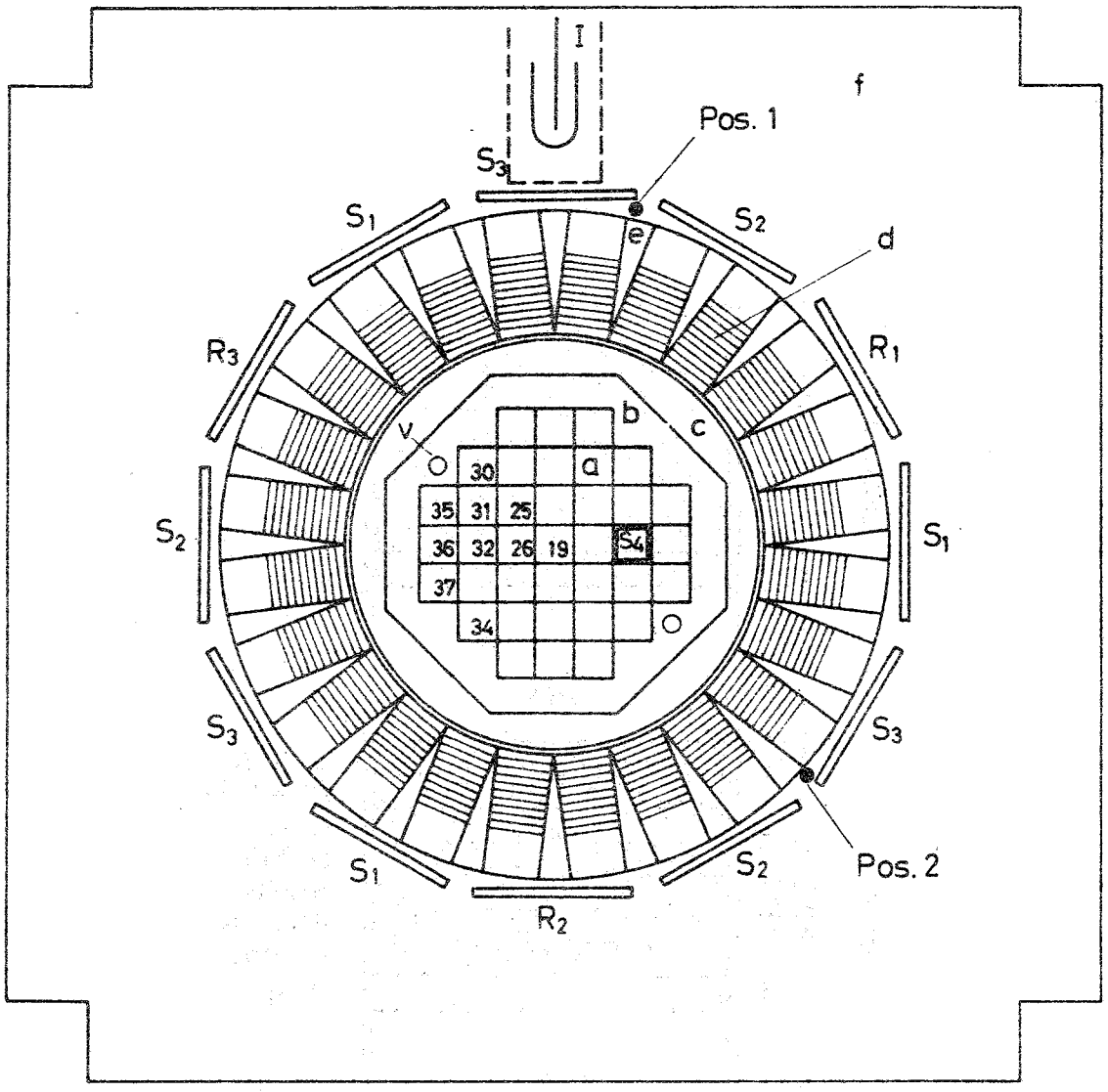

Fig. 1 Schematic cross section of STARK

a - fast core
b - natural uranium zone
c - graphite region
d - thermal core (fuel region)
e - thermal core (graphite pieces)
f - graphite reflector
v - vertical channel

19; 25; 26 ... matrix positions for fission chamber and foil measurements

R_1, R_2, R_3 - fine-control plates

S_1, S_2, S_3 - safety plates

S_4 - fuel-poison safety rod

● - He^3-detector positions

I - B-ionization chamber

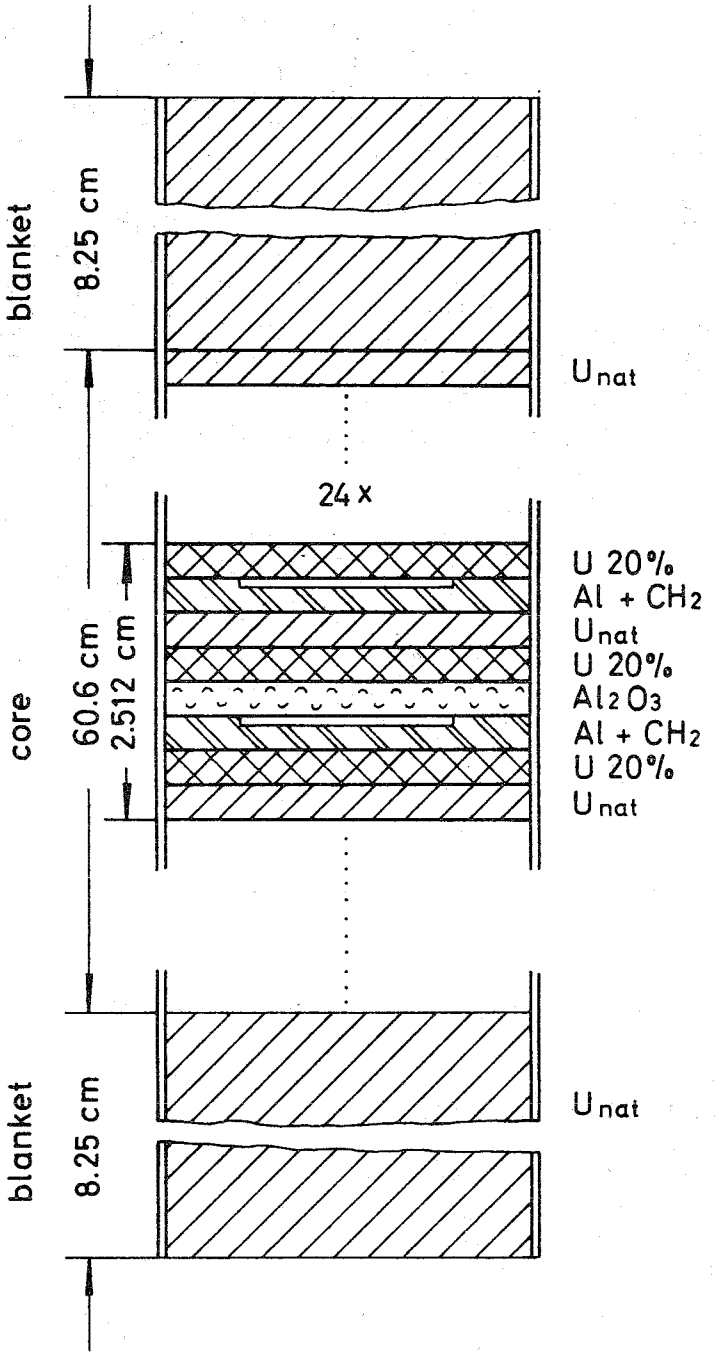

Fig. 2 Loading pattern of the fast core elements

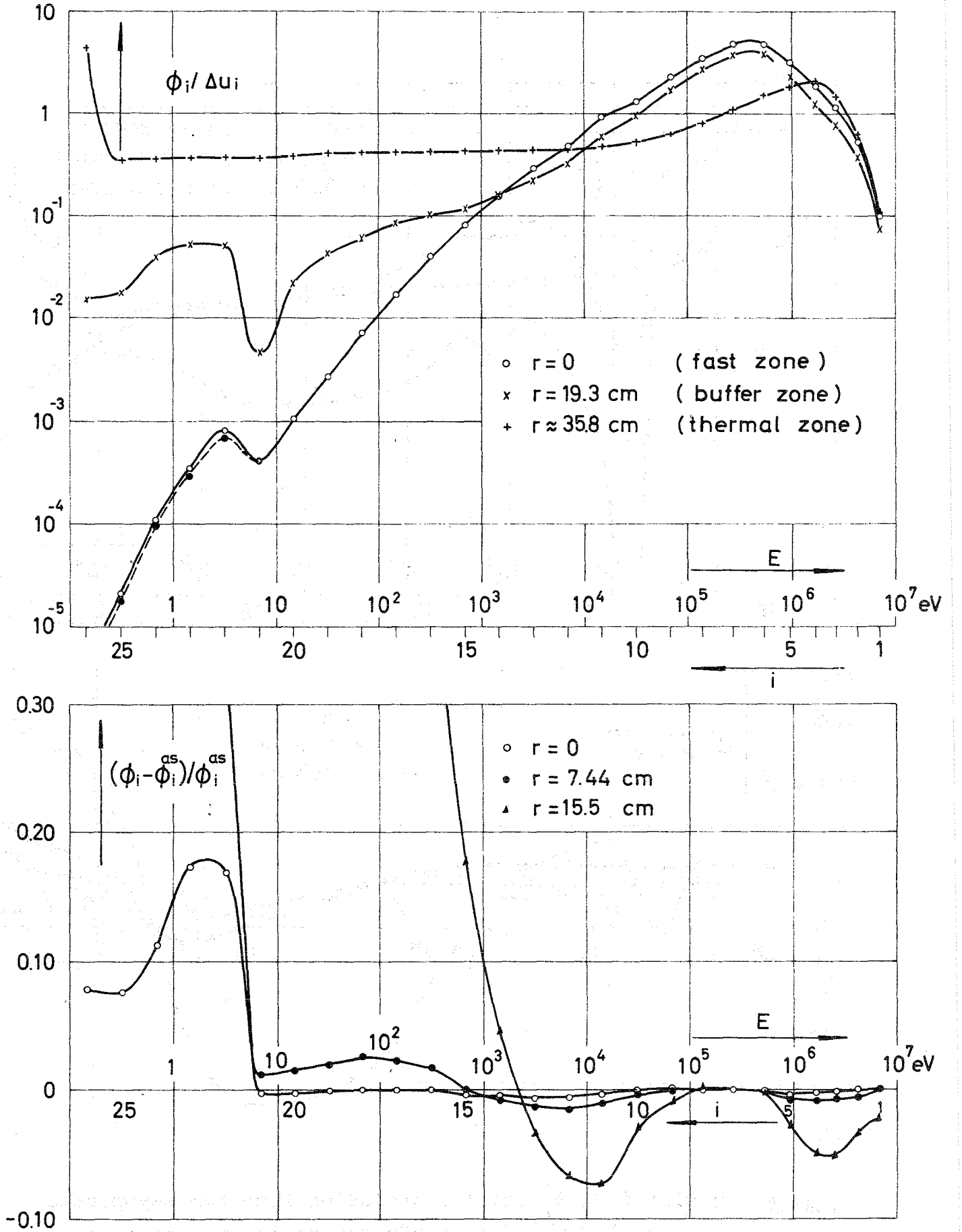

Fig. 3 Neutron spectrum ϕ_i and its deviation from the equilibrium spectrum ϕ_i^{as} at different radial positions r in STARK 5

——— STARK spectrum } diffusion calculation
– – – – – equilibrium spectrum } with 26-group ABN set

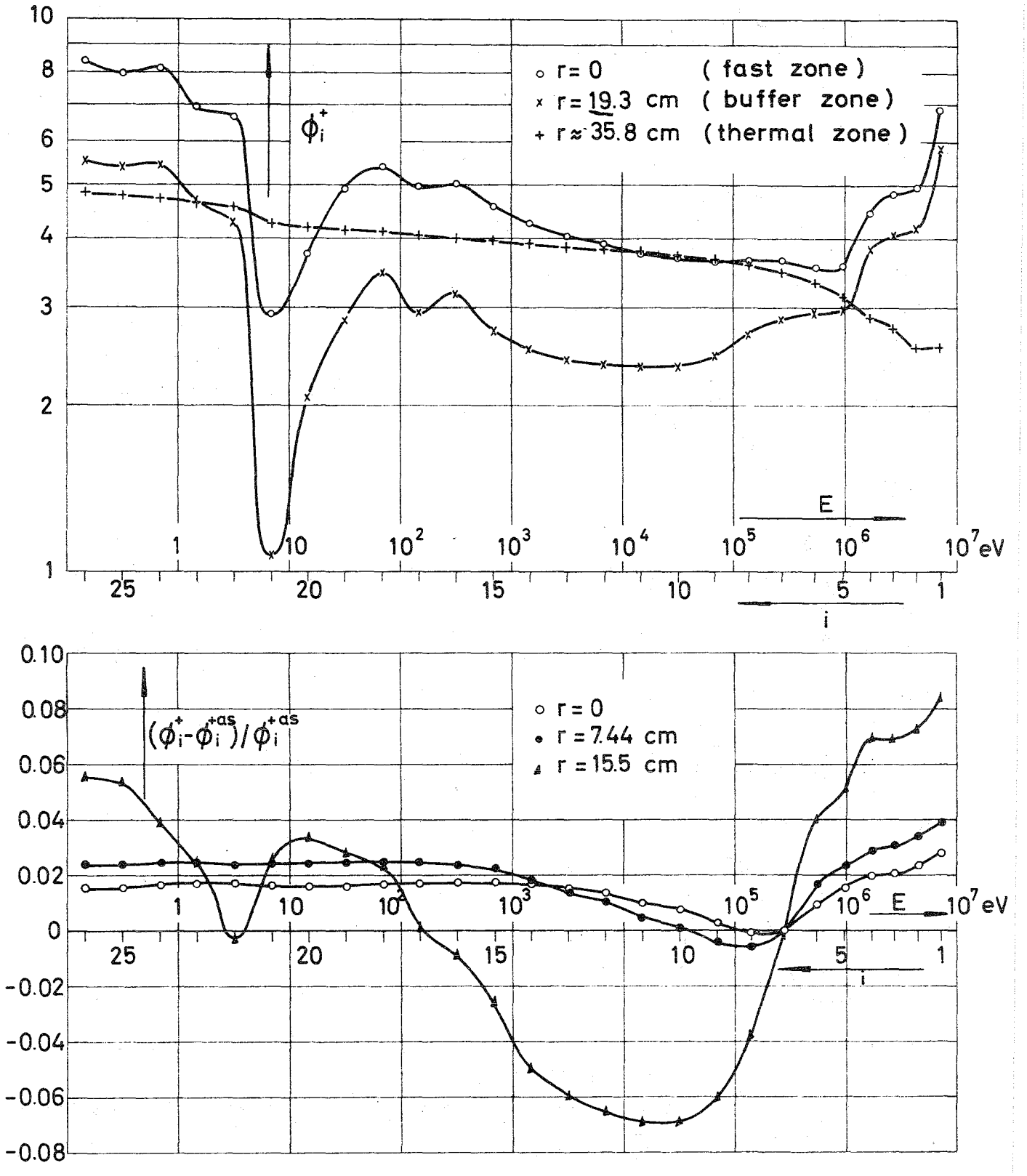

Fig. 4 Adjoint flux ϕ_i^+ and its deviation from the asymptotic adjoint flux ϕ_i^{+as} at different radial positions in STARK 5 (diffusion calculation with 26-group ABN-set)

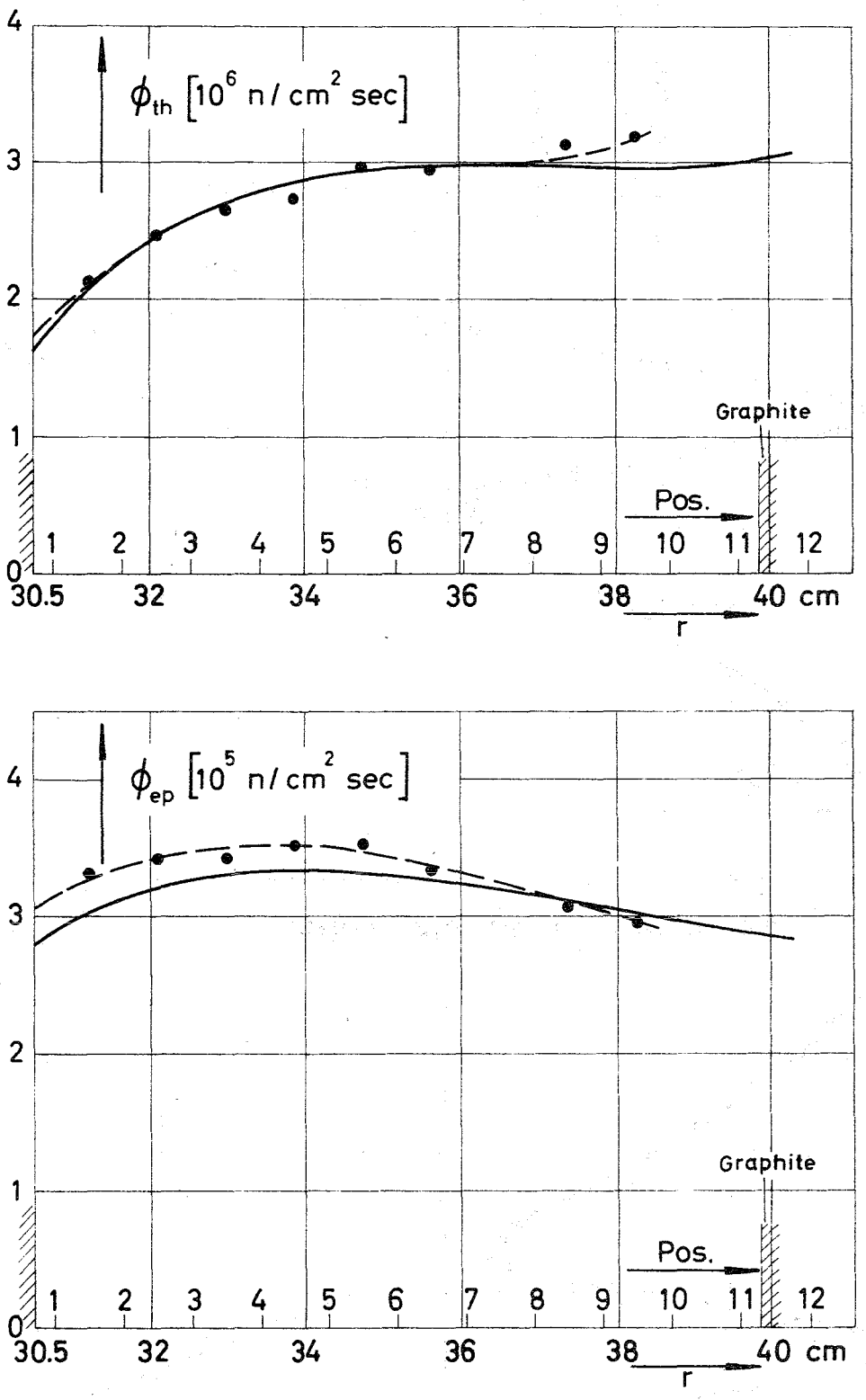

Fig. 5 Radial distribution of the thermal and epithermal flux in the thermal core at 1 Watt reactor power

— —●— — measurement with Au + Cu foils

——— diffusion calculation with 26-group ABN set

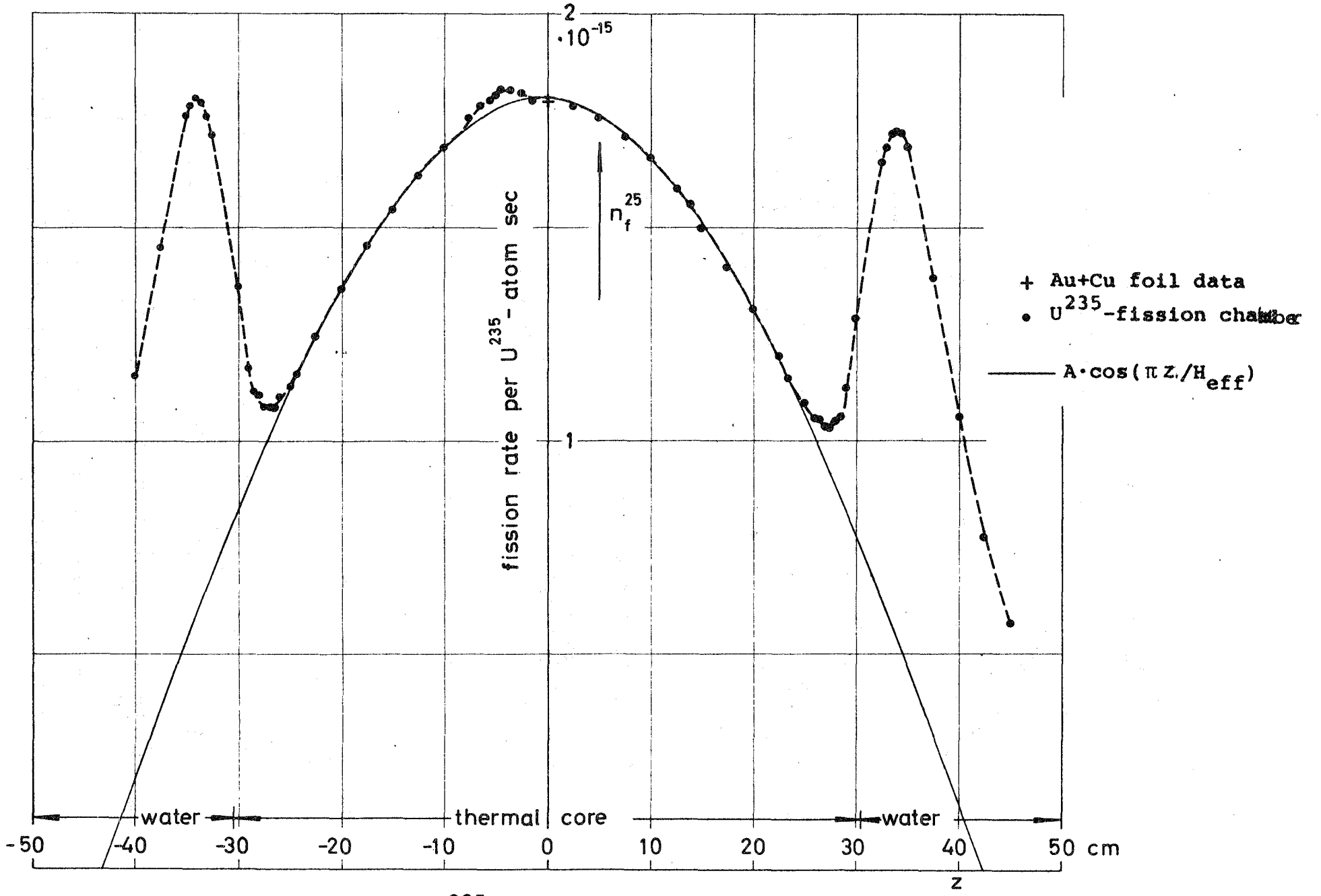

Fig. 6: Axial distribution of the U^{235}-fission rate in the thermal core (r=34.8 cm) at 1 Watt reactor power

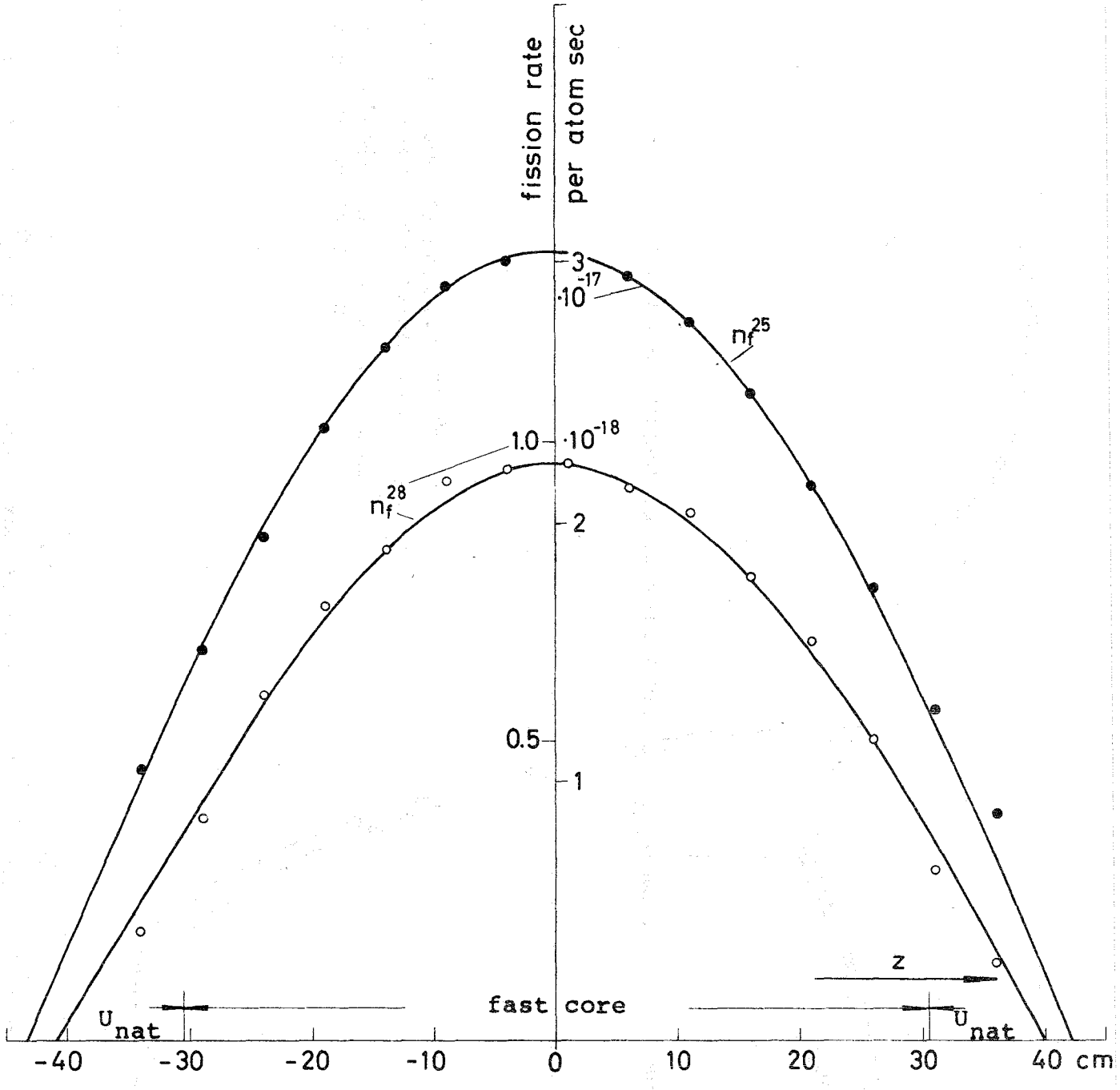

Fig. 7 Axial distribution of U^{235}- and U^{238} fission rates per atom, n_f^{25} and n_f^{28}, in the central position of the fast zone at 1 Watt reactor power

- • U^{235} fission chamber traverse
- ○ U^{238} fission chamber traverse
- ——— A cos ($\pi z / H_{eff}$) fitted to experimental data

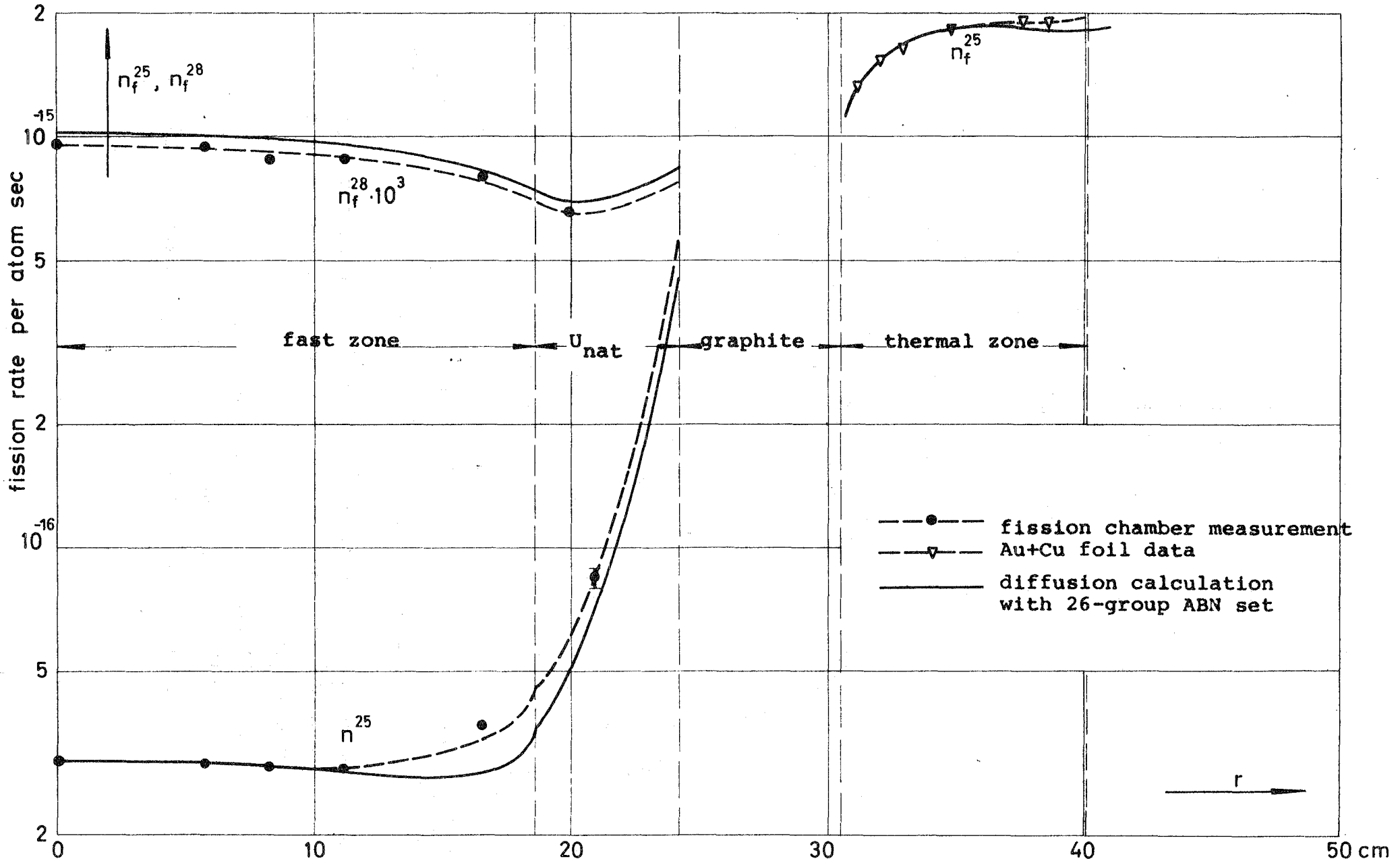

Fig. 8 Radial distribution of U^{235}- and U^{238} fission rates per atom, n_f^{25} and n_f^{28}, in the midplane of STARK 5 at 1 Watt reactor power

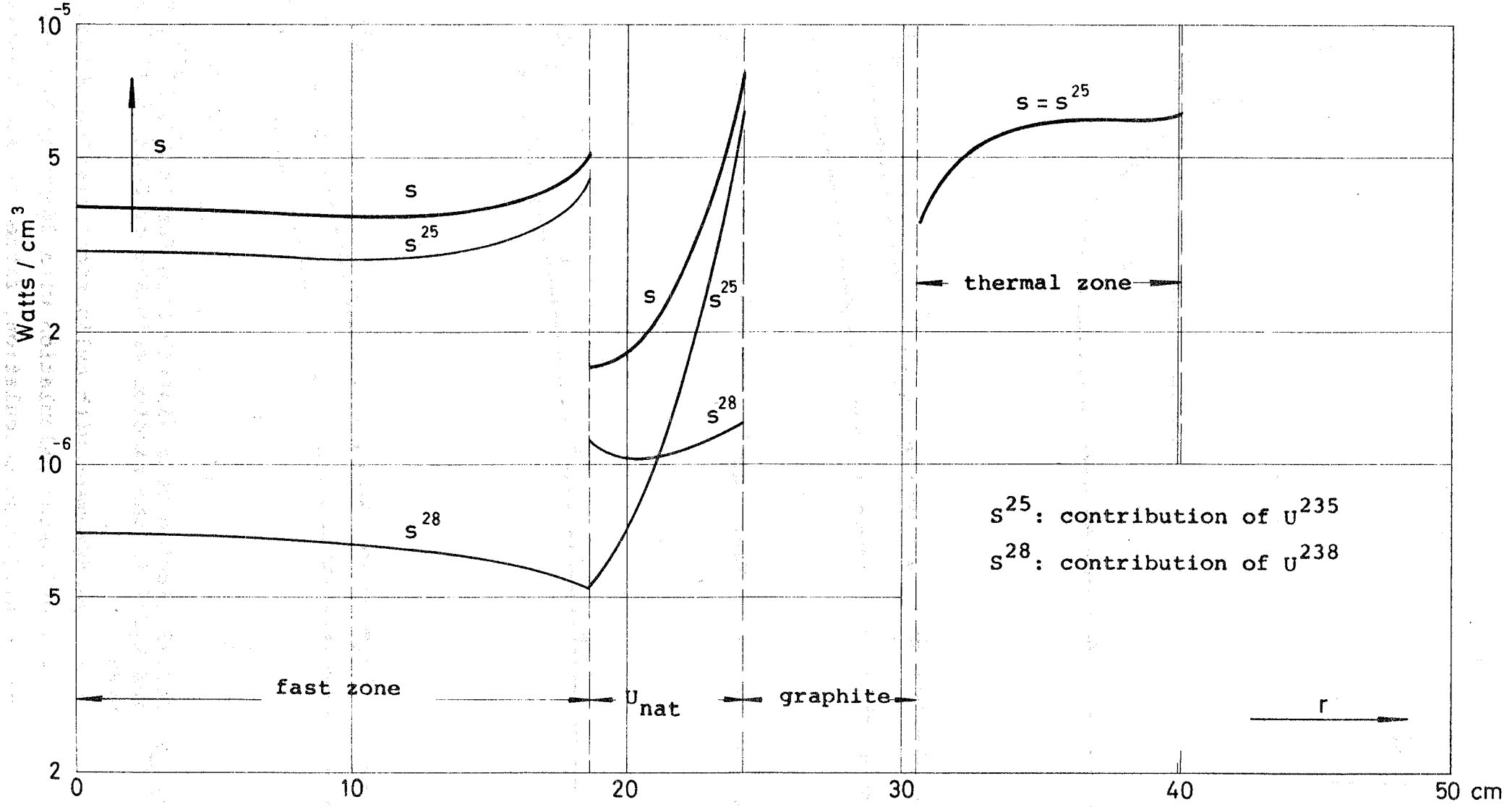

Fig. 9 Radial power distribution S(r) per unit core volume from fission chamber measurement (Fig. 8) at 1 Watt reactor power

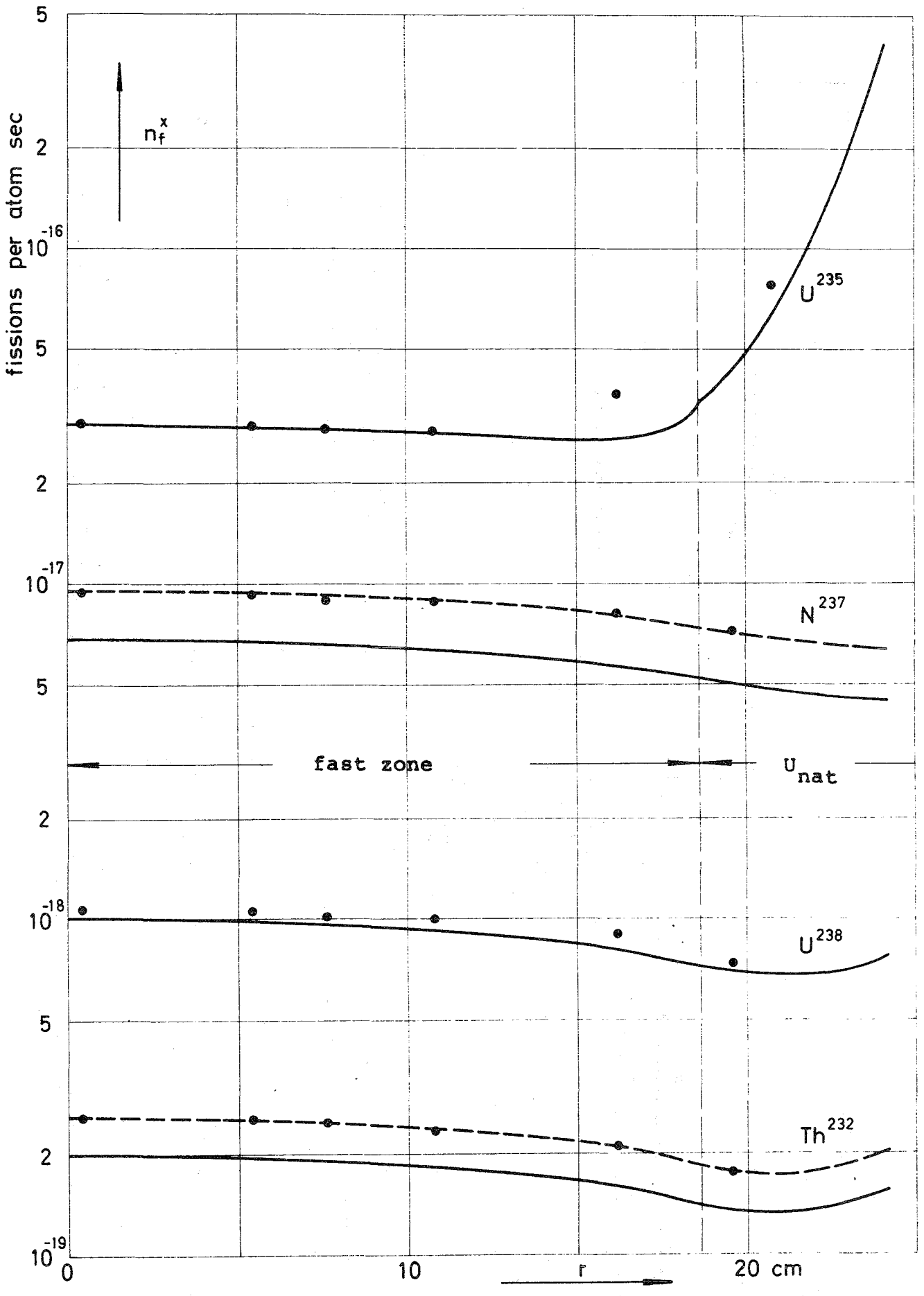

Fig. 10 Radial fission rate distribution for Th^{232}, U^{235}, U^{238}, and Np^{237} in the reactor midplane of STARK 5 at 1 Watt power

o measurement with cylindrical fission chamber

——— diffusion calculation with 26-group ABN set

– – – – diffusion calculation, fitted to experimental data

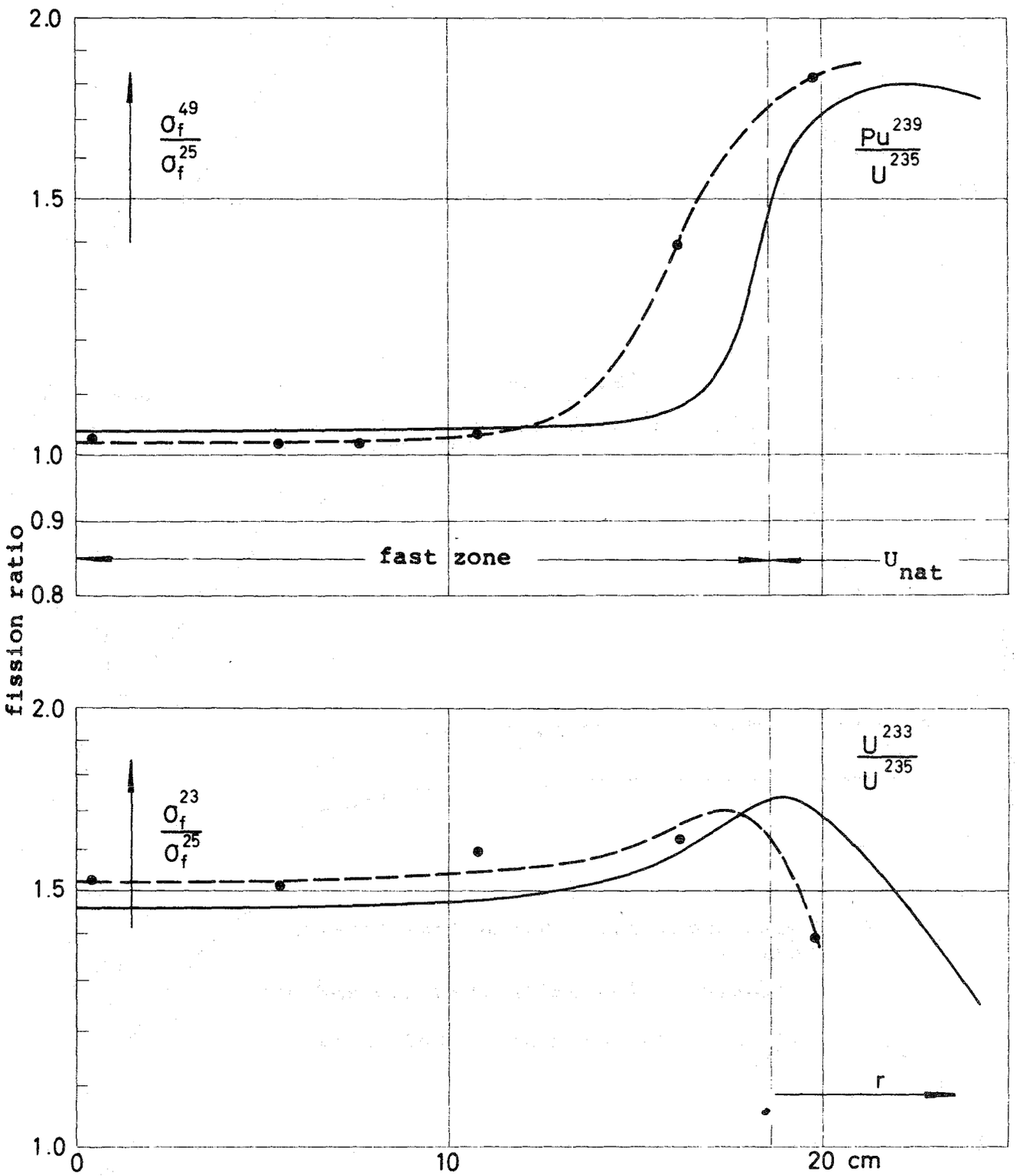

Fig. 11 Radial dependence of Pu^{239}/U^{235}- and U^{233}/U^{235}-fission ratios in the midplane of STARK 5

—●— measurement with cylindrical fission chamber

——— diffusion calculation with 26-group ABN set

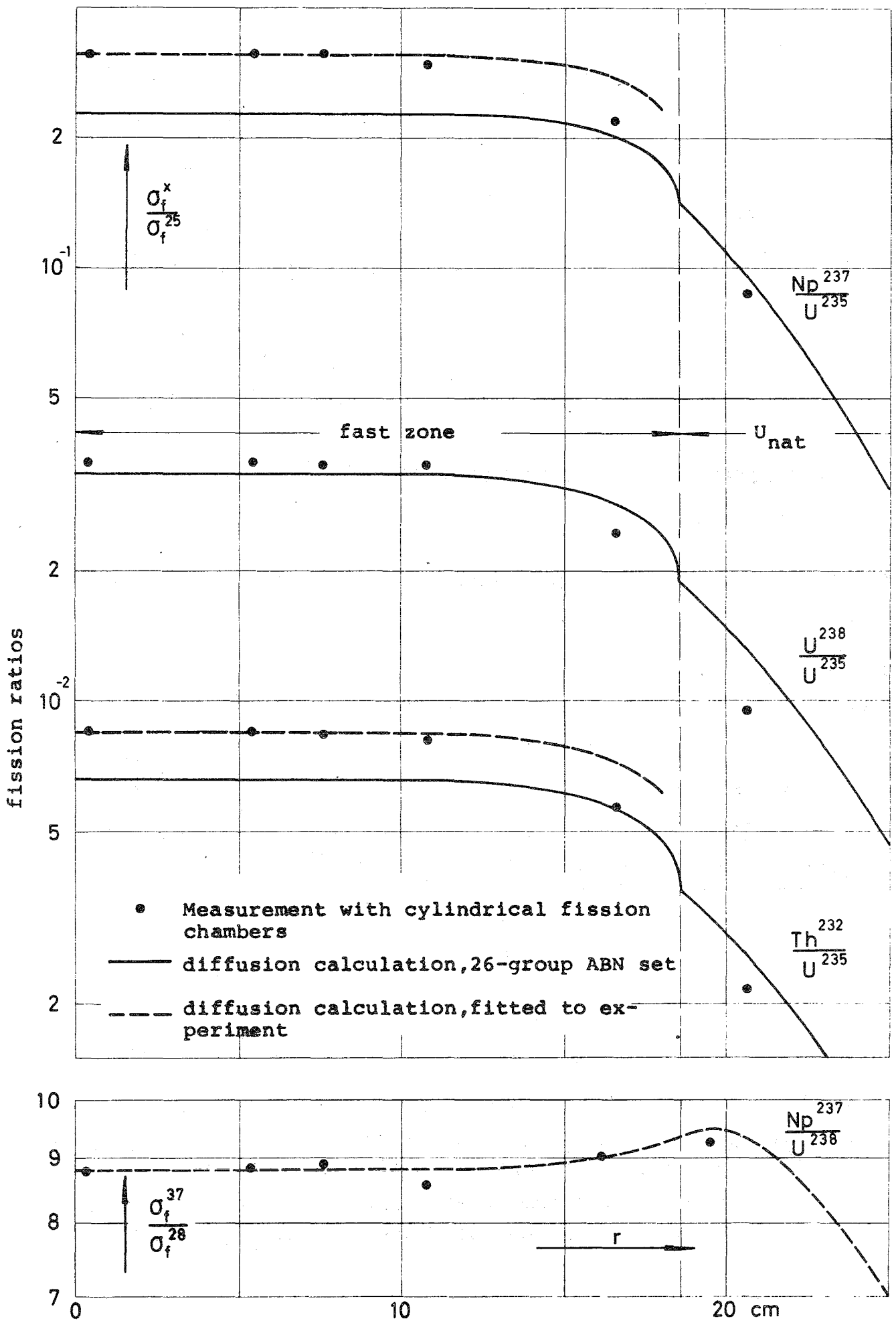

Fig. 12 Radial dependence of fission ratios in the midplane of STARK 5

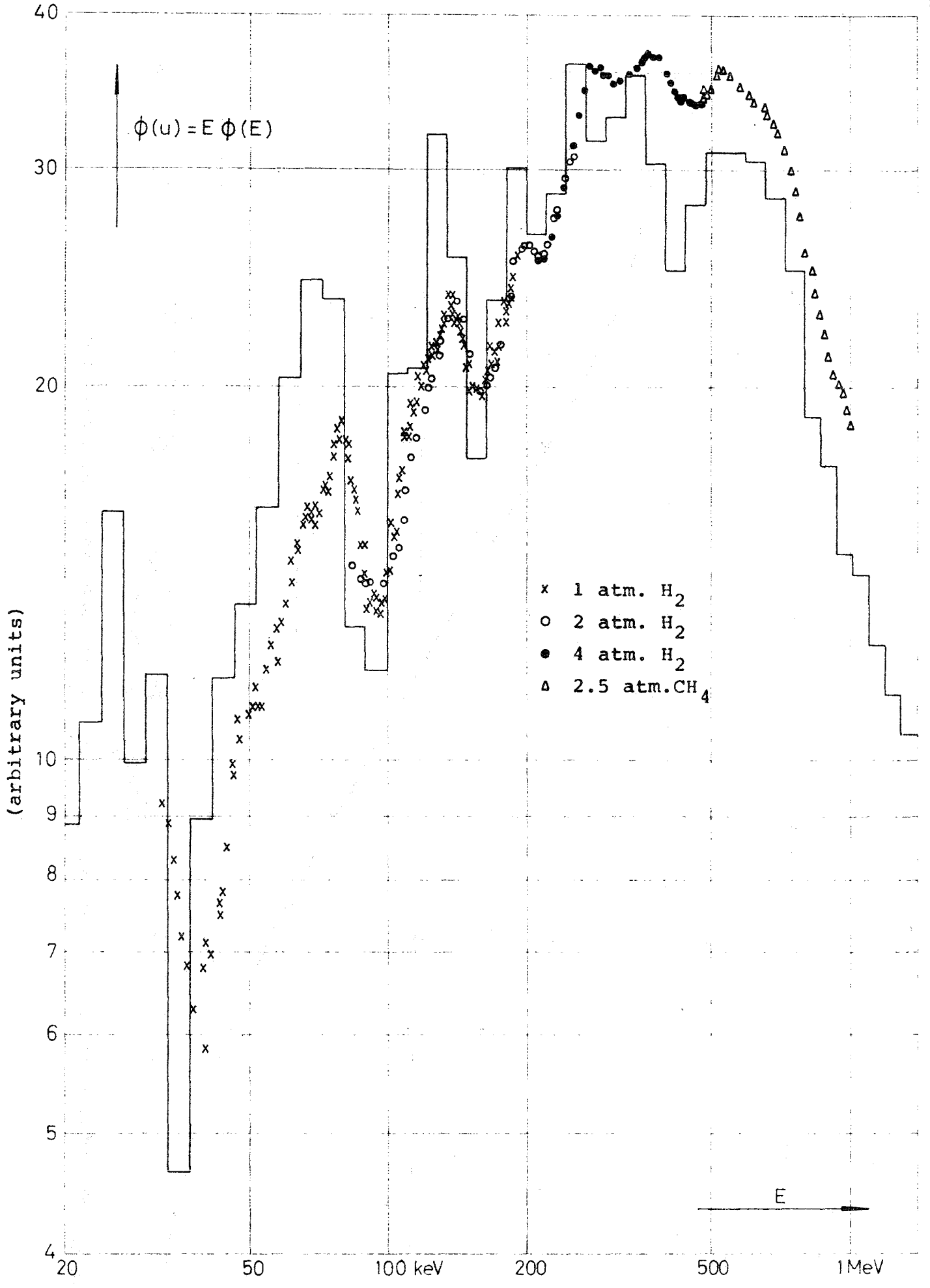

Fig. 13 Neutron spectrum in the center of STARK 5

× ○ ● △ proton recoil counter

——— 208-group calculation

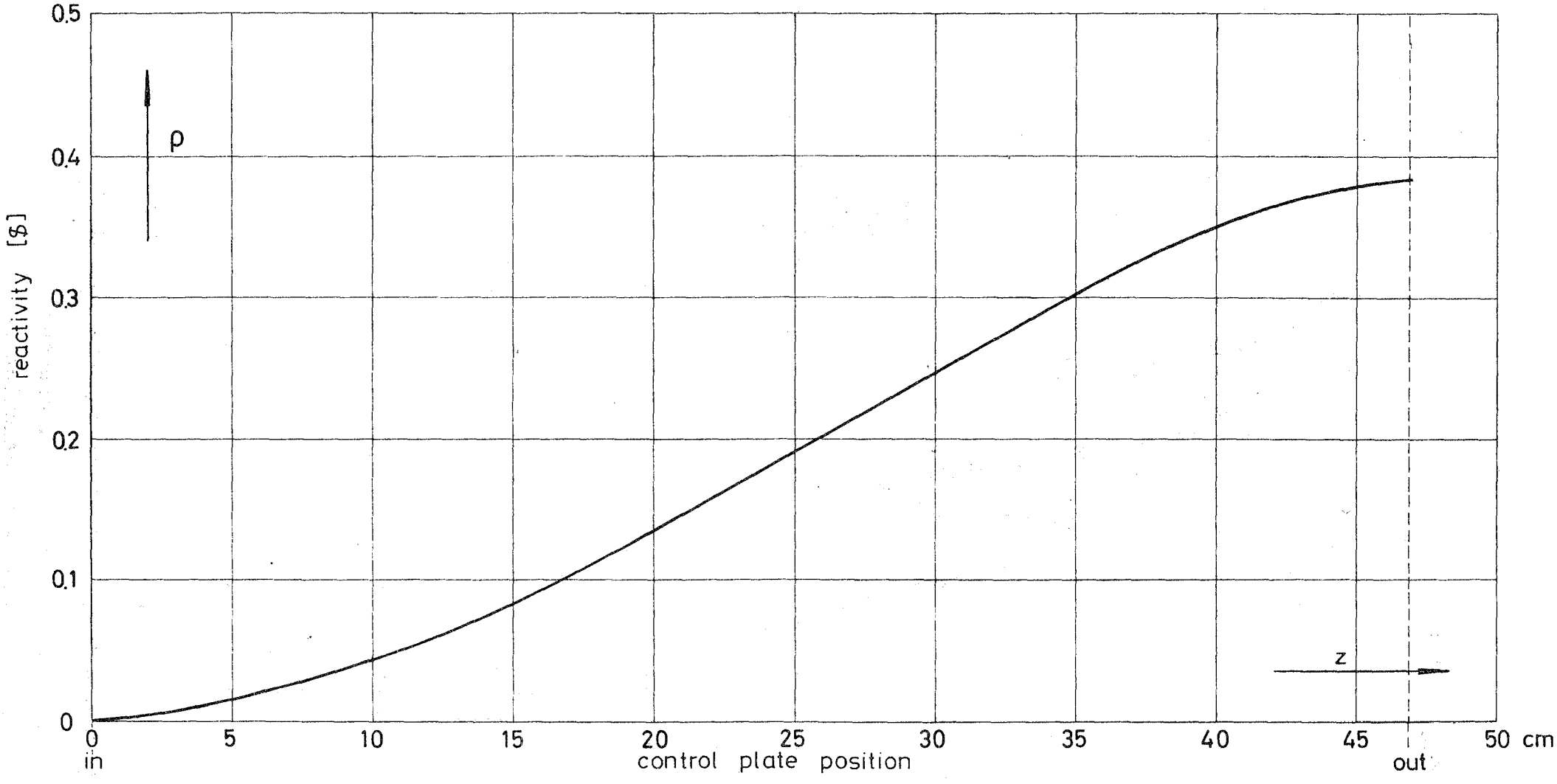

Fig. 14 Reactivity calibration of control plate R_3 by inverse kinetics method

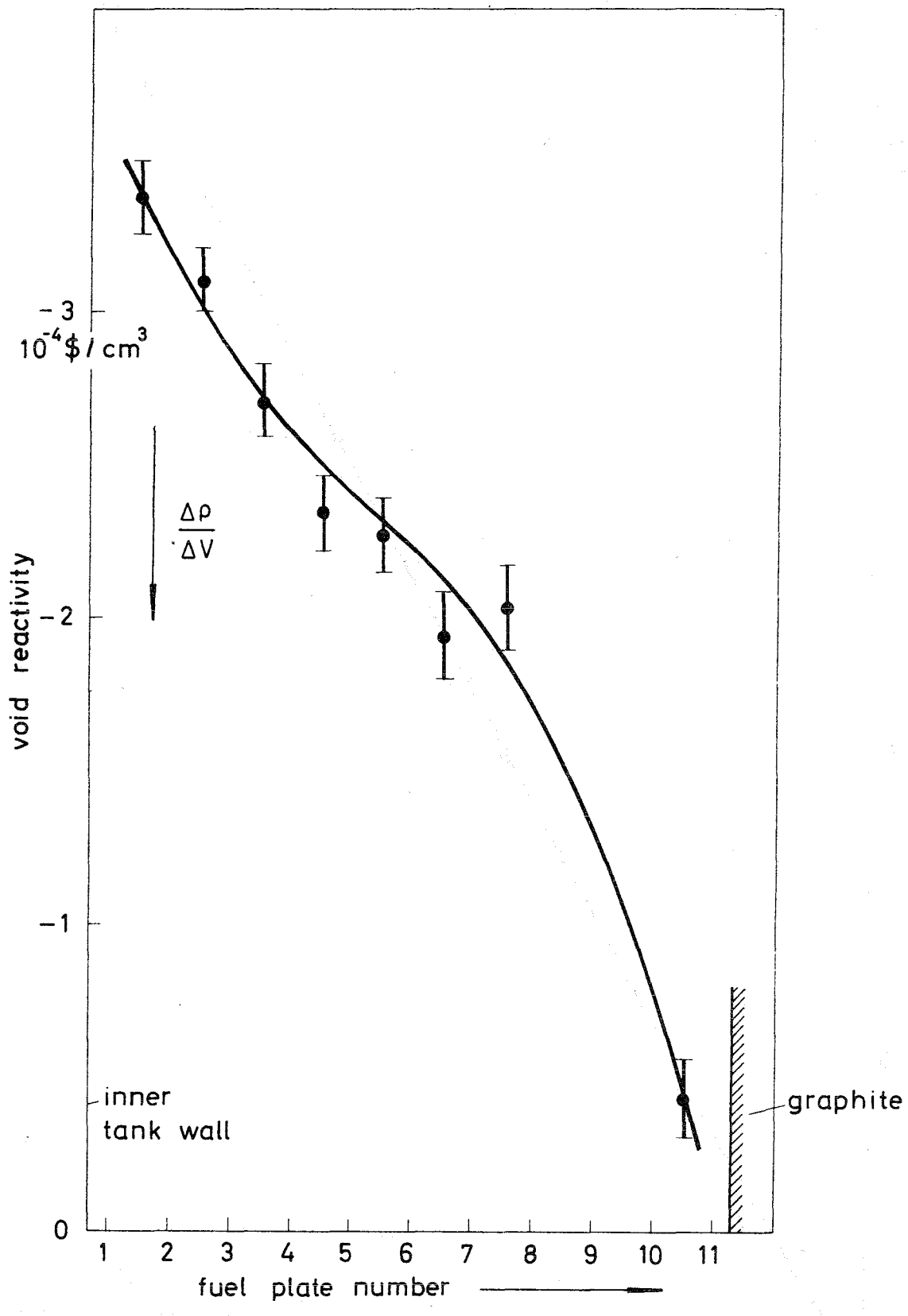

Fig. 15 Radial variation of the H_2O void coefficient measured within the fuel plate interspaces

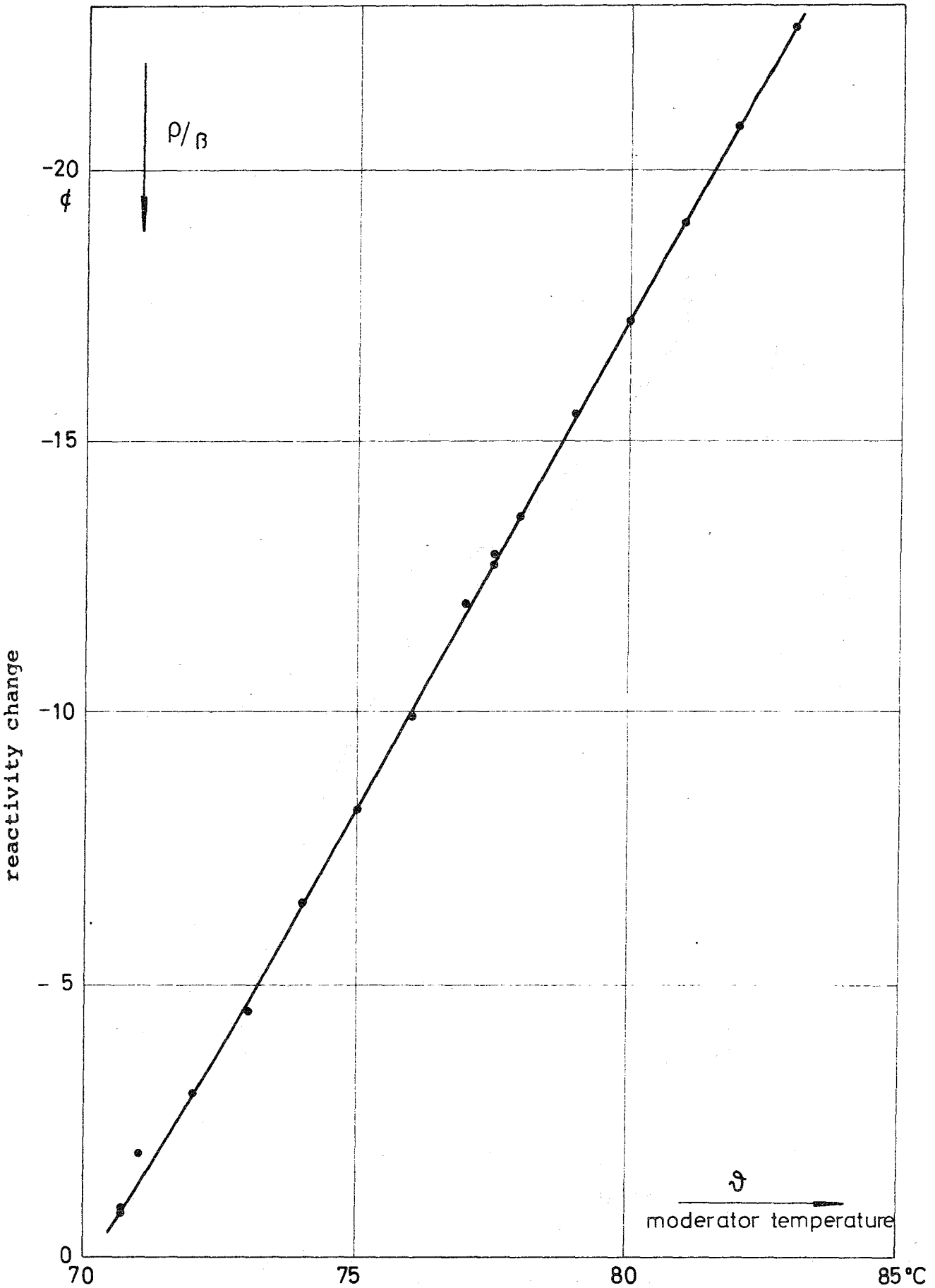

Fig. 16 Results of temperature coefficient determination

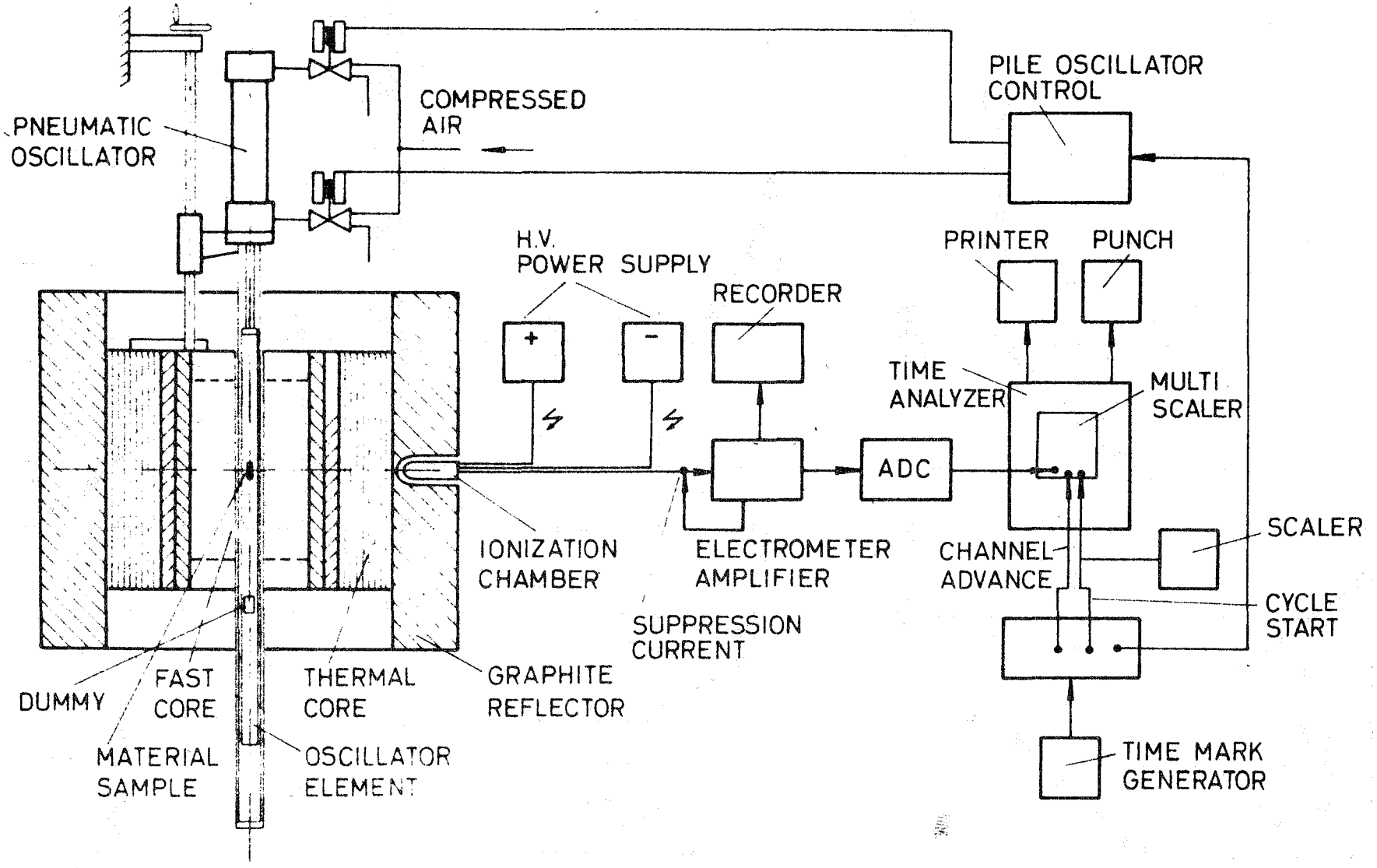

Fig. 17 Block diagram of square - wave pile oscillator

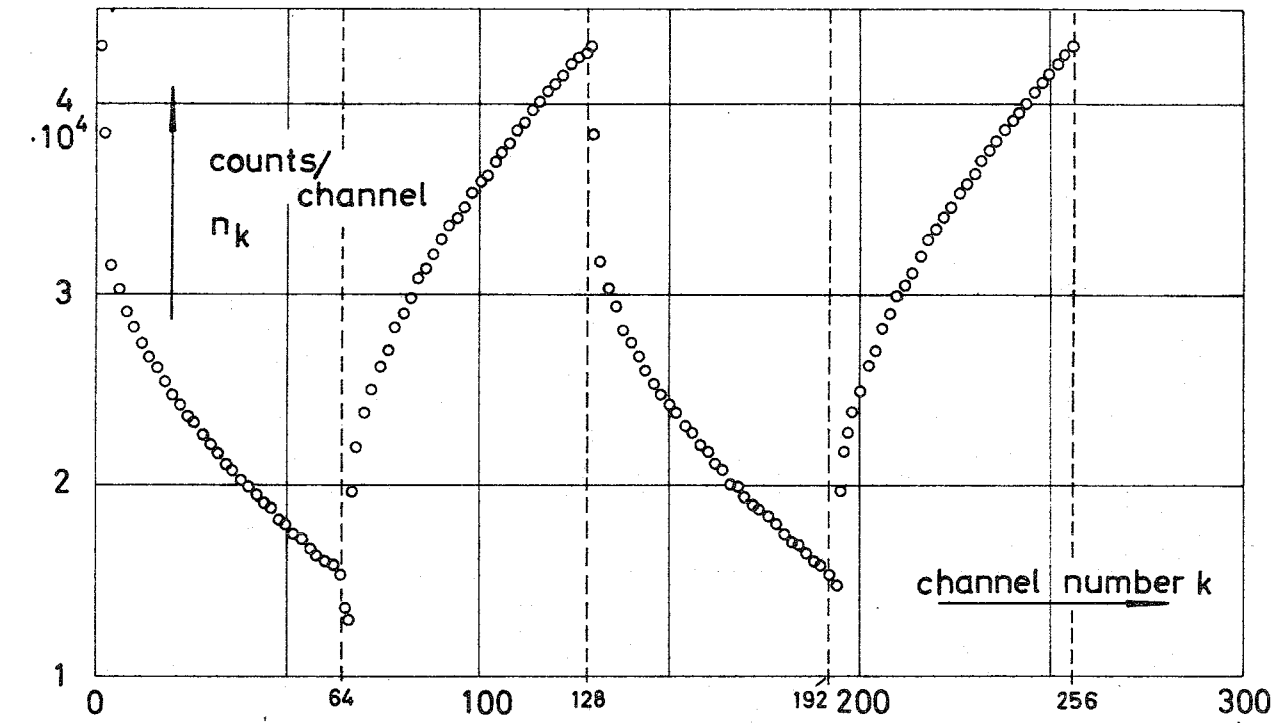

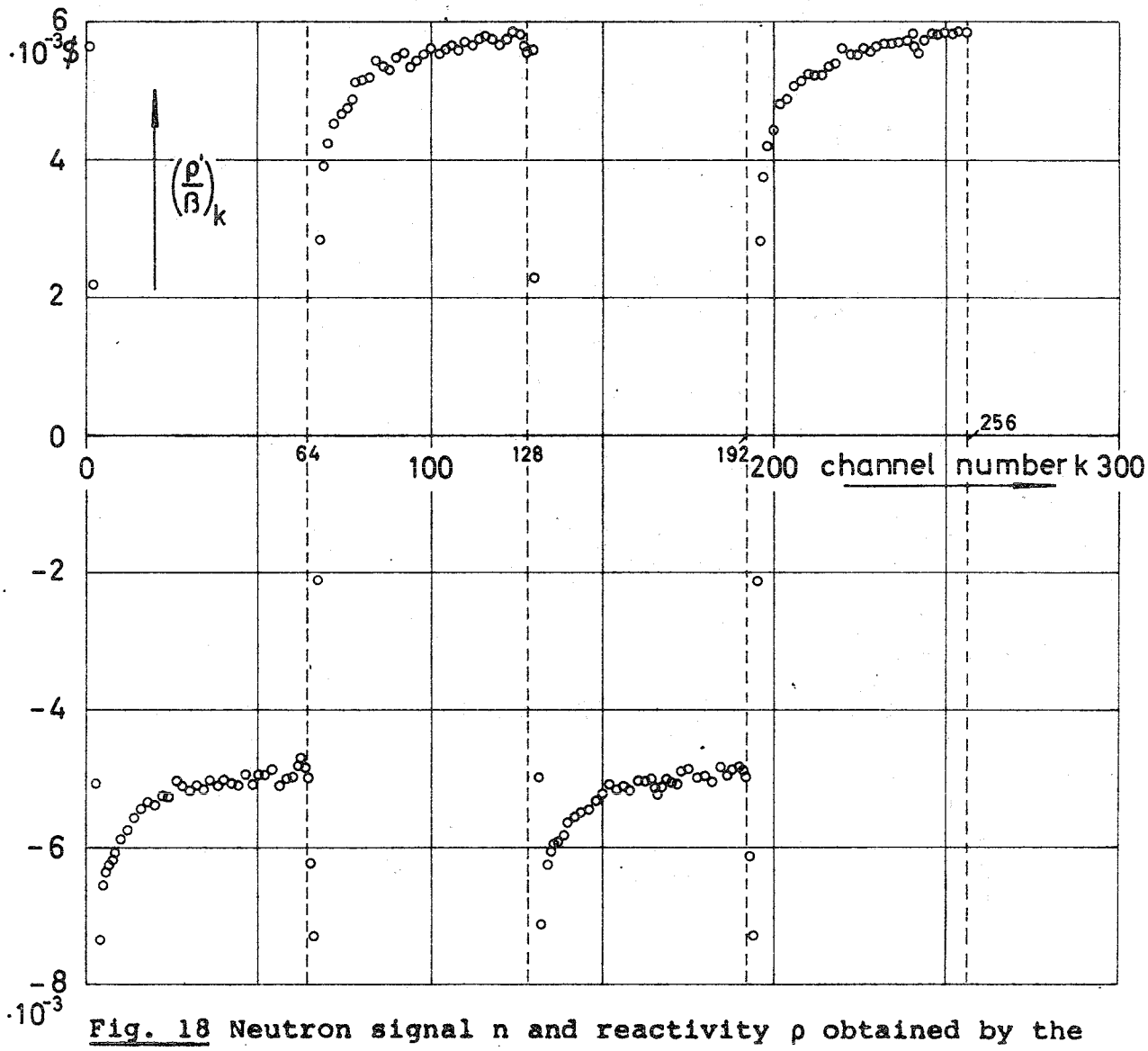

Fig. 18 Neutron signal n and reactivity ρ obtained by the inverse kinetics method for a pile oscillator measurement

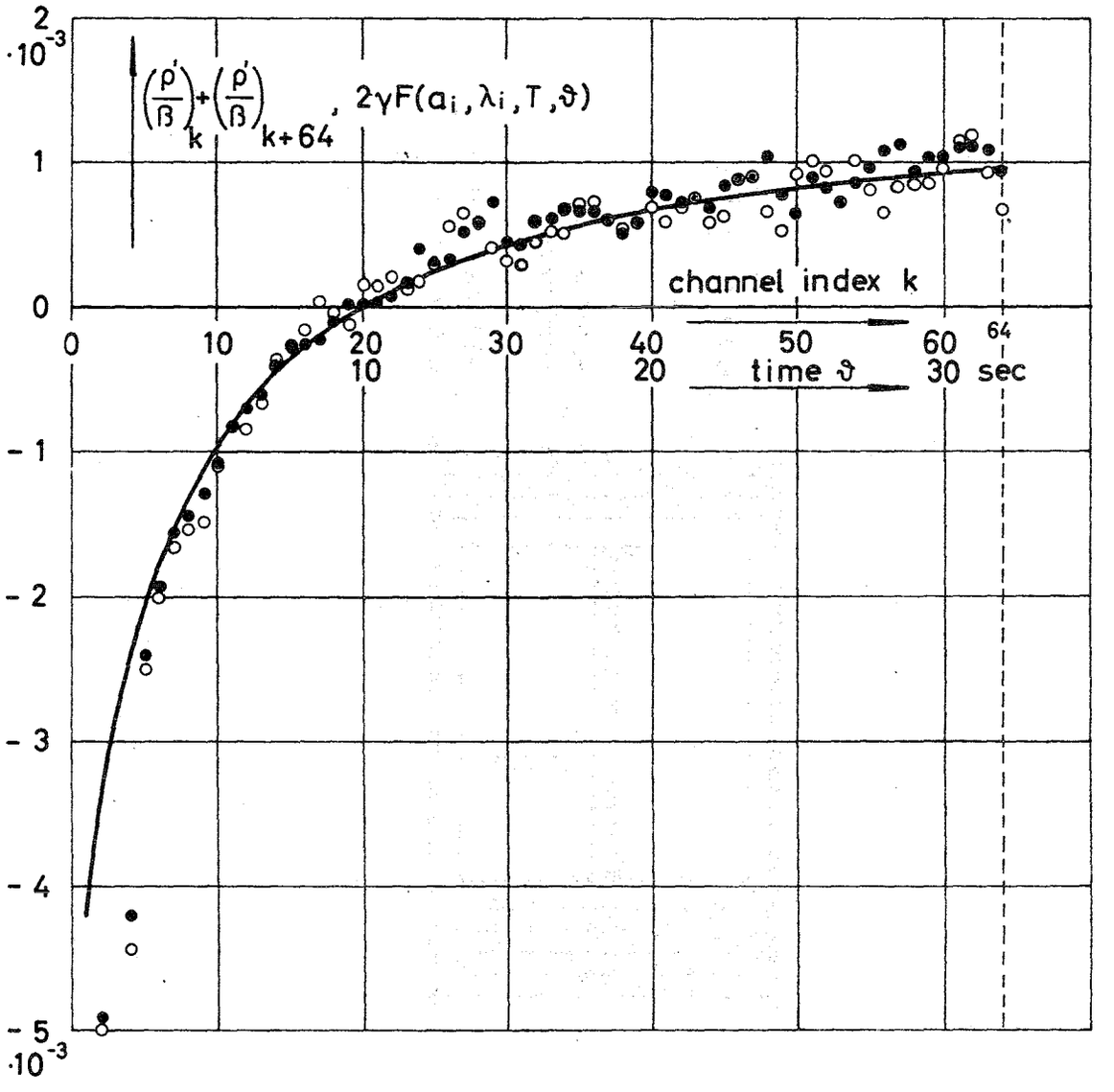

Fig. 19 Delayed neutron transient obtained by Eq.(3.4.17) from the data of Fig. 18

- ● experimental data (1st and 2nd half-period)
- ○ experimental data (2nd and 3rd half-period)
- ——— theoretical curve $2\gamma F(a_i, \lambda_i, T, \vartheta)$, Eq.(3.4.17), fitted to experimental data.

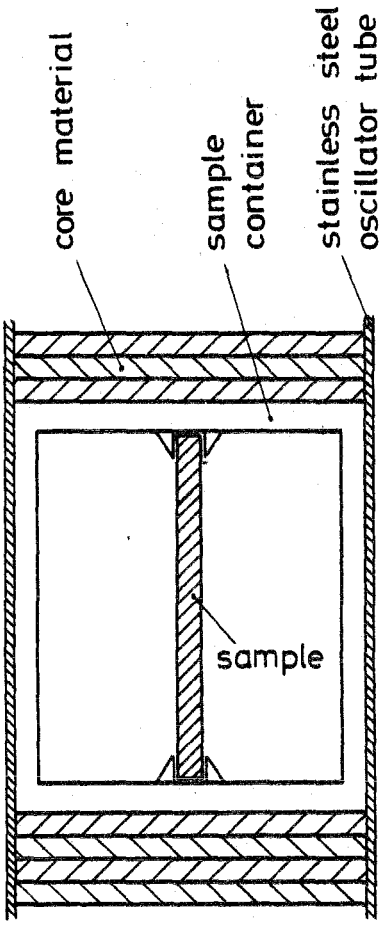

Fig. 20 Sample arrangement for pile oscillator measurements

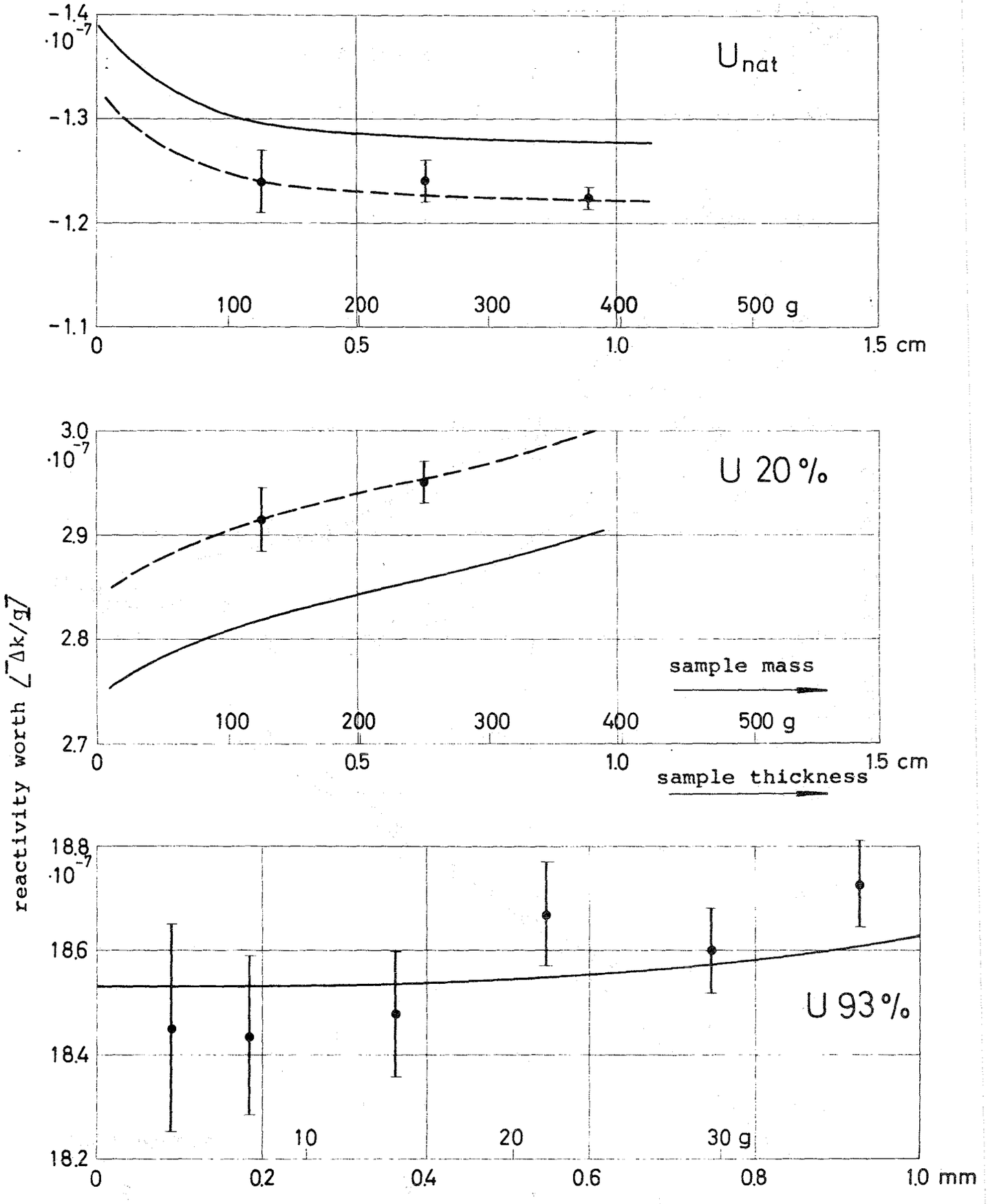

Fig. 21 Reactivity worth vs. sample size for U_{nat}, U(19.84%) and U(93.14%)

pile oscillator data

integral transport calculation (H2ØPMB set)

calculation, fitted to experiment

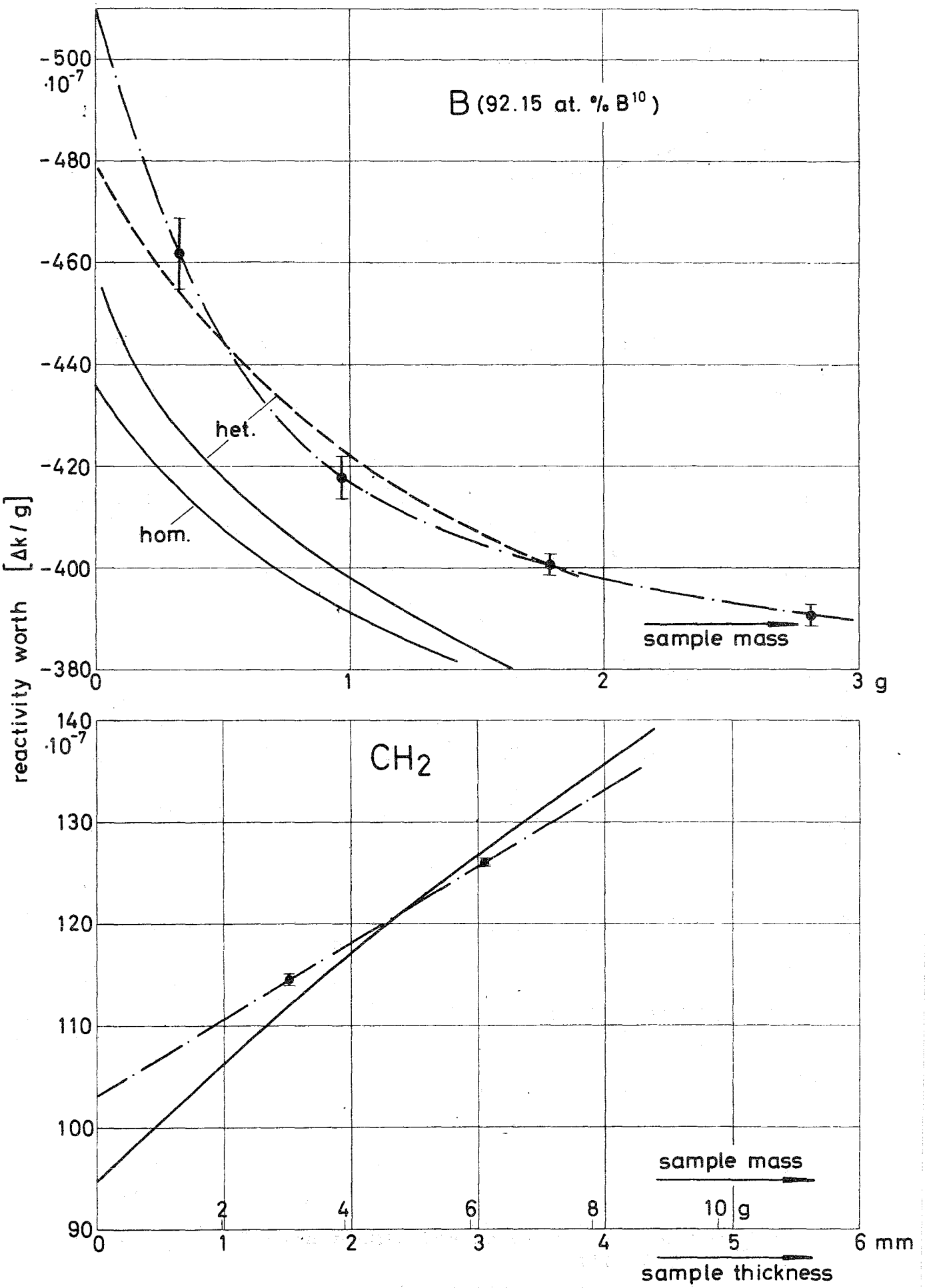

Fig. 22 Reactivity worth vs. sample size for B and CH_2
pile oscillator data, ——·—— experimental curve
—— integral transport calculation (H2ØPMB set)
— — calculation, fitted to experiment

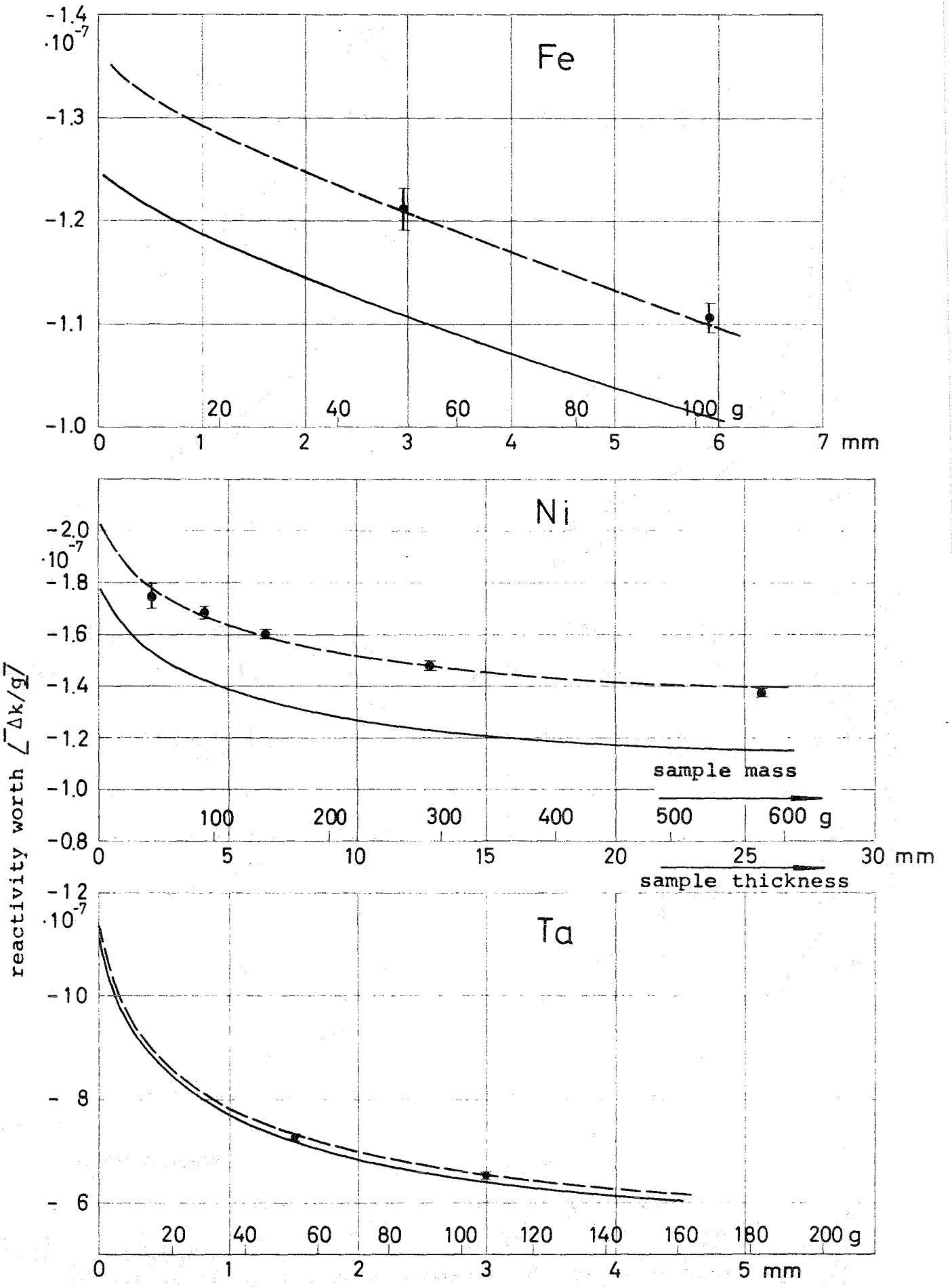

Fig. 23 Reactivity worth vs. sample size for Fe, Ni and Ta
● pile oscillator data,
——— integral transport calculation (H2ØPMB set)
– – – – calculation, fitted to experiment

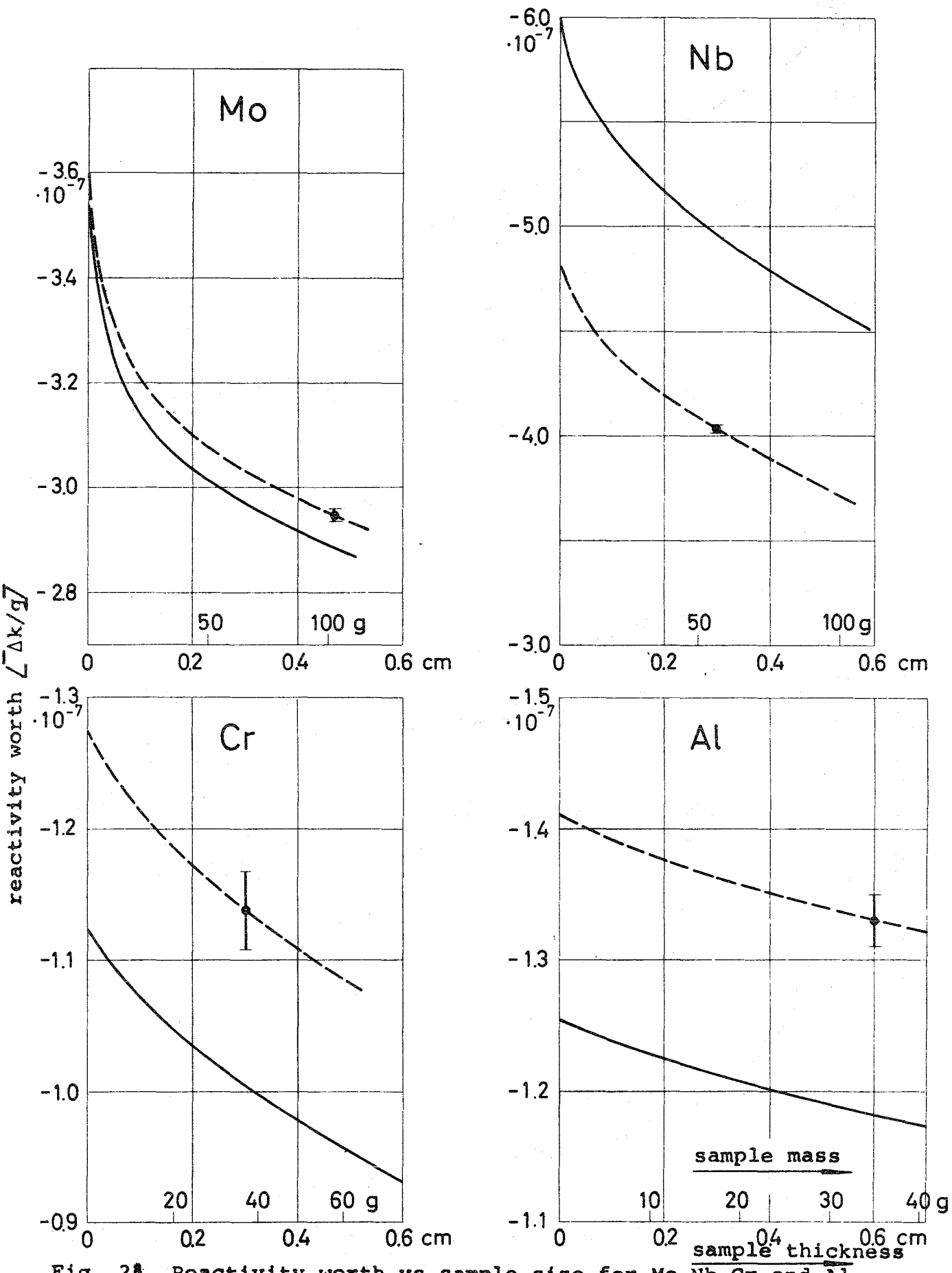

Fig. 2 Reactivity worth vs. sample size for Mo, Nb, Cr and Al

pile oscillator data

integral transport calculation (H2ØPMB set)

calculation, fitted to experiment

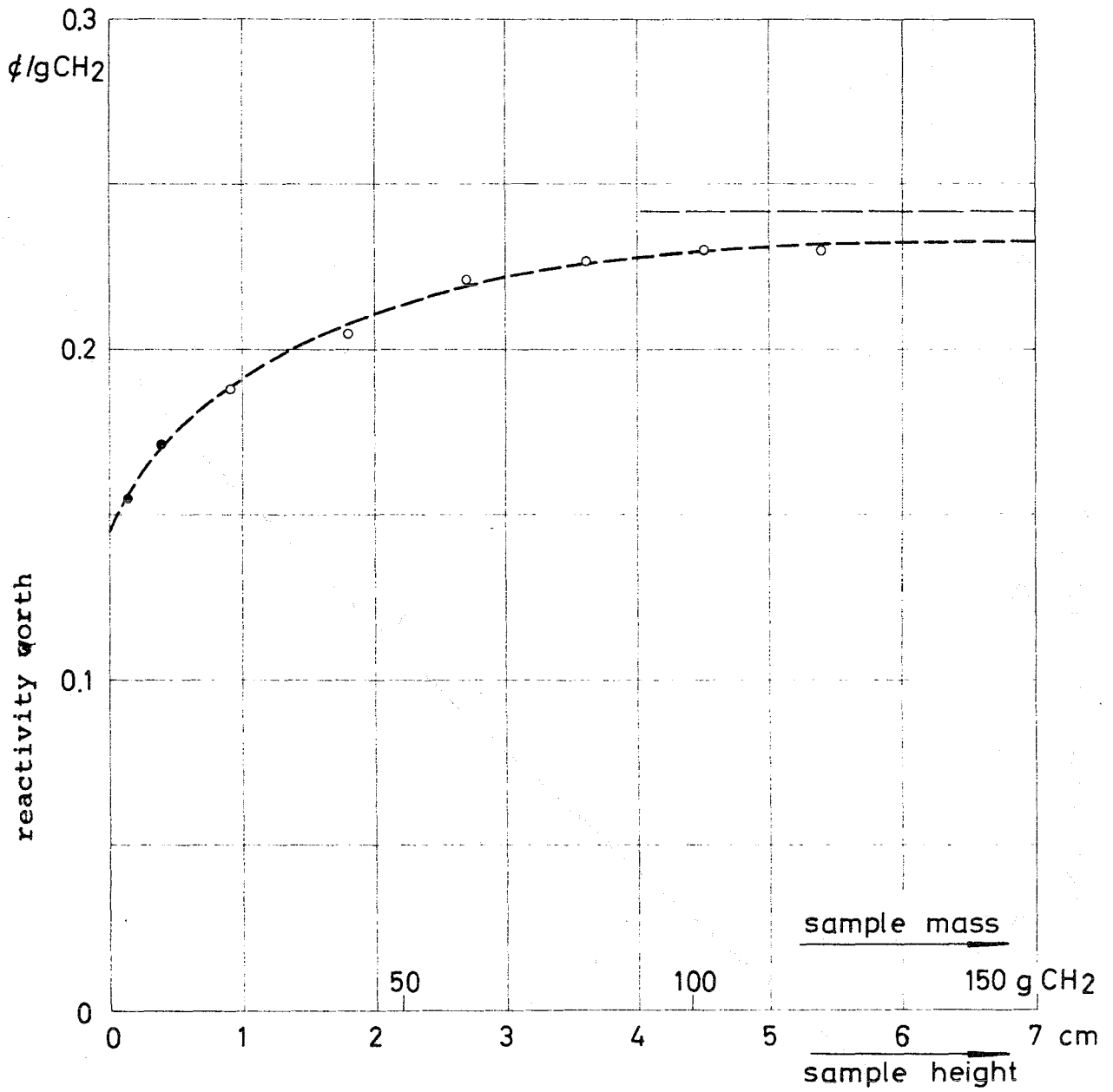

Fig. 25 Reactivity worth of polypropylene $(CH_2)_m$ in the center of the fast zone as a function of sample mass

—●— pile oscillator measurement

—○— static measurement for large samples

——— limiting value $(\rho^*/M)_\infty$

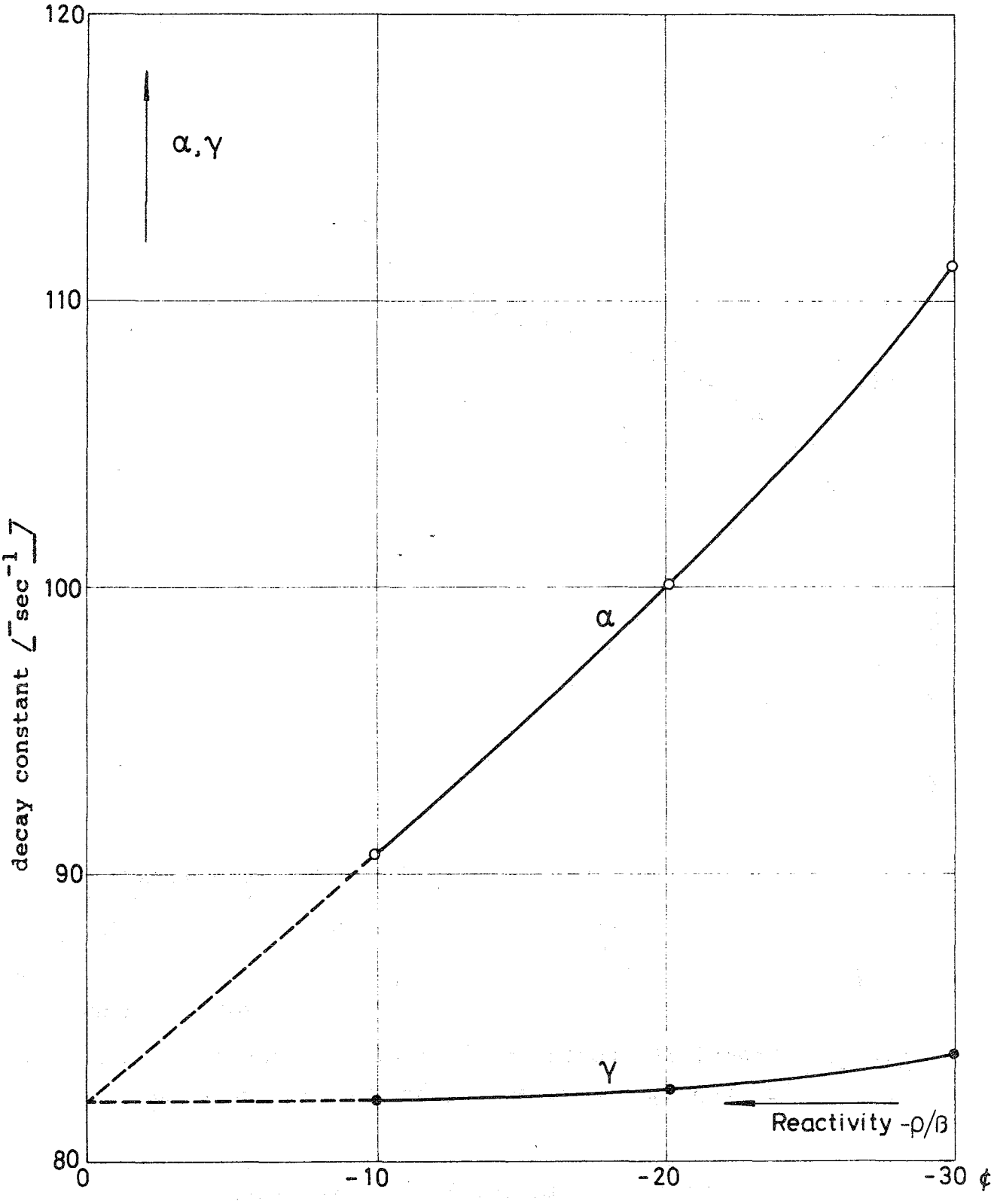

Fig. 26 Prompt neutron decay constant α and the parameter γ measured by the pulsed neutron source technique as a function of static reactivity ρ/β.

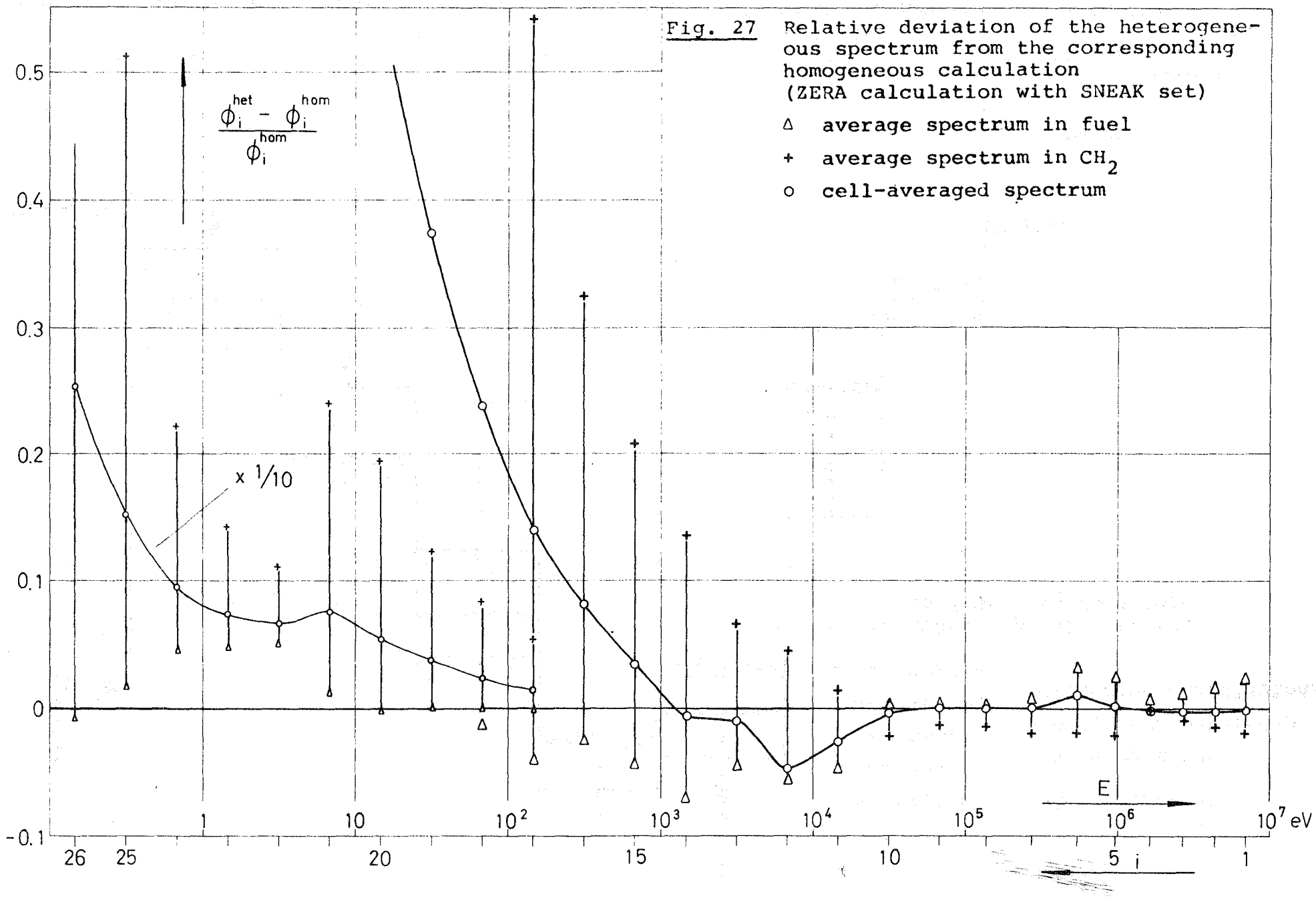
Fig. 27 Relative deviation of the heterogeneous spectrum from the corresponding homogeneous calculation (ZERA calculation with SNEAK set)
Δ average spectrum in fuel
+ average spectrum in CH_2
o cell-averaged spectrum
$\frac{\phi_i^{het} - \phi_i^{hom}}{\phi_i^{hom}}$
x 1/10
0.5
0.4
0.3
0.2
0.1
0
-0.1
1
10
10^2
10^3
10^4
10^5
10^6
10^7 eV
E
26
25
20
15
10
5
i
1

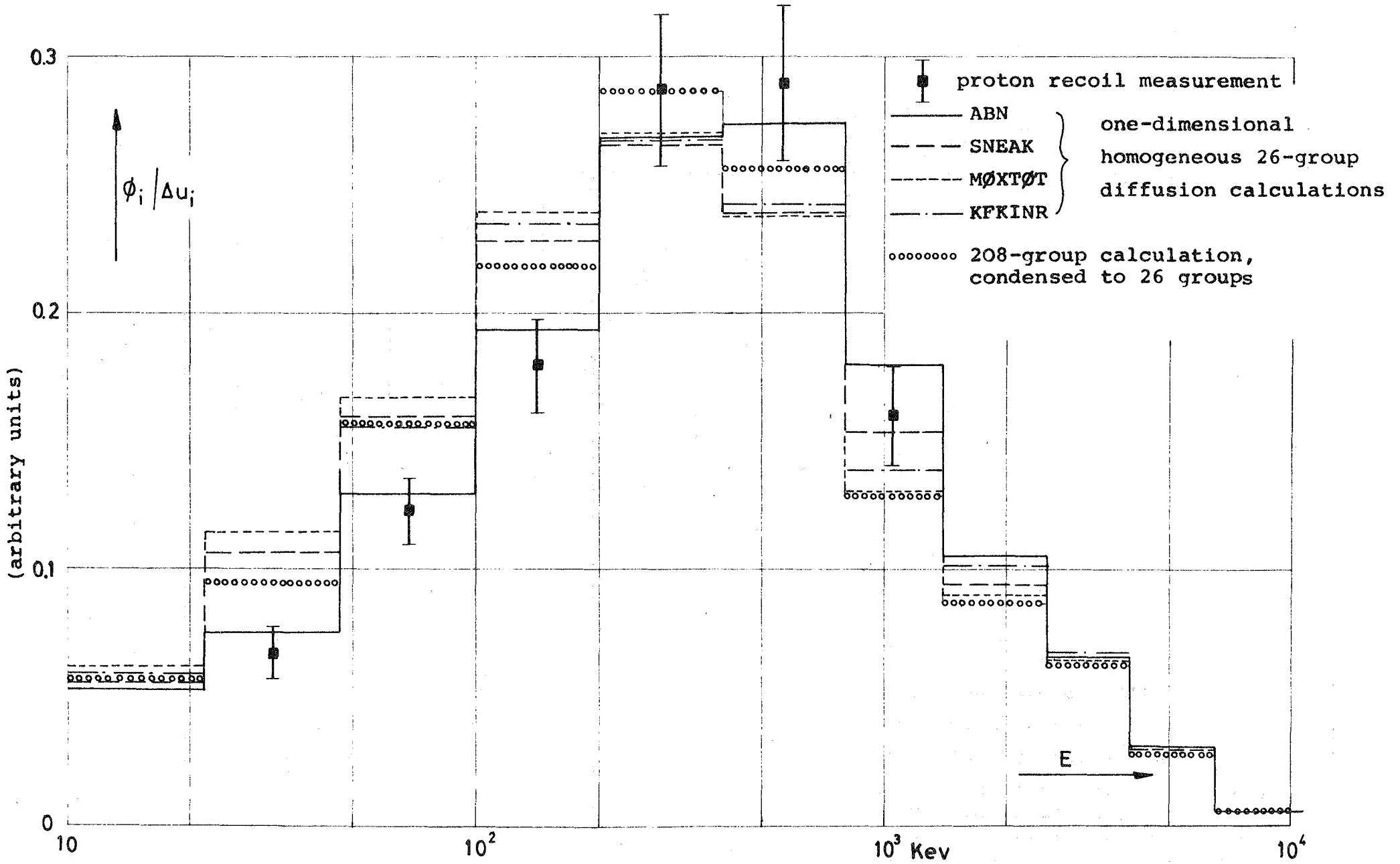

Fig. 28 Comparison of 26-group spectra for the center of STARK 5 (normalization interval 0.0465 to 2.5 MeV)

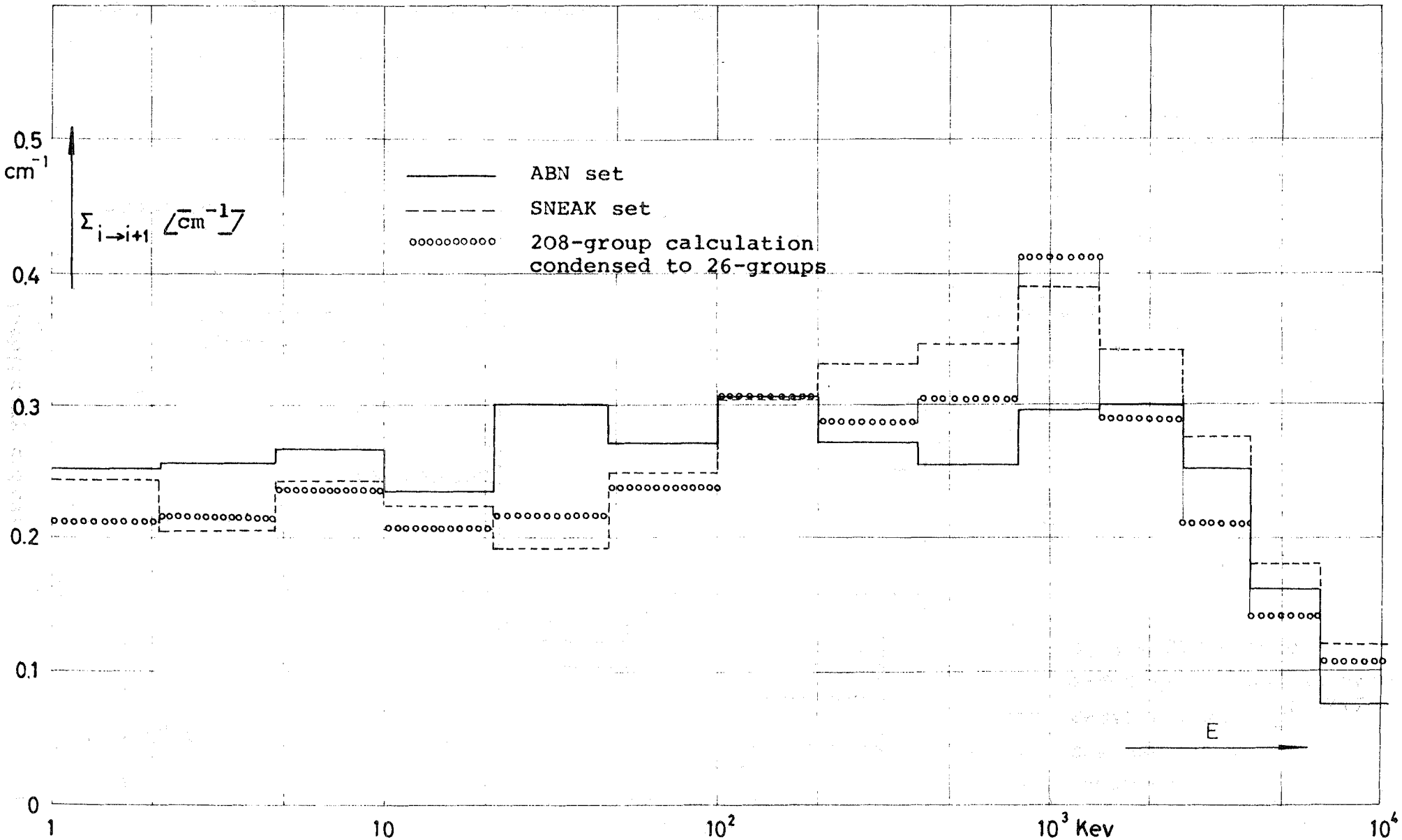

Fig. 29 Group transfer cross section $\Sigma_{i \to i+1}$ from 26-group sets and 208-group calculation

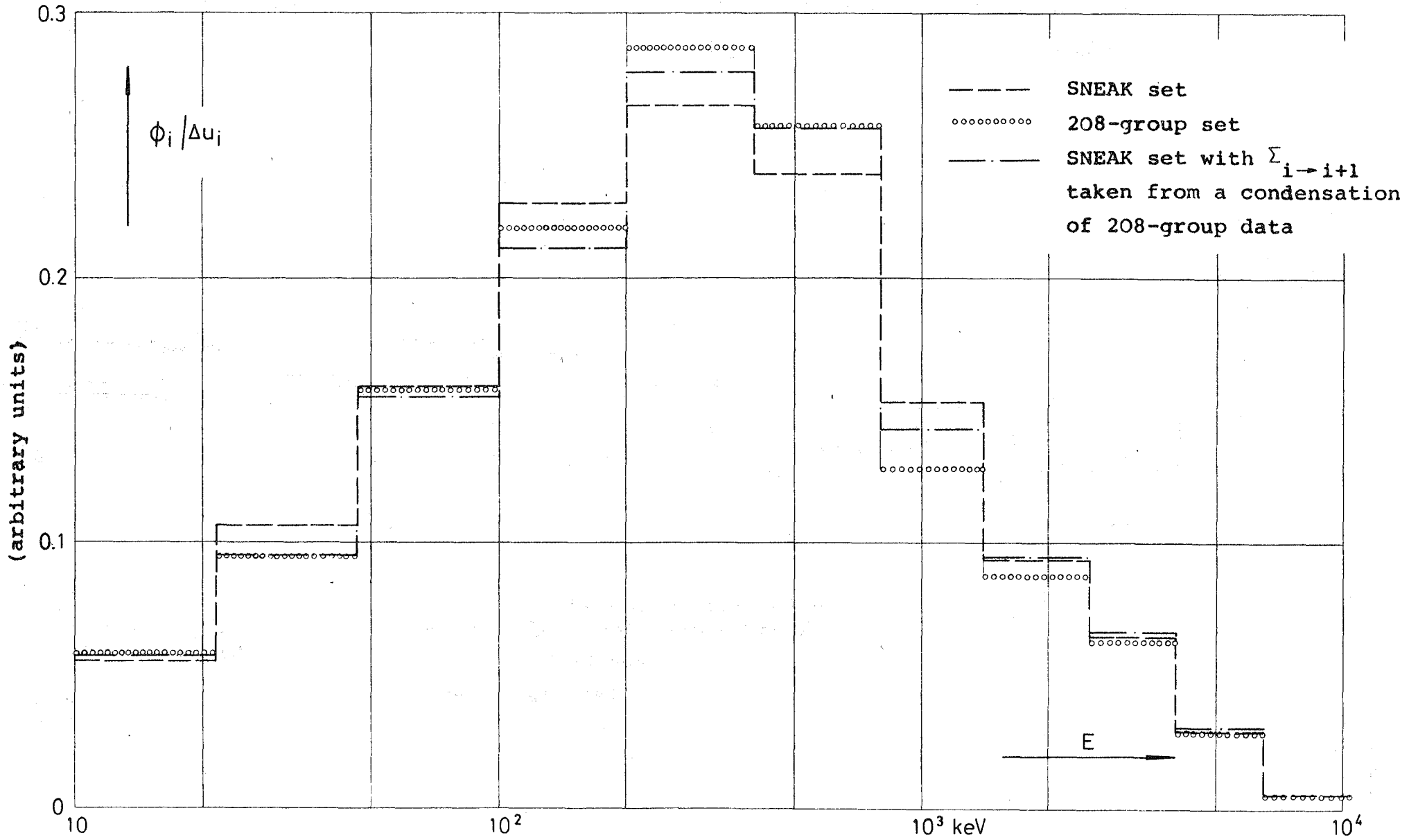

Fig. 30 26-group spectra for the center of STARK 5

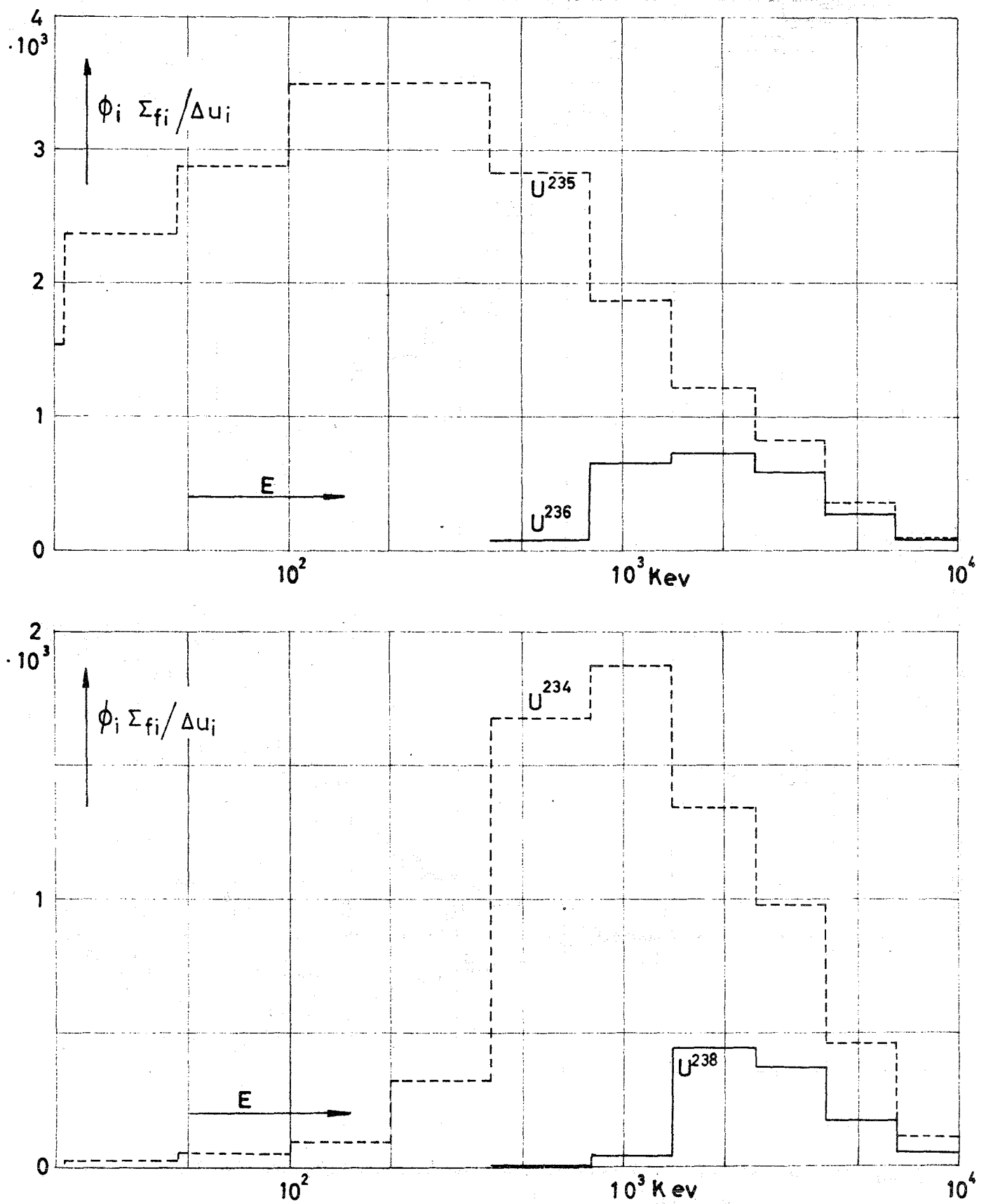

Fig. 31 Group contributions to the fission rate in U isotopes

——— U^{236}, U^{238} ---- U^{234}, U^{235}

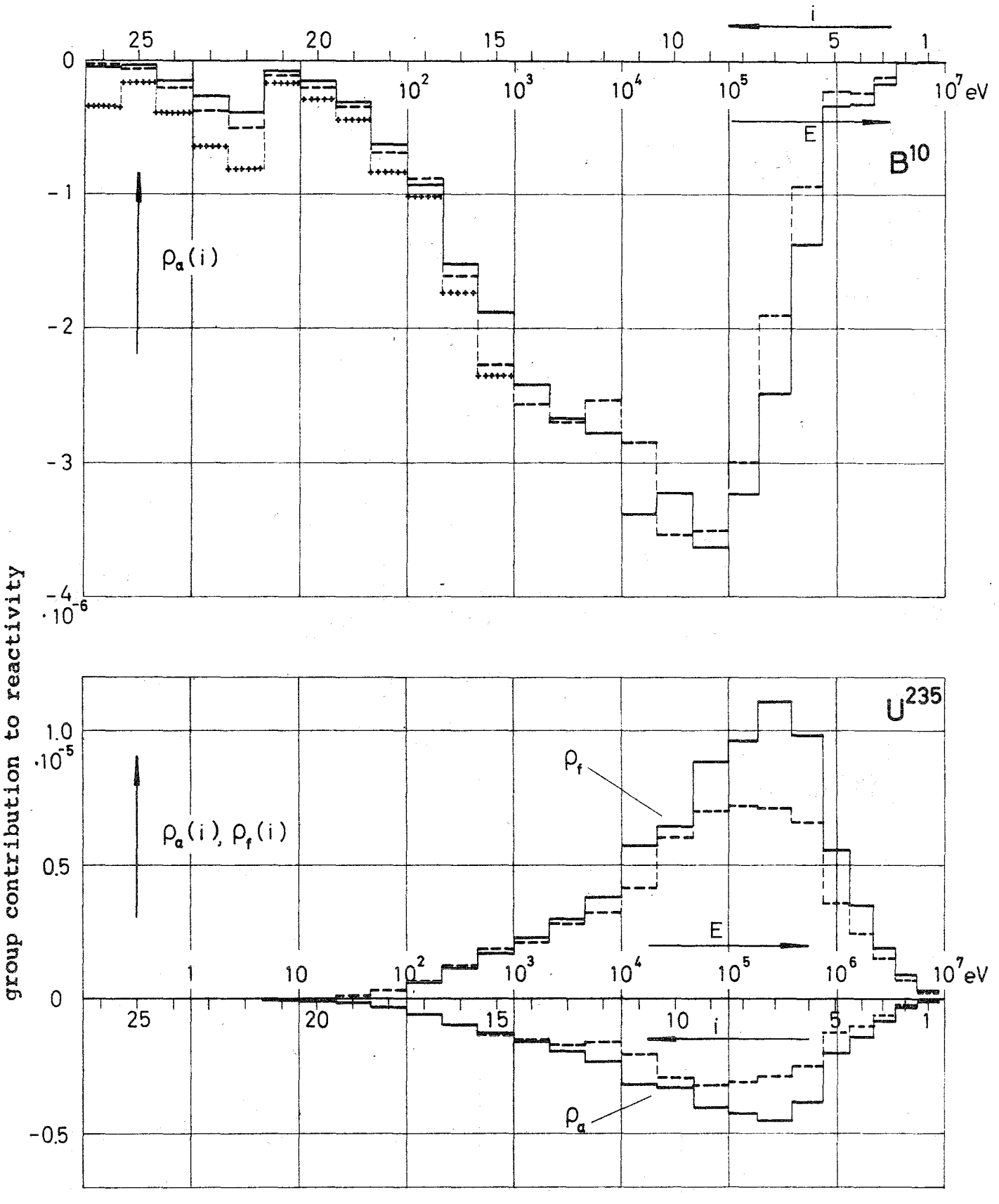

Fig. 32 Group contributions to the reactivity worth of B^{10} and U^{235}

——— ABN set
- - - - H2ØPMB set
+++++++ H2ØPMB set het.spectrum

} first-order-perturbation calculation

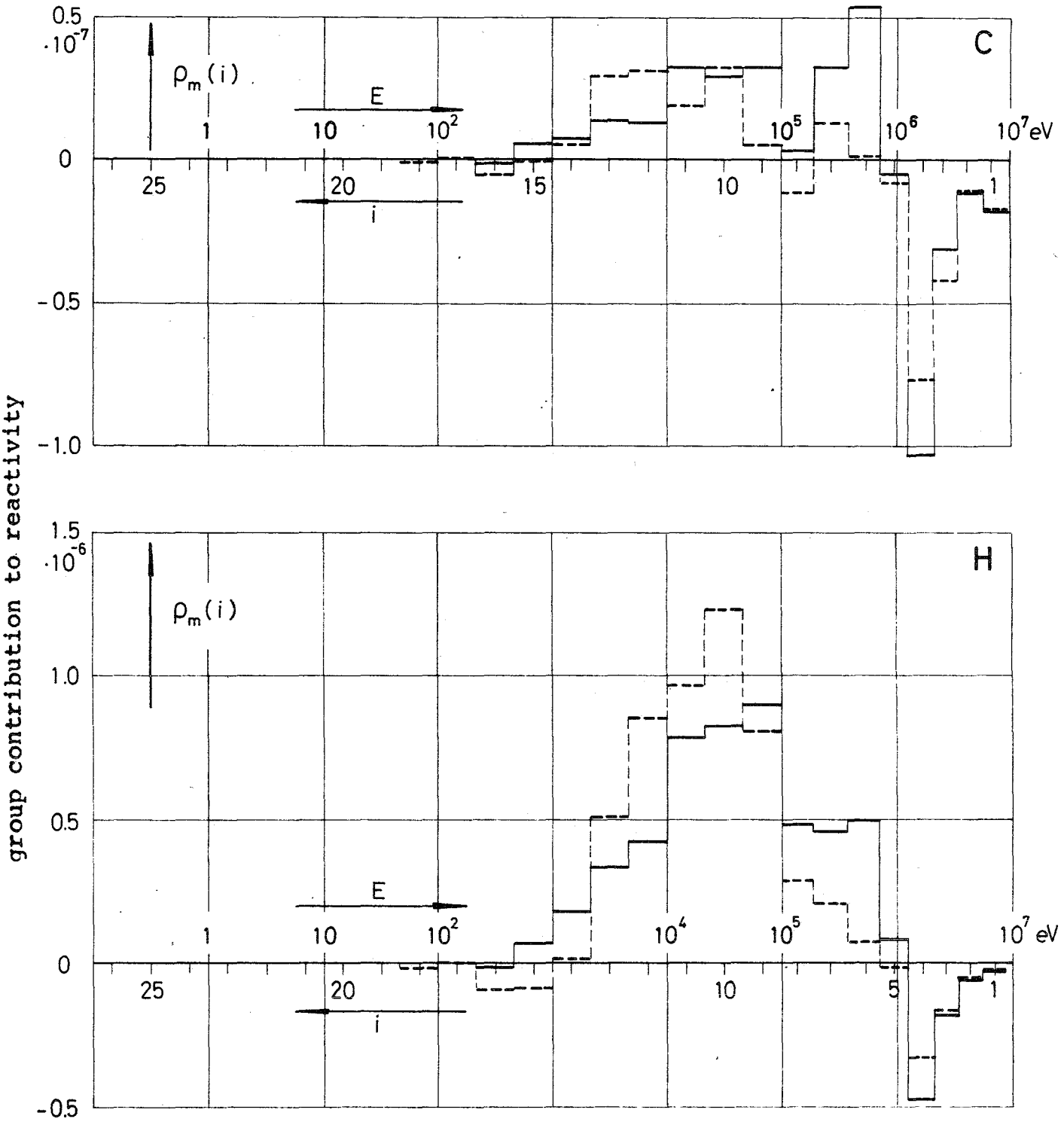

Fig. 33 Group contributions to the reactivity worth of C and H

——— ABN set
---- H2ØPMB set
} first-order perturbation calculation